

Compact SOI Polarization Rotators based on Asymmetric Periodic Loaded Waveguides

by

Yao Sun

A thesis submitted to the Faculty of Graduate and Postdoctoral Affairs in
partial fulfillment of the requirements for the degree of

Master of Applied Science in Electrical and Computer Engineering

Ottawa-Carleton Institute for Electrical and Computer Engineering

Department of Electronics

Carleton University

Ottawa, Ontario

Dec, 2015

© Copyright,

2015, Yao Sun

Abstract

Silicon-on-insulator (SOI) technology is a promising platform for photonic applications. It enables low-cost and large-volume production due to its compatibility with the complementary metal-oxide semiconductor (CMOS) fabrication process. With publicly accessible CMOS foundries and multi-project wafer (MPW) runs, SOI-based photonic integrated circuits (PICs) can be realized at an affordable cost. However, the high index contrast between silicon and the top cladding (SiO_2 or air) of SOI waveguides leads to considerable modal birefringence. Consequently, SOI-based PICs are generally highly polarization-sensitive, making polarization management a necessity. In this thesis, two polarization rotator (PR) designs based on the 220-nm SOI platform are demonstrated through numerical simulations and experiments. The demonstrated PR designs are based on asymmetrical periodic loaded waveguide structures. The demonstrated designs feature compact device footprints and can be fabricated by CMOS-compatible fabrication processes. Both designs have shown promising performance over the C-band wavelength range (1530 nm–1565 nm) in simulation. However, the fabrication requirements are stringent for these two designs, thus the performance of the fabricated devices are limited by the current fabrication technology.

Acknowledgements

I would like to acknowledge the help and contributions of all the people who have made this thesis possible; without you, I would never have made it to this point. First of all, I would like to thank my supervisor, Dr. Winnie Ye, for her support, guidance, and many hours spent revising my papers and this thesis. I would like to thank the Carleton Microfabrication Lab technicians, Rob Vandusen and Angela McCormick, for their help in preparing the chip for SEM imaging. I would like to thank Sebastian Schulz and Jeremy Upham, at the University of Ottawa, who took the SEM images of the fabricated devices. I would also like to thank my colleagues, Yule Xiong, Owen Marsh, Dusan Gostimirovic, Shuyu Ding, and Shuxia Li, for their invaluable help, advice, and friendship. I would like to acknowledge CMC Microsystems and the NSERC-SiEPIC Program, particularly Dan Deptuck, Dr. Jessica Zhang, and Dr. John Bock, who have provided great favor in fabricating the devices. I am grateful for the support from the staff in the Department of Electronics at Carleton University during my study here. Finally, I would like to offer my sincere gratitude to my husband, Kai Wang, and my parents, who have been a source of ongoing support and motivation through these years.

Table of Contents

Abstract	ii
Acknowledgements.....	iii
Table of Contents	iv
List of Figures	vii
List of Tables	x
Chapter 1.....	1
Introduction	1
1.1 Silicon Photonics	1
1.2 Slab Waveguide and Channel Waveguide	2
1.3 Waveguide Modes.....	3
1.4 Birefringence in SOI.....	6
1.5 Polarization Management	6
1.6 Polarization Rotation and Polarization Rotators	8
1.7 Thesis Objective and Organization	9
<i>Reference</i>	10
Chapter 2.....	11
Literature Review and Background	11
2.1 Mode Evolution based Polarization Rotators (PRs).....	12
2.2 Mode Coupling Based Polarization Rotators (PRs).....	15
2.2.1 General Approach in mode coupling based PRs.....	15
2.2.2 Asymmetrical Periodic Loaded Structures.....	18
2.3 Simulation Methods	22
2.3.1 Film Mode Matching Method	22
2.3.2 Finite Difference Method.....	24
2.3.3 Eigenmode Expansion Method	24
2.3.4 Finite-Difference Time Domain Method	25
<i>References:</i>	27
Chapter 3.....	29

Design and Parameter Optimization	29
3.1 Overview of Chapter 3	29
3.2 First Polarization Rotator Design.....	29
3.2.1 Device Structure.....	29
3.2.2 Device Optimization	30
3.2.3. Performance Evaluation.....	34
3.3 Second Polarization Rotator Design	38
3.3.1 Device Structure.....	38
3.3.2 Parameter Optimization	39
3.3.3 Performance Evaluation	42
<i>References</i>	45
Chapter 4.....	46
Fabrication and Testing Setup	46
4.1 IMEC Fabrication Technology Overview.....	46
4.2 Mask Layers and Process Modules for the SOI Patterning.....	47
4.3 Fabrication Tolerances and Bias	49
4.4 Mask Layout Design.....	51
4.5 Testing Circuit Mask Design	52
4.6 Testing Setup	54
<i>References</i>	57
Chapter 5.....	58
Experimental Results and Discussion	58
5.1 SEM Images of the Fabricated Devices	58
5.2 Performance Characterization for the First Design.....	60
5.3 Performance Characterization for the Second Design	64
5.4 Discussions on the Experimental Results	68
5.5 Discussions on Fabrication Tolerance	76
<i>References</i>	78
Chapter 6.....	79

Conclusions and Future Work	79
6.1 Significant Contribution.....	83
6.2 Publications.....	83
6.3 Achievements.....	84
6.4 Future Works	84
<i>References</i>	86
Appendix A.....	87

List of Figures

Fig.1. 1. Schematic of SOI wafer.....	2
Fig.1. 2. Schematic of a slab (left) and a channel (right) waveguide on SOI platform.....	3
Fig.1. 3. Electric field distributions of the two fundamental modes in a 500 nm * 300 nm SOI channel waveguide.....	4
Fig.1. 4. The schematic of a ridge waveguide on SOI platform.	5
Fig.1. 5. Schematic of integrated polarization diversity scheme [6].....	8
Fig.2. 1. Schematic of the mode evolution PR design in [10].....	13
Fig.2. 2.Schematic of the PR design using a-Si overlayer [12].	14
Fig.2. 3. Schematic of the demonstrated polarization rotation design [9].	17
Fig.2. 4. Schematic cross section of the plasmonic waveguide based PR design [11].	18
Fig.2. 5. Schematic of the first demonstrated PR based on asymmetrically periodic loaded structures [13].....	19
Fig.2. 6 Polarization Rotation in one period of left and right side perturbed waveguide sections.	21
Fig.2. 7. An example of an SOI rib waveguide under the FMM treatment.	23
Fig.2. 8. A MMI coupler modeled by EME.....	25
Fig.3. 1. Top view and structure (inset diagram) of the proposed polarization rotator design.	30
Fig.3. 2. Extinction Ratio (ER) as a function of waveguide core width (W_c) and slab width (W_s) combinations calculated by EME.	31
Fig.3. 3. Extinction Ratio (ER) as a function of Periods (N) and slab length (L_s) combinations calculated by EME.....	32
Fig.3. 4. Extinction Ratio (ER) as a function of slab thickness and core thickness combinations calculated by EME.....	33
Fig.3. 5. Extinction Ratio (ER) as a function of perturbed slab sections alternation periods N with a given set of optimized device parameters ($W_c=0.4 \mu\text{m}$, $W_s=0.15 \mu\text{m}$, $L_s=1.315 \mu\text{m}$).	34
Fig.3. 6. Transverse electric field components E_x and E_y along the proposed polarization rotator design (top view) for TE (a), (b) and TM (c), (d) polarization inputs.	35

Fig.3. 7. Wavelength dependence of extinction ratio (ER) for both TE and TM polarized inputs, calculated by 3D-FDTD.....	36
Fig.3. 8. Wavelength dependence of polarization rotation efficiency (PRE) for both TE and TM polarized inputs, calculated by 3D-FDTD.	37
Fig.3. 9. Wavelength dependence of the insertion loss for both TE and TM polarized inputs, calculated by 3D-FDTD.....	38
Fig.3. 10. Top view and cross section views (inset diagram) of the proposed polarization rotator design.	39
Fig.3. 11. Extinction Ratio (ER) as a function of waveguide total width ($W_c + W_s$) and slab width (W_s) combinations calculated by EME.....	40
Fig.3. 12. Extinction Ratio (ER) as a function of Periods (N) and half taper length (LHT) combinations calculated by EME.	40
Fig.3. 13. Extinction Ratio (ER) as a function of slab thickness and core thickness combinations calculated by EME.	41
Fig.3. 14. Extinction ratio of the proposed polarization rotator design as a function of wavelength for both TE and TM polarized input modes, calculated by 3D-FDTD.	44
Fig.3. 15. Wavelength dependence of the polarization rotation efficiency for both TE and TM polarized inputs, calculated by 3D-FDTD.	44
Fig.3. 16. Wavelength dependence of the device insertion loss (IL) for both TE and TM polarized inputs, calculated by 3D-FDTD.	45
Fig.4. 1. The three available etch levels in IMEC’s Si Photonics PSV technology.....	47
Fig.4. 2. Cross section view of SOI patterning on the SK levels.	48
Fig.4. 3. Cross section view of SOI patterning with mask layers on different etch levels.....	49
Fig.4. 4. Relationship between the dimensions on the mask and that on the wafer based on the data provided in [2].....	50
Fig.4. 5. Mask layout designs for the two proposed devices.	51
Fig.4. 6. Mask of testing circuits for one group of devices.....	53
Fig.4. 7. The completed mask layout for the proposed designs.	54
Fig.4. 8. Block diagram of the testing setup.	56
Fig.5. 1. SEM images showing (a) topview of the fabricated first design, (b) topview of the fabricated second design.	59

Fig.5. 2. Topview of the testing circuit for the fabricated design.	60
Fig.5. 3. Normalized measured transmission as a function of wavelength of the fabricated device. .	61
Fig.5. 4. Extinction Ratio of the fabricated device (with rectangular shaped perturbed sections) as a function of wavelength.....	62
Fig.5. 5. PRE for the fabricated devices (the first design) as a function of wavelength of the fabricated device.	63
Fig.5. 6. Normalized measured transmission as a function of wavelength of the fabricated device. .	65
Fig.5. 7. Extinction Ratio of the fabricated device (with triangular shaped perturbed sections) as a function of wavelength.....	66
Fig.5. 8. PRE for the fabricated devices (with triangular shaped perturbations) over the operating wavelengths.....	67
Fig.5. 9. Comparison between the measured ER and the simulated ER considering fabrication deviations.	71
Fig.5. 10. Comparison between the measured ER and the simulated ER considering fabrication deviations.	74
Fig.5. 11. Measured Transmissions for TE and TM inputs from the reference circuits.	75
Fig.5. 12. Self-alignment process by using hard mask for both rib waveguides (left) and channel waveguides (right) [4].....	77

List of Tables

TABLE 3. 1. SUMMARY OF OPTIMIZED GEOMETRICAL PARAMETERS.....	34
TABLE 3. 2. SUMMARY OF OPTIMIZED GEOMETRICAL PARAMETERS.....	43
TABLE 5. 1. SUMMARY OF THE FABRICATION TOLERANCES.....	69
TABLE 5. 2. SUMMARY OF IMPACT OF CORE WIDTH VARIATION BY FDTD METHOD FOR THE FIRST DESIGN.....	70
TABLE 5. 3. SUMMARY OF IMPACT OF CORE WIDTH VARIATION BY FDTD METHOD FOR THE SECOND DESIGN	72
TABLE 5. 4. SUMMARY OF IMPACT OF SLAB WIDTH VARIATION BY FDTD METHOD FOR THE SECOND DESIGN	73

Chapter 1

Introduction

1.1 Silicon Photonics

Silicon has been of great interest to the photonics industry, as it is compatible with silicon Integrated Circuit (IC) fabrication processes. By utilizing the well-established and standardized complementary metal-oxide semiconductor (CMOS) fabrication process in the microelectronic industry, silicon-on-insulator (SOI) technology has become a promising platform for photonic applications by enabling low-cost and large-volume production. With publicly accessible CMOS foundries and multi-projects wafer (MPW) runs, SOI-based photonics integrated circuits (PICs) can be realized at an affordable cost [1].

Fig. 1.1 presents the schematic of an SOI wafer. It is consisted of three layers: a thin surface layer of silicon (thickness ranges from several hundred Å to several μm) where the optical circuits are formed (top), an underlying layer of buried oxide (BOX) which isolates the top silicon layer from the main body of the wafer (middle), and another bulk silicon layer as mechanical support (bottom).

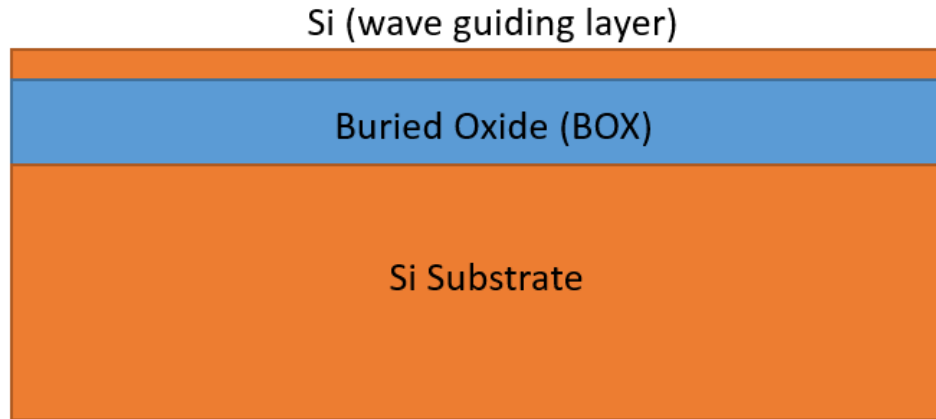


Fig.1. 1. Schematic of an SOI wafer.

The high index contrast between silicon ($n_{\text{Si}} = 3.45$) and the cladding materials ($n_{\text{air}} = 1$ and $n_{\text{SiO}_2} = 1.45$) offers strong optical confinement, which enables guiding of light in structures with down to several-hundred-nanometer dimensions.

1.2 Slab Waveguide and Channel Waveguide

A slab waveguide is considered to be the simplest waveguide structure, where only one-directional confinement is present. An SOI slab waveguide is formed by sandwiching a core layer (high index) with two layers having lower refractive indices. An SOI wafer itself (Fig. 1.1) is a slab waveguide (with air cladding). A channel waveguide is formed by sandwiching a two-dimensional confined dielectric with a high refractive index between two layers with lower refractive indices. The schematic of a slab waveguide (left) and a channel waveguide (right) on the SOI platform is shown in Fig. 1.2.

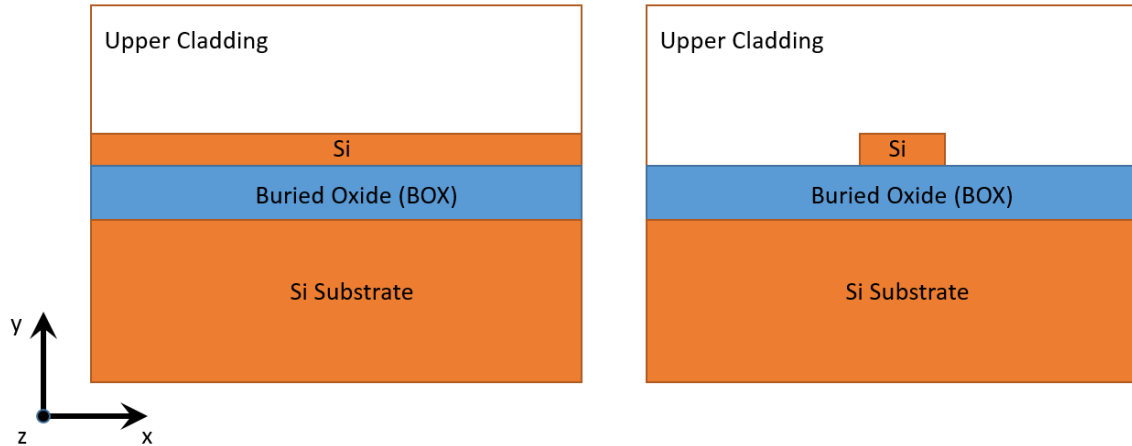


Fig.1. 2. Schematics of a slab waveguide (left) and a channel waveguide (right) on the SOI platform.

Along the z direction, with an angle of incidence above the critical angle, total internal reflection inside the waveguide (dielectric with a higher refractive index) is achievable. Thus, light can be strongly confined in an SOI waveguide.

1.3 Waveguide Modes

When electromagnetic waves propagate through waveguides, they become waveguide modes, and are governed by Maxwell's equations. These modes are a spatial distribution of optical energy in one or more dimensions that remain constant in time [2]. They present the eigen solutions to Maxwell's equations, which are solved for the boundary conditions based on the waveguide geometry. The numerical methods used to solve waveguide modes are discussed in Chapter 2. A guided mode has an effective index n_{eff} larger than the refractive index of the cladding layers. As shown in Fig. 1.2, the guided mode propagates along the z axis, where the y - z plane is the plane of incidence that contains the wave vectors for the incident, reflected, and transmitted light.

In a simple slab waveguide (Fig.1.2 left), the transverse electric (TE) mode and transverse magnetic (TM) mode are supported. TE modes have their electric fields perpendicular to the plane

of incidence (lying in the core layer), whereas TM modes have their magnetic fields perpendicular to the plane of incidence (with electrical field normal to the core layer). The field components for these two modes are defined as $E_y=E_z=H_x=0$ and $H_z=H_y=E_x=0$ for TE and TM modes, respectively. In a two-dimensionally confined waveguide (as shown in Fig.1.2(b) and Fig.1.4), pure TE and TM modes do not exist. The boundary conditions imposed by the waveguide in both the x and y direction don't support the field components defined for the slab waveguides. Instead, we use the term "TE-like mode" and "TM-like mode" to define the hybrid modes in which the E_x and H_y components dominate, and in which the E_y and H_x dominate, respectively. The "TE-like modes" are denoted as E_{pq}^x , and the "TM-like modes" are denoted as E_{pq}^y , where p and q represent the numbers of the field extrema (maxima and minima) in the x and y directions.

Fundamental modes refer to lowest order of TE and TM-like modes. Fig.1.3 presents the electric field distributions of the two fundamental modes in a 500-nm × 300-nm SOI channel waveguide.

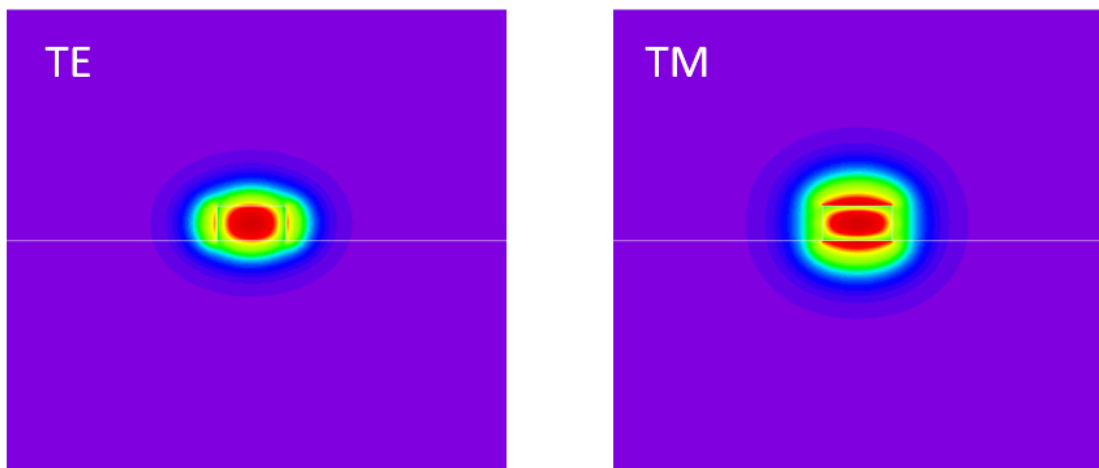


Fig.1. 3. Electric field distributions of the two fundamental modes in a 500-nm × 300-nm SOI channel waveguide.

The TE and TM modes are orthogonally polarized. As we can see from Fig.1.3, if a channel waveguide is confined in the x–y direction, and light is propagating through the waveguide along

the z direction, the electric field of a TE-like mode will expand more along the x direction, and that of a TM-like mode will expand more along the y direction.

The total number of optical modes supported by a waveguide depends on its geometry. A single-mode waveguide supports only the fundamental modes (including both the lowest-order TE and TM modes). In SOI channel waveguides, the core dimension should be smaller than a half-wavelength of a guided wave in silicon in order to fulfill the single-mode condition. For example, for a 1550-nm wavelength in a 200-nm-thick silicon channel waveguide, the single-mode condition is fulfilled when the core width is less than 460 nm [3]. By proper design, ridge waveguides (Fig. 1.4) can meet the single-mode condition even when having the cross-sectional dimensions in several microns [4].

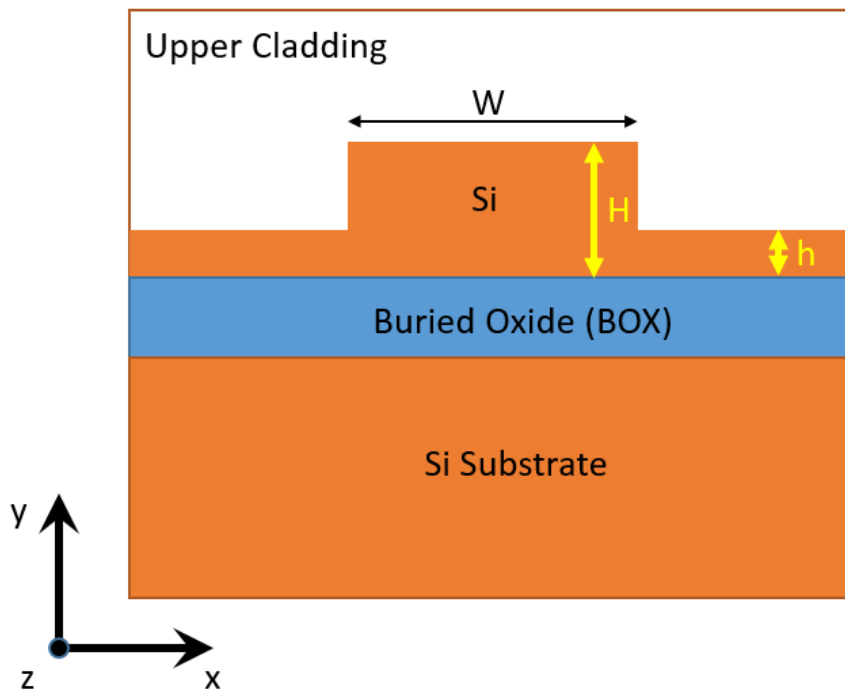


Fig.1. 4. The schematic of a ridge waveguide on the SOI platform.

The approximate expression for single-mode-condition ridge-waveguide-design is defined (with the geometry parameters shown in Fig. 1.4) as

$$\frac{W}{H} \leq 0.3 + \frac{\frac{h}{H}}{\sqrt{1-\frac{h^2}{H}}}, \text{ for } \frac{h}{H} \geq 0.5 \quad (1.1)$$

In designs following Equ. 1.1, the initial propagating higher-order modes are leaky. After a short propagation distance, only the fundamental modes in the ridge region will survive [4].

1.4 Birefringence in SOI

Waveguide birefringence describes the anisotropy with respect to polarization in the propagation constant of the optical modes [5]. It is defined as the difference between the effective indices of the two orthogonally polarized waveguide modes: TE and TM.

Although SOI wafers enable light guiding in nanoscale PICs, the high index contrast makes the control of waveguide birefringence extremely challenging. Consequently, SOI-based PICs are generally highly polarization dependent, which is undesired, as the polarization state changes randomly in optical fibers. Furthermore, the large birefringence will cause polarization mode dispersion, which will limit high-speed data transmission bandwidth. The polarization-dependent wavelength characteristics induced by birefringence will impose problems in delay-based filter devices (e.g., AWGs) [3].

1.5 Polarization Management

In order to achieve polarization-independent performance, several solutions have been proposed: a perfect-square core waveguide, polarizers, and the polarization-diversity scheme. The simplest solution is to use a perfect-square core, which has a symmetric geometry in every direction. However, it has stringent fabrication requirements (less than a nanometer). For instance, the differential group delay in a 5-cm-long 300-nm \times 300-nm waveguide reaches 6.6 ps with a \pm 5-

nm variation in core width. This 6.6-ps delay will degrade high-speed signals with data rates above 40 Gbps [6]. Thus, a fabrication error of less than 1 nm is required for devices used in polarization-independent dense wavelength division multiplexing systems.

Polarizers pass only the desired polarization. They present a simple, yet satisfactory solution to the polarization dependence of silicon waveguides. However, by using such devices, modes in unwanted polarizations are ultimately lost, and thus decrease the overall power efficiency.

Another approach is to employ the polarization-diversity scheme. The schematic for this scheme is shown in Fig. 1.4, where the two key components are the polarization beam splitter (PBS) and the polarization rotator (PR). A PBS first separates the input light (with arbitrary polarization state) into two orthogonally polarized beams, while a PR rotates the polarization state of one beam into its orthogonal counterpart (TM to TE, or vice versa), thus maintaining one polarization state throughout the signal processing circuit. A second PR is then used on the other arm to prevent signal interferences and to compensate loss. The resulting two orthogonal beams will then be recombined by a second PBS [7].

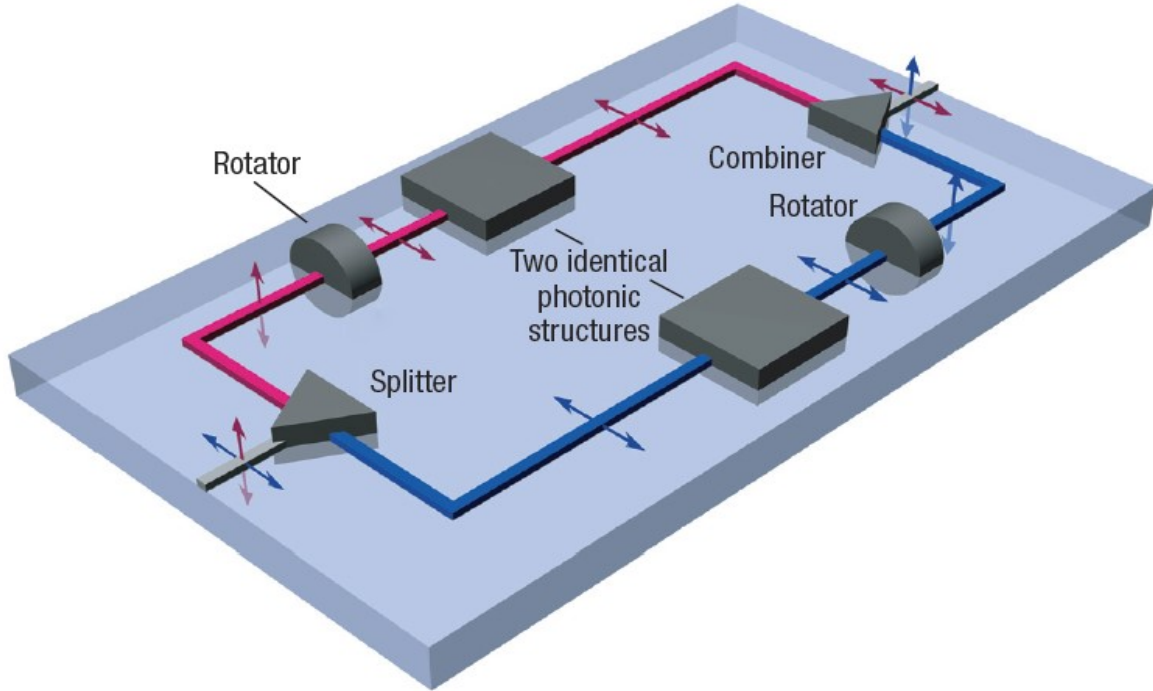


Fig.1. 5. Schematic of an integrated polarization-diversity scheme [6].

By employing this scheme, polarization-sensitive photonic devices can be rendered transparent to the input polarization over the entire operating wavelength range [7].

1.6 Polarization Rotation and Polarization Rotators

Rotation of a polarization state is achieved by rotating the optical axis of a silicon waveguide. This rotation can be done by either breaking the waveguide symmetry or employing tapered structures to rotate the polarization state in unison along the transition. A more detailed discussion on the operating principle of a PR is given in Chapter 2, along with a literature review on current PR designs

Polarization rotation and the polarization-diversity approach presented in Section 1.4 are of great interest for managing polarization-dependent circuits that support only single-mode

operation. For example, in mode-division multiplexing (MDM) technology, two orthogonal polarizations can be used simultaneously with the help of a polarization rotator array [8].

1.7 Thesis Objective and Organization

The goal of this thesis is to study and understand polarization rotators fabricated on the SOI platform. It involves the design, fabrication, and testing of two different polarization rotator designs based on periodic asymmetrical-loaded waveguide structures. Chapter 2 includes the literature review on polarization rotators and summarizes the numerical methods employed in the design process.

Chapter 3 presents the design and optimized simulation results for the two PR designs. The designs for both proposed structures are illustrated. Then the optimization of the design parameters are performed, followed by a performance evaluation based on the optimized parameters.

Fabrication preparation of the proposed designs are included in Chapter 4, along with a review on the fabrication technology being used. The design of the testing circuit, the mask layout of the proposed PRs, the testing method, and the experimental setup are explained.

Chapter 5 presents the experimental results. SEM images of the fabricated prototypes are included, and the normalization of the results are explained. These results are presented and compared to the simulated results at the end of the chapter.

Chapter 6 concludes this dissertation by reviewing the presented PR designs and outlining future work.

Reference

- [1] D. Xu, J. H. Schmid, G. T. Reed, G.Z. Mashanovich, D.J. Thomson, M. Nedeljkovic, X. Chen, D. V. Thourhout, S. Keyvaninia, and S.K. Selvaraja, “Silicon Photonic Integration Platform-Have We Found the Sweet Spot?”, IEEE Journal of selected topics in Quantum Electronics, Vol. 20, No.4, July/Aug 2014,
- [2] R. G. Hunsperger, “Integrated Optics, Chapter 2: Optical Waveguide Modes”, pp. 17-31, Springer, 2009
- [3] K. Yamada, “Silicon Photonics II, Chapter 1: Silicon Photonic Wire Waveguides: Fundamentals and Applications”, pp.1-29, Springer, 2011
- [4] R. A. Soref, J. Schmidtchen, and K. Petermann, “Large single-mode waveguides in GeSi-Si and Si-on-SiO₂,” IEEE J. Quantum Electron., vol. 27, pp. 1971–1974, 1991.
- [5] W.N. Ye, D.X. Xu, S.Janz, P.Cheben, M-J.Picard, B.Lamontagne, and N.G. Tarr, “Birefringence Control Using Stress Engineering in Silicon-on-Insulator (SOI) Waveguides”, Journal of Lightwave Technology, Vol.23, No.3, pp.1308-1318, Mar 2005
- [6] H. Fukuda, K. Yamada, T. Tsuchizawa, T. Watanabe, H. Shinojima and S. -I. Itabashi, “Polarization rotator based on silicon wire waveguides”, Opt. Express, 16(4), 2628-2635 (2008)
- [7] T. Barwicz, M. R. Watts, M. A. Popovic, P.T. Rakich, L. Socci, F.X. Kartner, E.P. Ippen and H.I. Smith, “Polarization-transparent microphotonic devices in the strong confinement limit”, Nature Photonics, Vol.1, pp.57-60, Jan 2007
- [8] Y. Xiong, “Silicon Photonic Devices for Sensing, Switching, Polarization and Mode Control”, Thesis submitted to the Faculty of Graduate and Postdoctoral Affairs, Department of Electronics, Carleton Univeristy, pp.19-20, Dec 2014

Chapter 2

Literature Review and Background

This chapter includes the literature review on polarization rotator (PR) designs and their operating principles. The simulation methodologies used in the design of the demonstrated PRs are illustrated.

Currently, the two major polarization rotation mechanisms used in integrated optics are mode-coupling based and mode-evolution based. The two mechanisms, and the demonstrated PR designs based on these mechanisms, are illustrated in the following sections.

The performance of a PR can be characterized by three parameters: extinction ratio (ER), polarization rotation efficiency (PRE), and insertion loss (IL). ER is defined as

$$ER_{(TE-TM)} = 10 \log \frac{P_{TE-TM}}{P_{TE-TE}} \quad (2.1)$$

Here, P_{TE-TM} is the power coupled to the TM-polarized mode at the output when the input polarization is TE. P_{TE-TE} is the residual power of the TE-polarized mode left at the output. A

positive ER means more than a half of the input mode's power is coupled to the orthogonally polarized mode at the output.

The PRE is a measure of the power transferred between the two orthogonally polarized beams at the output port. It is defined as

$$PRE (\%)_{TE-TM} = \frac{P_{TE-TM}}{P_{TE-TE} + P_{TE-TM}} \quad (2.2)$$

The last important measure is the IL, which is defined as

$$IL = 10 \log_{10} \left(\frac{P_{out}}{P_{in}} \right) \quad (2.3)$$

where P_{out} is the total power measured at the output, and P_{in} is the total power measured at the input.

2.1 Mode Evolution based Polarization Rotators (PRs)

Mode evolution based PRs were first proposed in [1]. They can be formed by twisting a waveguide or by depositing a tapered overlayer. In the mode rotating region, the launched fundamental mode becomes hybridized gradually as the width of one of the waveguide strips or the overlayer is gradually reduced. By matching the refractive indices between the input and the output, the two polarizations will be coupled by the asymmetric shape of the waveguide [2]. Thus, the input mode's polarization state will be rotated by the tapered layer.

PRs based on such mechanisms are generally fabrication tolerant. The drawback of this mechanism is that a long distance is required to obtain adiabatic mode conversion. When using plasmonic waveguide based designs, this would impose another problem: the long distance would accumulate large ohmic losses from the metal. Therefore, mode evolution based PR designs using

plasmonic waveguides cannot achieve good performance and a compact device footprint at the same time. Additionally, mode evolution based PR designs usually require uncommonly thick silicon waveguides or additional layers of material.

A twisted waveguide based mode evolution PR is demonstrated in [2]. It uses 400-nm-thick silicon as the waveguide core and silicon dioxide as the cladding layer. As shown in Fig.2.1, the input waveguide is vertical, the output waveguide is horizontal, and a transition region is placed in between.

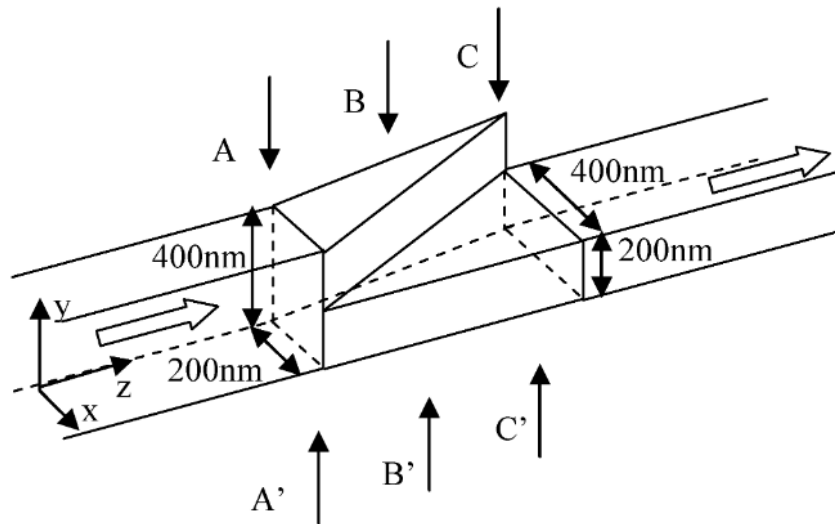


Fig.2. 1. Schematic of the mode evolution PR design in [10].

By matching the effective refractive index of the TE mode in the input waveguide to that of the TM mode in the output waveguide (and vice versa), rotation of the polarization state can be obtained. The prototype is fabricated by two-step dry etching. They achieve a 15-dB ER in a 40- μm -long device, with an IL of ~ 1 dB. The asymmetrical input/output waveguide imposes a difficulty when integrated into PICs.

A twisted waveguide structure using a silicon waveguide with an additional tapered Si_3N_4 overlayer based PR design is demonstrated in [3]. In the mode rotating section, the silicon waveguide gradually has its width increased, while the Si_3N_4 waveguide has its width decreased as it moves away from the silicon section. A mode adapter is used to transit the input from a regular silicon waveguide into the mode of the combined structure, where both Si and Si_3N_4 have the same width. Another mode adapter is used to connect the PR output to a regular silicon waveguide. The demonstrated device is 420- μm long, with a PRE of more than 90% and an IL less than 1 dB for an 80-nm wide wavelength range.

The PR design proposed in [4] uses a diagonally positioned amorphous silicon (a-Si) overlayer on top of a silicon wire waveguide based on the mode evolution principle. The a-Si layer and the silicon layer are separated by a thin etch-stop oxide layer. The schematic of this proposed design is shown in Fig.2.2 below.

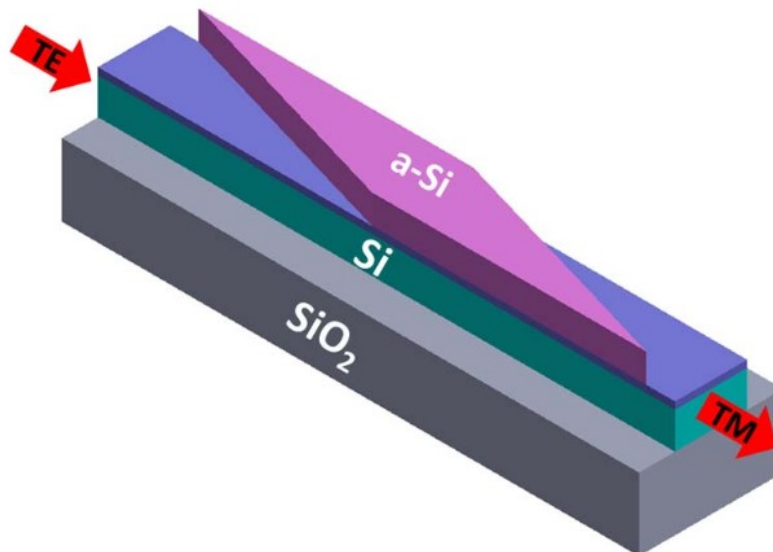


Fig.2. 2.Schematic of the PR design using an a-Si overlayer [12].

The width of the silicon waveguide and the a-Si overlayer remain constant, while the a-Si overlayer is tilted by an angle relative to the silicon waveguide. By simulation, they demonstrated a 17- μm PR with a PRE of over 90% for a wavelength range of 135 nm.

2.2 Mode Coupling Based Polarization Rotators (PRs)

2.2.1 General Approach in mode coupling based PRs

The mode coupling mechanism is based on mode beating behaviors between different modes introduced by breaking the waveguide symmetry. In the general approach, hybrid modes consisting of 50% TE and 50% TM polarization (two orthogonally polarized modes with 45° rotation in the optical axes, with respect to the x and y axes) need to be obtained. The two hybrid modes propagate along the device with different propagation constants (i.e., different speeds). The beat length of the two hybrid modes is defined as $L_b = \frac{\lambda}{\Delta n_{eff}}$, where Δn_{eff} is the effective index difference between the two modes and λ is the targeting wavelength. Constructive interference between the modes occur at each $0.5L_b$, thus resulting in a 90° polarization rotation at each $0.5L_b$. PR designs based on this principle can reach very compact device footprints, however, these devices are not fabrication tolerant.

An ultracompact polarization rotator design based on multiple subwavelength trenches with a conversion length as short as 10 μm has been demonstrated in [5] on the 260-nm SOI platform. In this design, the waveguide cross section symmetry is broken by two adjacent subwavelength trenches. The resulting fully hybrid modes consist of 50% TE and 50% TM. However, the fabrication of this device must be precise and use electron-beam lithography with high-contrast hydrogen silsesquioxane resist (HSQ). The trenches are to be formed by inductively coupled plasma-reactive ion etching (ICP-RIE).

Cut-corner structures have been used in [6] to break the waveguide symmetry and to induce fully hybrid modes. In a 25- μm -long device, a PRE of -0.85 dB (82%) has been achieved over a wavelength range of 30 nm. This design uses waveguide widths as narrow as 220 nm. It has high loss and requires a long taper to integrate the device into commercial photonic integrated circuits.

Slanted sidewall-based PRs have been demonstrated in [7]. In this design, the waveguide symmetry is broken by using air cladding and a sloped sidewall on one side of the waveguide. This device was fabricated by using dry plasma and wet chemical etching techniques. The demonstrated device obtained a peak TE–TM coupling efficiency of 75 % in a 3256- μm -long device.

PR designs based on slot waveguides have been demonstrated by simulation in [8]. The proposed design utilizes an adiabatic tapered vertical-slot waveguide that consists of straight and tapered silicon strips separated by 60-nm gaps. The slot waveguide has a low refractive index region sandwiched between two high refractive index regions. It enhances the light intensity in the slot region due to the large discontinuity of the electric field at interfaces with a high index contrast [8]. The mode conversion is based on the mode hybridization in the tapered strip, as the effective index of the tapered waveguide increases with increments to the strip width. By simulation, the proposed design achieves > 98% conversion efficiency over a ~100-nm wavelength range.

Another attempt to break the waveguide symmetry is by using off-axis double-core structures consisting of a silicon wire waveguide and a silicon-oxinitride waveguide [9]. In this design, the 200-nm-high Si wire core (first core) is used as the access waveguide, and the 840-nm-thick SiO_xN_y core (second core) is used to break the waveguide symmetry, as shown in Fig. 2.3.

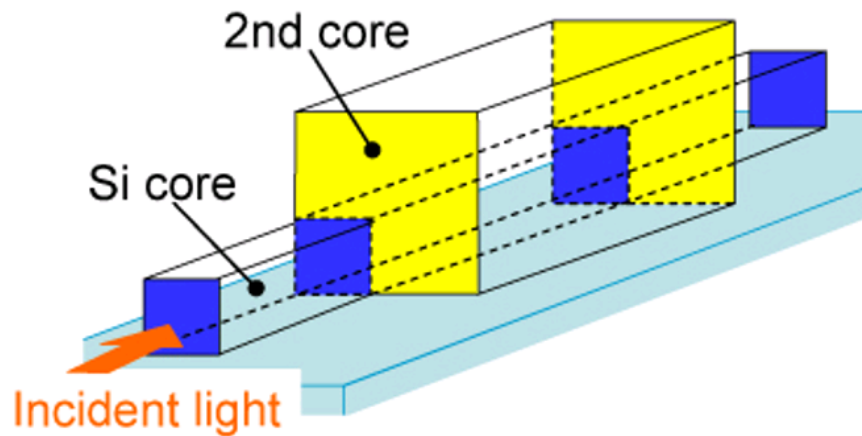


Fig.2. 3. Schematic of the demonstrated polarization rotation design [9].

The SiO_xN_y is deposited by plasma-enhanced chemical vapor deposition (PECVD), and the second core is formed by RIE with fluoride gas. They have achieved an 11-dB extinction ratio in a 35- μm -long device, with 1 dB of excess loss.

The symmetry of the waveguide can also be broken with the help of an overlayer made of different materials. In [10], a PR design with a polysilicon overlayer is demonstrated with a 220-nm-thick silicon layer, a 160-nm-thick polysilicon layer, and a 5-nm-thick thermally grown silicon dioxide layer (acting as an etch stop layer) in between. The fabrication was done by a 4-etching-step CMOS-compatible process. The polysilicon overlayer is formed by annealing previously deposited amorphous silicon. The demonstrated device achieves an 88.9 % conversion efficiency over a wavelength range of 80 nm, with a 7.6- μm effective conversion length.

Plasmonic waveguide based PR designs have been demonstrated by simulation in [11]. The waveguide symmetry is broken by using asymmetric claddings of silicon dioxide and metal, as shown in Figure.2.4.

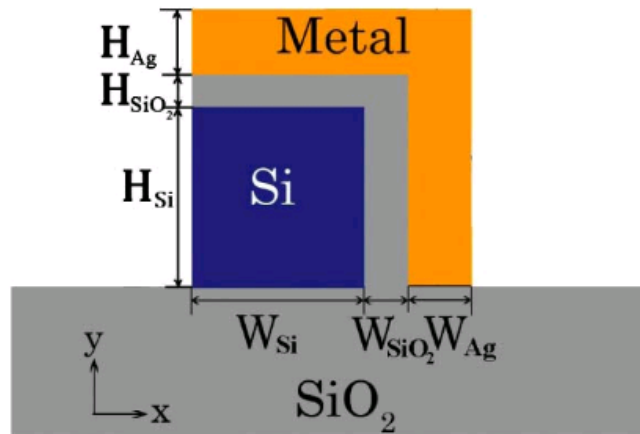


Fig.2. 4. Schematic cross section of the plasmonic waveguide based PR design [11].

Demonstrated by simulation, the device achieved a polarization conversion efficiency of 99.7% at a wavelength of 1.55 μm in a 9.7- μm -long device. However, the IL for this design is considerably high. By simulation, IL is found to be 2.2 dB at the peak wavelength.

Another plasmonic based PR design was demonstrated by simulation in [12]. It achieved a rotation efficiency of 99.5% at a 1.55- μm wavelength, and features a compact device footprint of 3.2 μm (in length). The hybrid plasmonic waveguides used have a silver cap, a thin low refractive index dielectric layer with a high refractive index dielectric layer. The use of a metal cap breaks the symmetry of the waveguide, making hybrid modes present in the waveguide. By simulation, the IL is found to be 1.38 dB.

2.2.2 Asymmetrical Periodic Loaded Structures

The PR designs presented in this thesis are based on asymmetrical periodic loaded structures. These structures can be viewed as a variation on the traditional mode coupling based PR structures. The difference is that, instead of using a single asymmetrical waveguide section to obtain fully hybrid modes (50% TE and 50% TM), this structure rotates the polarization state of the input light

based on periodically alternating asymmetrical waveguide sections that can obtain partially hybrid modes.

The first design of an asymmetrical periodic loaded waveguide based PR was demonstrated by Shani et al. [13] in 1991. It uses a 1.3- μm bandgap wavelength (1.3Q) material and InP. Fig. 2.5 shows the schematic of this design.

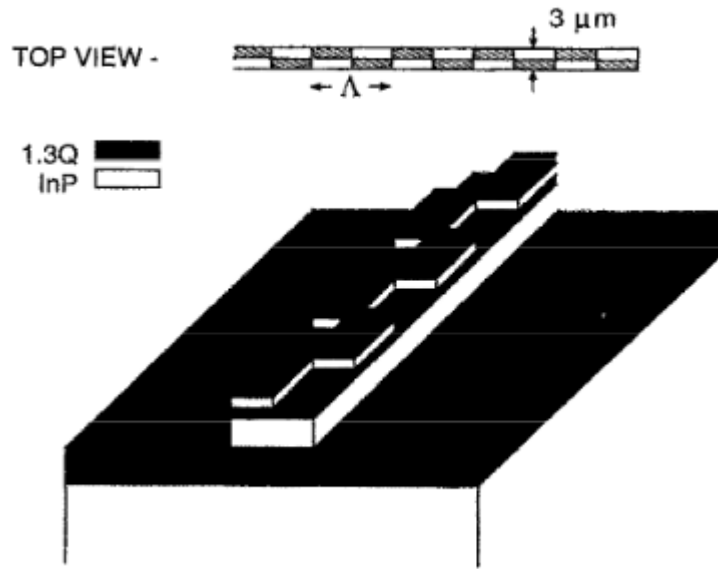


Fig.2. 5. Schematic of the first demonstrated PR based on asymmetrically periodic loaded structures [13].

By its name, this structure is formed by periodically alternating loaded waveguide sections on the left and right sides. As shown in Fig.2.5, Λ represents the length between alternations. The PR designs presented in thesis are based on this structure.

The PR design demonstrated in [13] achieves over 90% rotation efficiency in a 3.7-mm-long device, with a total insertion loss of 13 dB. PR designs based on asymmetrical periodic loaded structures have also been demonstrated, by simulation and experiment, on III-V material (GaAs, InP, etc.) platforms [14][16-17]. Demonstrated by experiment, the PR design in [14] achieves a

peak extinction ratio of 16 dB in a 1500- μm -long device, with a 12-dB insertion loss. By simulation only, the PR design proposed in [16] achieves full conversion in a 900- μm -long device; while the PR design proposed in [17] achieves 98% rotation in a 740- μm -long device.

The polarization conversion of PRs using asymmetrical periodic loaded structures is based on the mode-beating behavior and the coupling between the periodic asymmetrical sections. The physical principle of the PR is that the geometric mismatch introduced by the waveguide asymmetry is responsible for the cross-coupling between the two polarizations. This is different from mode coupling based PR designs since there is no need to obtain fully hybrid modes by breaking the waveguide symmetry. In other words, for mode coupling based PRs, the rotation of the optical axis needs to be exactly 45° . Here, the asymmetric waveguide cross-section of each mismatched segment introduces a rotation ϕ to the optical axis along the direction of propagation. When the length of a single perturbed section is half of L_b , constructive interference between the two modes will occur; leading to a $+2\phi$ rotation of the polarization state at the output of the waveguide. Fig. 2.6 shows an example of how the polarization state rotates in one full period of the asymmetrical waveguide sections, where θ is the total rotation angle to the input. Assuming that a TE mode is being launched from the left side, the polarization state of the mode at location (i) will be $\theta = +2\phi$, given that the right perturbed waveguide offers a $+\phi$ rotation to the optical axis (Fig. 2.6 (a)). As shown in Fig.2.6 (b), the mode has a 3ϕ rotation with respect to the optical axis of the left perturbed waveguide section, where a $-\phi$ rotation to the optical axis is induced by the waveguide asymmetry at location (i). At location (ii), the polarization state of the mode will be rotated by -6ϕ . The final resulting mode has a -4ϕ rotation angle compared to the initial TE input.

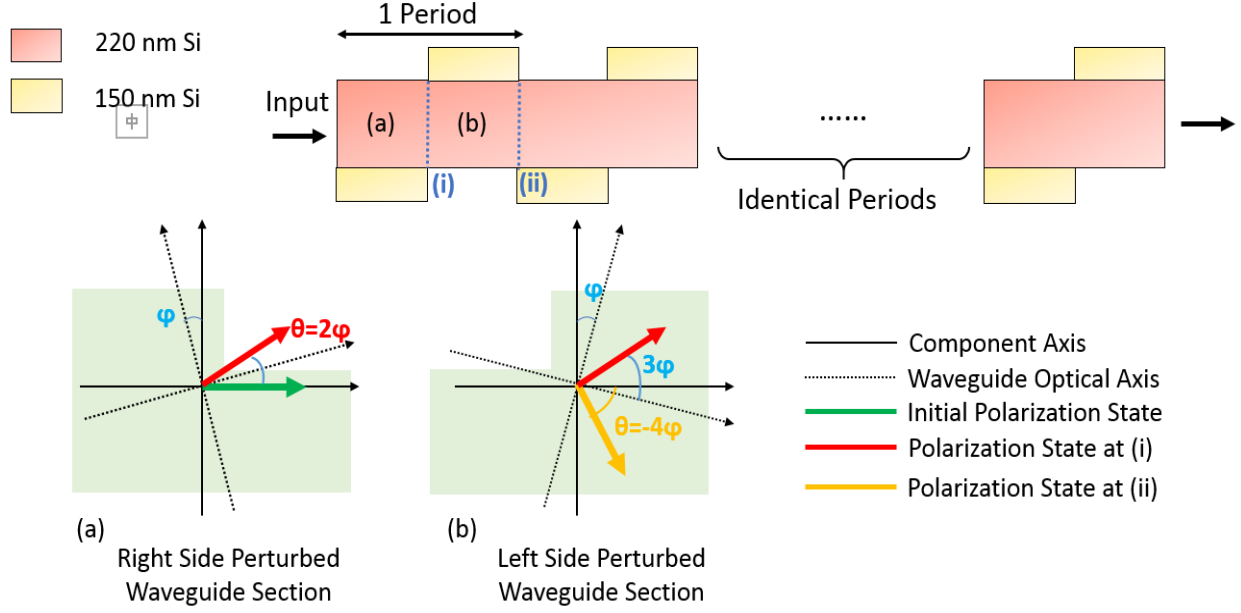


Fig.2. 6 Polarization Rotation in one period of left and right side perturbed waveguide sections.

If the length of each perturbed section L_s is chosen to match half of L_b (i.e., $L_s = 0.5L_b$), after repeating N alternations of left and right side perturbed sections, the polarization of the input mode will be rotated by an angle θ , where

$$\theta = (-1)^N 4N\varphi. \quad (2.4)$$

By matching the phases of the two orthogonal modes in the asymmetric loaded waveguide, polarization rotation of any angle can be achieved [14-15].

Efforts have been made to combine asymmetrical periodic loaded polarization rotators with Bragg diffraction effects in SOI waveguides in [18-19]. Since Bragg gratings are resonant structures, the resulting devices are wavelength selective (~ 1490 nm in [18] and ~ 1468 nm [19]). In addition, these devices have large footprints (~ 1000 μm in [18] and 308 μm in [19]).

This structure is interesting, especially for the 220-nm SOI platform, where no fully hybridized modes need to be obtained. The 220-nm SOI platform is so thin that many of the asymmetrical

waveguide structures used in mode coupling based PRs on thicker platform cannot be applied here to obtain fully hybrid modes. By using the asymmetrical periodic loaded structures, mode coupling mechanism based PRs can be designed on 220-nm SOI without using narrow waveguides [6] or additional materials with different refractive indices [10].

2.3 Simulation Methods

Three commercial software programs are used to simulate the theoretical designs of the demonstrated PRs: Fimmwave® and Fimmprop® from Photon Design, and FDTD Solutions® from Lumerical Inc. These are based on several numerical analysis techniques, including the film mode matching (FMM) method, the finite-difference method (FDM), the eigenmode expansion method (EME), and the finite-difference time-domain (FDTD) method. These numerical methods are based on numerical approximations of Maxwell's equations, done in slightly different ways. The unique advantages/disadvantages of these methods are described and illustrated in the sections below.

2.3.1 Film Mode Matching Method

The film mode matching method is available in Fimmwave. It is used to provide accurate mode propagation constants and mode profiles. Over the computational domain, the user-defined arbitrary waveguide structure is described by a list of vertical slices. Each of these slices are uniform horizontally and consist of a number of vertical layers. Fig.2.7 shows an example of the FMM treatment of an SOI rib waveguide.

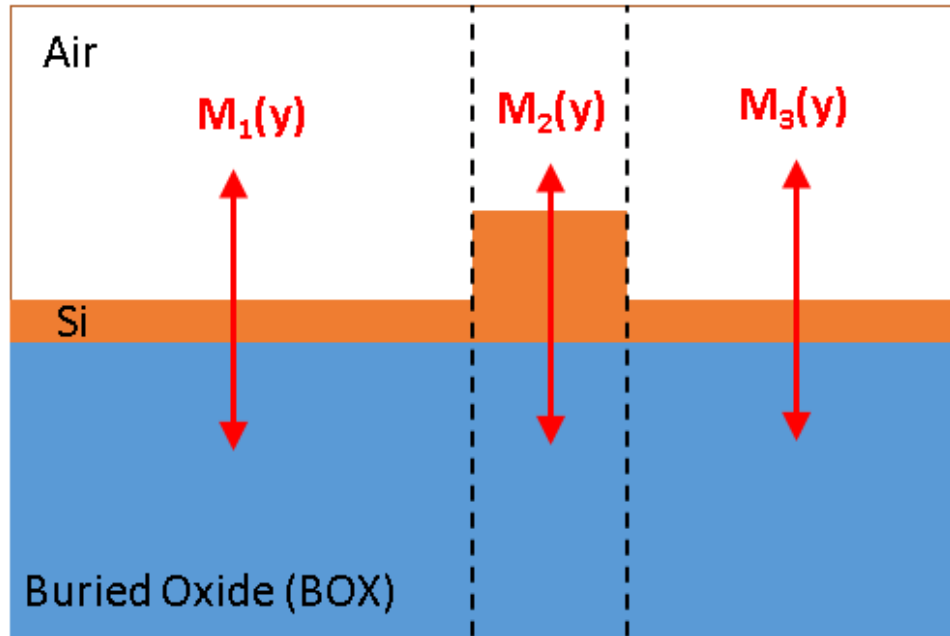


Fig.2. 7. An example of an SOI rib waveguide under the FMM treatment.

$M_N(y)$ represents the 1D modes of the Nth slice. Based on the TE and TM 1D modes in each slice, a 2D mode is built up [20]. The modelled area may be bound by either perfect metallic or magnetic walls. Theoretically, this method exacts an infinite number of 1D modes [21].

In Fimmwave's FMM solver, the degree of accuracy is proportional to the number of modes solved in each slice. The simulation time is mainly based on the number of slices in the defined structure, and is slightly increased with an increase to the number of layers in each slice. The solver is fully vectorial, allowing for the observation of different effects (e.g., the optical leakage of the minority field). It is considered to be the optimal solver for waveguides with a rectangular geometry and a well-defined interface, which is typically the case for rib and wire waveguides [21].

2.3.2 Finite Difference Method

The finite difference method (FDM) is the simplest numerical method. It has an almost fully numerical approach and is available in Fimmwave.

The FDM setup process is generally started by establishing a 2D mesh grid over the computational domain. An appropriate finite-difference formula is then selected to approximate all the differentials; where the boundary conditions are defined by electric or magnetic walls. By assembling the equations into a linear system, the modes of the computed structure can be found [22].

The FDM solver in Fimmwave is ideal for simulating absorbing devices and metallic waveguides. It is also very helpful in silicon photonics, as it can model waveguides with high-step refractive index profiles, slanted or curved interfaces, and gradient profiles [23].

Compared to FMM, FDM is more capable of accurately simulating waveguide structures with slanted or curved interfaces. However, FMM has a shorter simulation time, since its solution is analytic along one axis. In addition, the eigenvalue problem in FDM is linear, making it more efficient than FMM when many modes need to be found.

2.3.3 Eigenmode Expansion Method

The eigenmode expansion method (EME) is available in Fimmprop®. It is a powerful method of simulating the electromagnetic propagation along a single axis of long and uniform structures. Each section of the user defined device is treated as a subcomponent of a larger device. Electromagnetic fields are represented in terms of basis sets of local modes for each section. These

modes can be obtained by either FDM or FMM, based on whichever is appropriate for the section selected. Joints are introduced between every two waveguide sections with different structures, in which the overlapping between modes is calculated. The algorithm calculates the bidirectional transmission and coupling for each possible input mode through the sections and joints of the device [24]. This approach has the ability to solve all inputs simultaneously. Fig. 2.8 shows an example of a multimode interference (MMI) coupler modeled by EME.

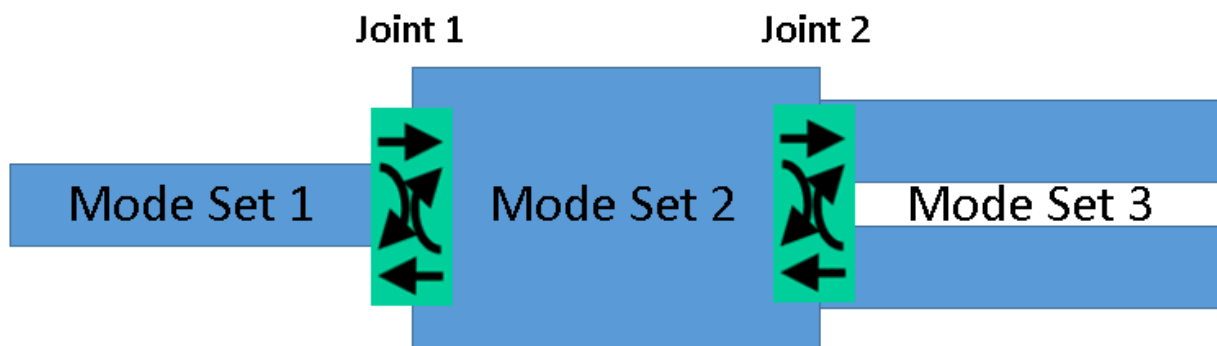


Fig.2. 8. An MMI coupler modeled by EME.

In addition, this method can be used to efficiently simulate structures with identical repeating sections, since the overlap integrals at the repeated joints will be the same [25].

2.3.4 Finite-Difference Time Domain Method

The finite-difference time domain method (FDTD) is available in FDTD Solutions®. This method was first proposed by K.S. Yee, in 1966 [26]. Due to advancements made in computer hardware, it is now a popular method to numerically simulate the propagation of light in 2D and 3D structures. This method models Maxwell's curl equations in the time domain, where light propagation is modeled into expressions for all 6 field components (E_x , E_y , E_z , H_x , H_y , and H_z) within a 3D computational volume. FDTD uses Yee's scheme to define these components. The

3D mesh over the computational domain is formed by discretizing the volume of interest equidistantly into rectangular cells. Time is also discretized into equal intervals. The derivatives in the curl equations are evaluated by using finite-difference approximations based on this mesh [27]. FDTD Solutions uses an auto-generated conformal Yee mesh, which adjusts the spacing between grid points. By using more grid points at important boundaries, while using fewer points when away from the modal power, this approach provides a more accurate calculation within less time.

FDTD is entirely numerical and does not require preprocessing Maxwell's equations. Compared to EME, it can model complex 3D structures, inhomogeneous materials, anisotropy, and nonlinear materials more easily. However, simulations are generally longer and require more memory, since every field component at every mesh point needs to be calculated.

References:

1. M. R. Watts and H. A. Haus, "Integrated mode-evolution-based polarization rotators", *Opt. Lett.*, 30(2), 138-140 (2005).
2. J. Zhang, M. Yu, G. -Q. Lo, and D. -L. Kwong, "Silicon-waveguide-based mode evolution polarization rotator", *IEEE J. Sel. Top. Quantum Electron.* 16(1), 53-60 (2010).
3. L. Chen, C. R. Doerr, and Y. -K. Chen, "Compact polarization rotator on silicon for polarization diversified circuits", *Opt. Lett.*, 36(4), 469-471 (2011).
4. Y. Xiong, D.-X. Xu, J. H. Schmid, P. Cheben, S. Janz and W. N. Ye, "Robust silicon waveguide polarization rotator with an amorphous silicon overlayer", *IEEE Photon. J.*, 6(2), 2200308 (2014).
5. A. V. Velasco, M. L. Calvo, P. Cheben, A. Ortega-Monux, J. H. Schmid, I. M. Fernandes, J. Leopoite, M. Vachon, S. Janz and D.-X. Xu, "Ultracompact polarization converter with a dual subwavelength trench built in a silicon-on-insulator waveguide", *Opt. Lett.*, 37(3), 365-367 (2012).
6. M. Amer, A. M. Gutierrez, A. Brimont, D. Vermeulen, G. Roelkens, J. M. Fedeli, A. Hakansson and P. Sanchis, "CMOS compatible silicon-on-insulator polarization rotator based on symmetry breaking of the waveguide cross section", *IEEE Photon. Technol. Lett.*, 24(22), 2031-2034 (2012).
7. C. Brooks, P. E. Jessop, H. Deng, D. O. Yevick and G. Tarr, "Passive silicon-on-insulator polarization-rotating waveguides", *Opt. Eng.*, Vol. 45, No. 4, 44603, Apr. 2006..
8. Y. Fei, L. Zhang, T. Cao, Y. Cao, and S. Chen, "High efficiency broadband polarization converter based on tapered slot waveguide", *IEEE Photon. Technol. Lett.*, 25(9), 879-881 (2013).
9. H. Fukuda, K. Yamada, T. Tsuchizawa, T. Watanabe, H. Shinojima and S. -I. Itabashi, "Polarization rotator based on silicon wire waveguides", *Opt. Express*, 16(4), 2628-2635 (2008).
10. D. Vermeulen, S. Selvaraja, P. Verheyen, P. Absil, W. Bogaerts, D. V. Thourhout and G. Roelkens, "Silicon-on-insulator polarization rotator based on a symmetry breaking silicon overlay", *IEEE Photon. Technol. Lett.*, 24(6), 482-484 (2012).
11. L. Jin, Q. Chen and L. Wen, "Mode-coupling polarization rotator based on plasmonic waveguide", *Opt. Lett.*, 39(9), 2798-2801 (2014).
12. L. Gao, Y. Huo, J. S. Harris and Z. Zhou, "Ultra-compact and low-loss polarization rotator based on asymmetric hybrid plasmonic waveguide", *IEEE Photon. Technol. Lett.*, 25(21), 2081-2084(2013).
13. Y. Shani, R. Alferness, T. Koch, U. Koren, M. Oron, B. I. Miler and M. G. Young, "Polarization rotation in a symmetric periodic loaded rib waveguides", *Appl. Phys. Lett.*, Vol. 59, No. 11, Pp. 1278-1280, Sept. 1991.
14. T. Mangeat, L. Escoubas, F. Flory and L. Roussel, "Integrated polarization rotator made of periodic asymmetric buried Ta₂O₅/silica sol-gel waveguides", *Opt. Express*, 15(19), 12436-12442(2007).
15. W. Huang and Z. M. Mao, "Polarization rotation in periodic loaded rib waveguides", *J. Lightwave Technol.*, 10(12), 1825-1831 (1992).

16. J. J. G. M. Van Der Tol, F. Hakimzadeh, J. W. Pedersen, D. Li and H. Van Burg, "A new short and low-loss passive polarization converter on InP", *IEEE Photon. Technol. Lett.*, 7(1), 32-34(1995).
17. S. S. A. Obayya, B. M. A. Rahman, and H. A. El-Mikati, "Vector Beam Propagation Analysis of Polarization Conversion in Periodically Loaded Waveguides", *IEEE Photon. Technol. Lett.*, 12(10), 1346-1348(2000).
18. H. Okayama, Y. Onawa, D. Shimura, H. Yaegashi, and H. Sasaki, "Polarization rotation Bragg grating using Si wire waveguide with non-vertical sidewall", *Opt. Express* 22(25), 31371-31378 (2014).
19. H. Yun, J. Flueckiger, Z. Chen, Y. Wang, L. Chrostowski, and N. A.F. Jaeger, "A wavelength-selective polarization rotating reflector using a partially-etched asymmetric Bragg grating on an SOI strip waveguide", *IEEE Group IV Photonics Conference*, Vancouver, BC (2015)
20. A Sv Sudbo, "Film mode matching: a versatile numerical method for vector mode field calculations in dielectric waveguides", *Pure Appl. Opt.: J. Euro. Opt. Society Part A*, 2(3), 211(1993).
21. Photon Design, "FIMMWAVE: The FMM Solver", http://www.photond.com/products/fimmwave/fimmwave_features_21.htm, Sept, 2015
22. P. Berini, "Numerical Methods in Electromagnetic Engineering", ELG 5379 Course Notes, Section 7
23. Photon Design, "FIMMWAVE: The FDM Solver", http://www.photond.com/products/fimmwave/fimmwave_features_22.htm, Sept, 2015
24. Photon Design, "FIMMPROP: How FIMMPROP works", http://www.photond.com/products/fimmprop/fimmprop_introduction_10.htm, Sept, 2015
25. D. F. G. Gallagher and T. P. Felici, "Eigenmode Expansion Methods for Photonics- Pros and Cons," in *Photonics West*, 2003, pp. 1–14
26. K. S. Yee, "Numerical Solution of Initial Boundary Value Problems Involving Maxwell's Equations in Isotropic Media," *IEEE Transactions on Antennas and Propagation*, vol. 14, no. 3, pp. 302–307, 1966.
27. P. Berini, "Numerical Methods in Electromagnetic Engineering", ELG 5379 Course Notes, Section 7.5

Chapter 3

Design and Parameter Optimization

3.1 Overview of Chapter 3

This section includes numerical demonstrations of two polarization rotator designs based on asymmetric periodic loaded SOI waveguides. Simulation results are obtained by using Lumerical's FDTD Solutions® and Photo Design's Fimmwave® and Fimmprop®. These use the FDTD and EME numerical analysis methods, respectively. As described in Chapter 2, the EME method is more time-efficient for long-waveguide simulations, while the FDTD method is more accurate for complicated photonic structures. Parameter optimization was done by EME and cross-checked by FDTD. The simulated performances of the reported devices were obtained by FDTD.

3.2 First Polarization Rotator Design

3.2.1 Device Structure

The schematic of the first design is illustrated in Fig.3.1. The structure is formed by a rib waveguide with longitudinally periodic perturbations (loadings) in the slab section of the waveguide, where the periodic loadings on the left and right sides are mismatched. The width of

the waveguide slab is represented by W_s , the width of the core is represented by W_c , and each perturbed section has a slab length of L_s . The structure is formed by repeating the alternation of the left and right slab perturbations for N periods. The device can be realized in a simple two-step etching process, where one shallow etch is required to form the periodic loadings on either side of the slab, followed by one full etch to define the core.

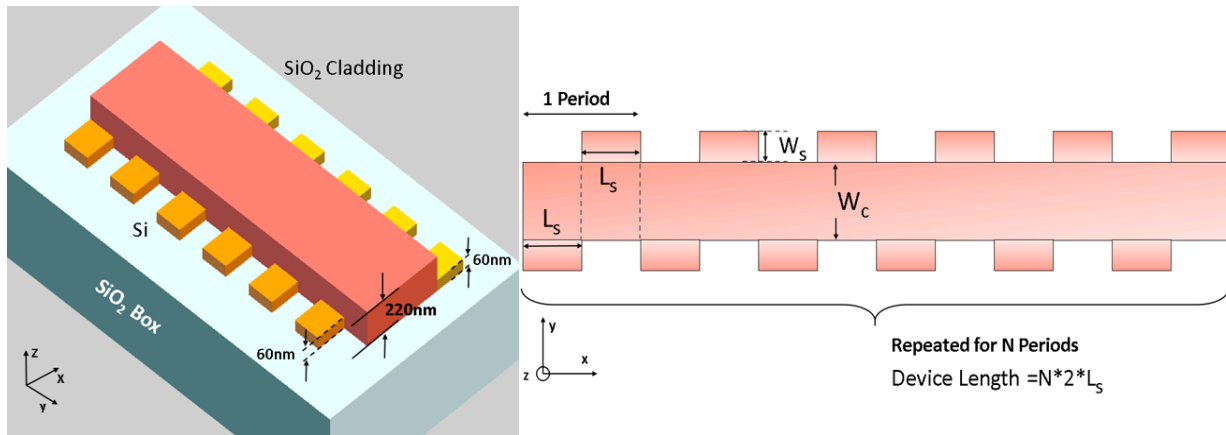


Fig.3. 1. Top view and structure (inset diagram) of the proposed polarization rotator design.

Based on the explanation of the operating principle given in Chapter 2, L_s is chosen to be half of the beat length between TE and TM-like modes.

3.2.2 Device Optimization

In the simulations, we focus on the C-band wavelengths (1530 nm–1565 nm) with both quasi-TE and quasi-TM input modes. The refractive index of Si and the surrounding cladding is assumed to be $n_{Si}=3.476$ and $n_{SiO_2}=1.444$, respectively. Due to the limitations of the available foundry service (IMEC, for example), the thicknesses of the waveguide core and slab are chosen to be 220 nm and 60 nm, respectively.

Our design optimization maximizes the performance parameter extinction ratio (ER) of the proposed polarization rotator; it is defined as

$$ER_{(TE-TM)} = 10 \log \frac{P_{TE-TM}}{P_{TE-TE}} . \quad (3.1)$$

P_{TE-TM} is the power coupled to the TM-polarized mode at the output when the input polarization is TE. P_{TE-TE} is the residual power of the TE-polarized mode left at the output. A positive ER means that more than a half of the input mode's power is coupled to the orthogonally polarized mode at the output. A negative ER value means that less than a half of the input mode's power is coupled to the orthogonally polarized mode at the output. Due to the operating principle of the proposed PR design, the TE-to-TM and TM-to-TE mode conversions are reciprocal.

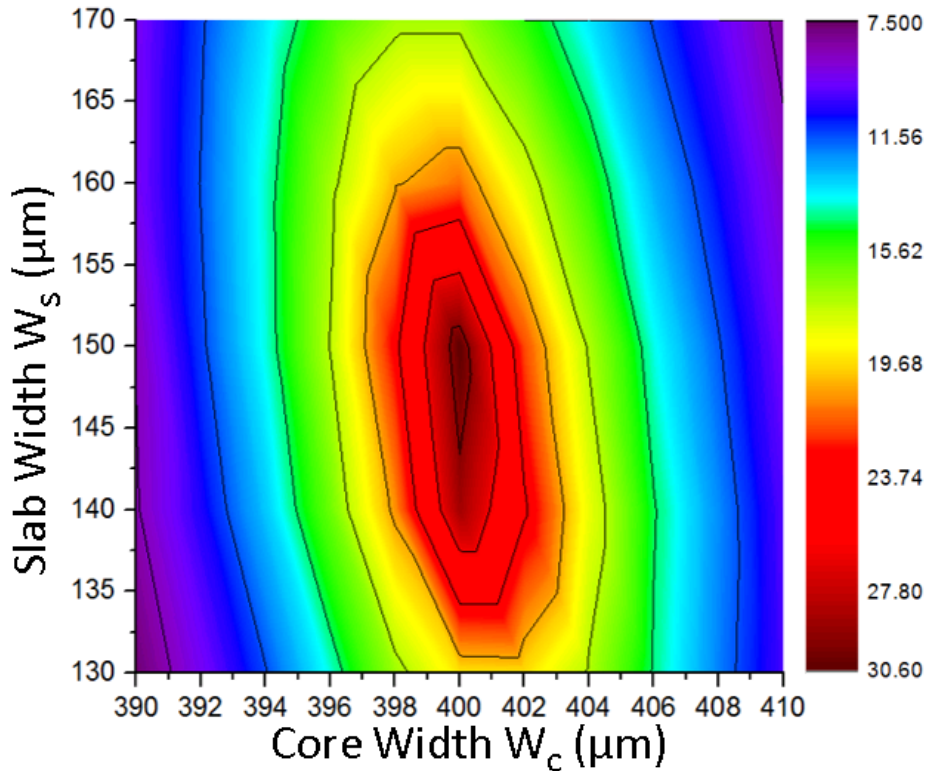


Fig.3. 2. EME calculation of ER as a function of waveguide core width (W_c) and slab width (W_s).

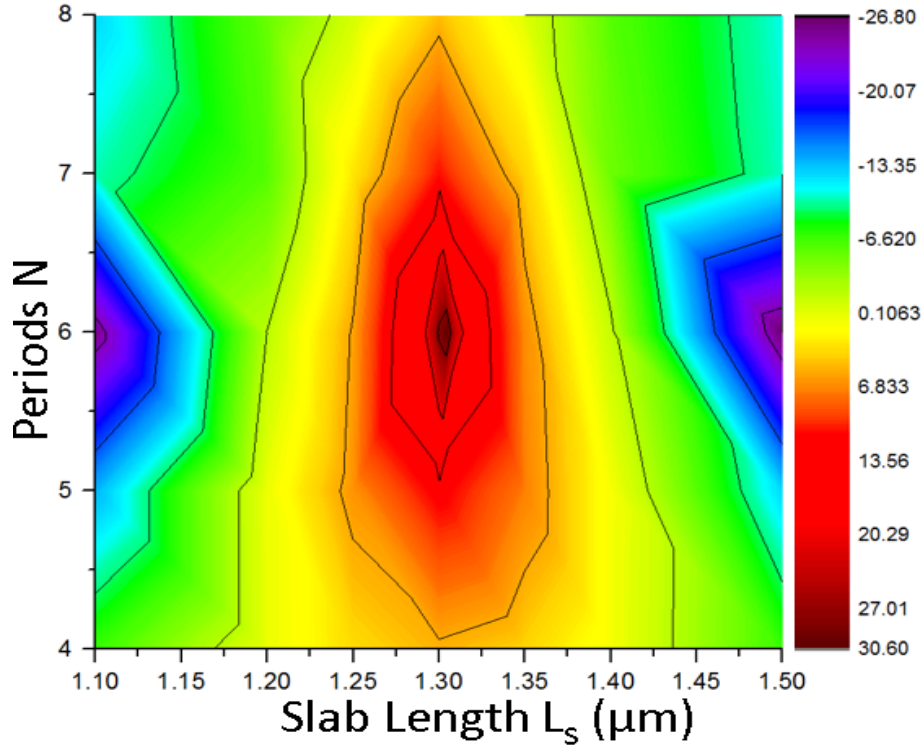


Fig.3. 3. EME calculation of ER as a function of slab length (L_s) and the number of periods (N).

For a given access-waveguide height of 220 nm, and a slab height of 60 nm, the rotator performance depends on the geometrical parameters W_c , W_s , L_s , and the number of periods N . To determine the optimal core and slab width W_c and W_s , we first fix $L_s=1.315 \mu\text{m}$ and $N=6$. Fig. 3.3 shows the calculated ER as a function of W_c and W_s . The best ER (30.6 dB) is found when $W_c=0.4 \mu\text{m}$ and $W_s=0.15 \mu\text{m}$. The calculated ER is over 20 dB for $W_c=0.4 \mu\text{m} \pm 0.003 \mu\text{m}$ and $W_s=0.15 \mu\text{m} \pm 0.015 \mu\text{m}$. Our PR design works within reasonable fabrication deviations ($\pm 10 \text{ nm}$). Next we determine the optimal value of L_s and N by fixing $W_c = 0.4 \mu\text{m}$ and $W_s = 0.15 \mu\text{m}$. Fig. 4 shows ER as a function of N and L_s , where the best ER (30.60 dB) is found when $L_s=1.315 \mu\text{m}$ and $N=6$. The calculated ER is over 20 dB within the L_s range of $1.275 \mu\text{m}$ to $1.325 \mu\text{m}$ for $N=6$.

We then perform fabrication tolerance analysis on slab and core thickness. Fig. 3.4 presents the calculated ER as a function of these thicknesses, with W_c , W_s , L_s , and N being fixed. The

calculated ER is over 20 dB for a core thickness of 220 nm \pm 5 nm and a slab thickness of 60 nm \pm 6 nm. Because the operation of this device is based on breaking the symmetry at the waveguide cross section, the device's performance remains optimal for core-and-slab thickness combinations as large as (225 nm, 68 nm), and as small as (215nm, 50nm). Note that the contour plots are not perfectly smooth. This is due to being based of individual data points obtained from the EME calculations.

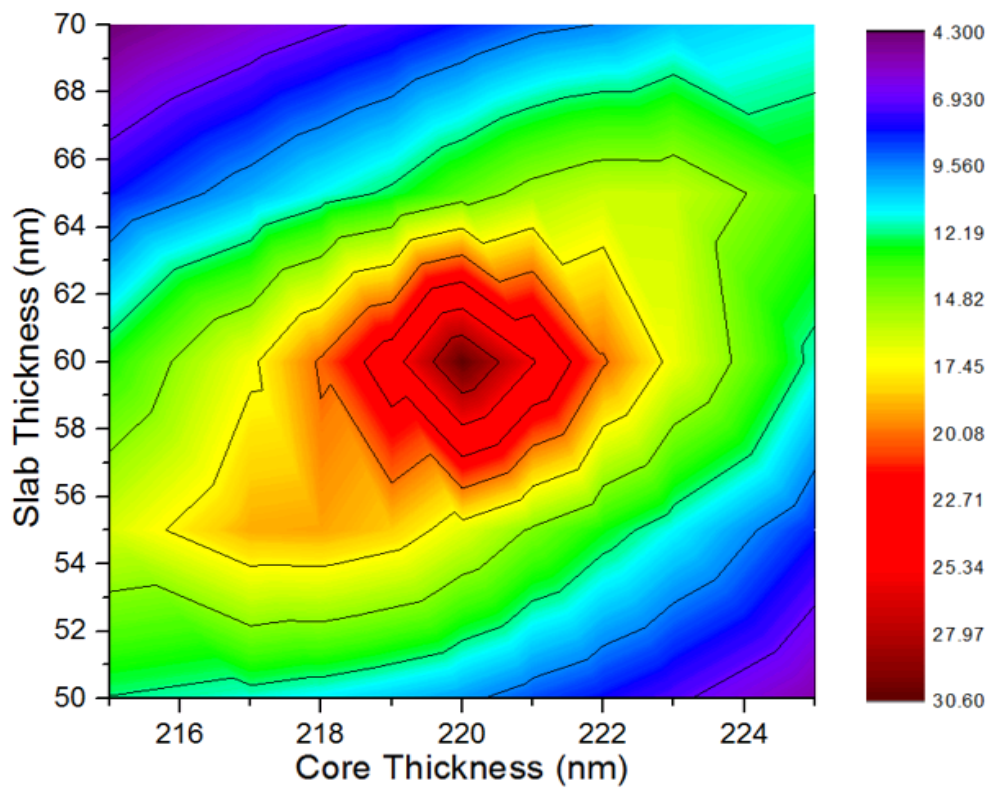


Fig.3. 4. EME calculation of ER as a function of slab and core thicknesses.

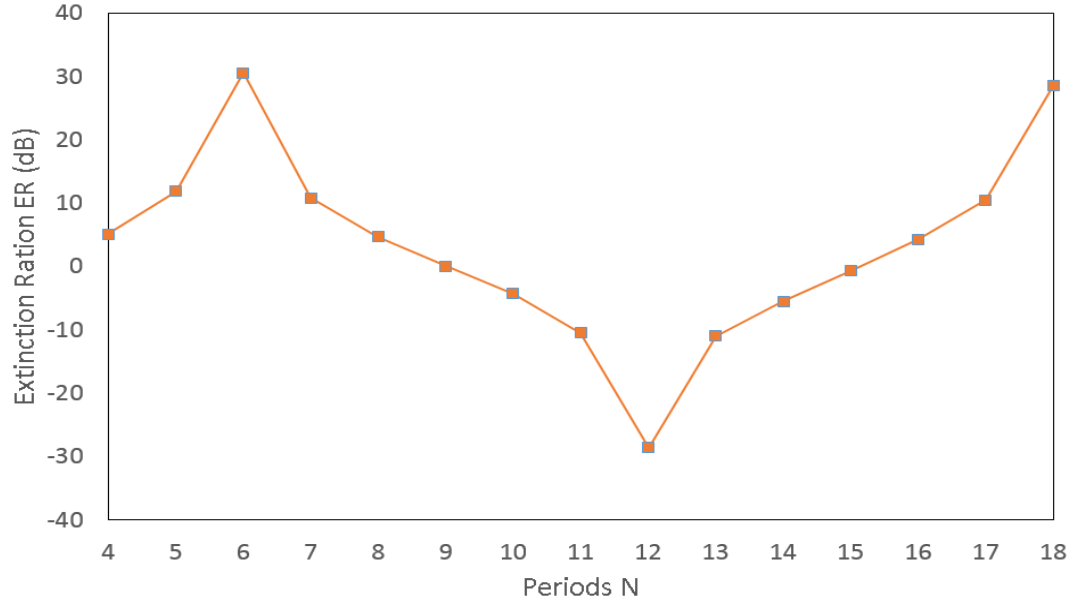


Fig.3. 5. ER as a function of the number of perturbed slab section alternation periods N. $W_c=0.4 \mu\text{m}$, $W_s=0.15 \mu\text{m}$, and $L_s=1.315 \mu\text{m}$.

Fig.3.5 plots the EME calculation of ER as a function of N, with a given set of optimized parameters ($W_c=0.4 \mu\text{m}$, $W_s=0.15 \mu\text{m}$, and $L_s=1.315 \mu\text{m}$). The highest ER (30.60 dB) is found when $N=6$; which results in a total device length of $15.78 \mu\text{m}$. The lowest ER is found when we double the periods of the proposed device, while the device achieves the highest ER once again when N is tripled. These observations agree with the previously described operating principle of the device.

3.2.3. Performance Evaluation

TABLE 3. 1. SUMMARY OF OPTIMIZED GEOMETRICAL PARAMETERS

Core Thickness (μm)	Slab Thickness (μm)	W_c (μm)	W_s (μm)	L_s (μm)	N	Device Length (μm)
0.22	0.06	0.4	0.15	1.315	6	15.78

Based on the optimized parameters, we cross-checked the EME-based simulation results by 3D-FDTD. Fig. 3.6 shows the conversion of the E_x and E_y electrical field components of the

waveguide mode. Fig. 3.6 (a) and (b) show that, as the TE-polarized input mode propagates along the device, the E_x component attenuates to zero before reaching the output. The E_y component appears and eventually dominates at the output. Similarly, for a TM-polarized input mode, the polarization rotation phenomenon can be observed in Fig. 3.6 (c) and (d): as the input mode is gradually rotated through its propagation, the predominant E_y component disappears and the output shows the E_x component.

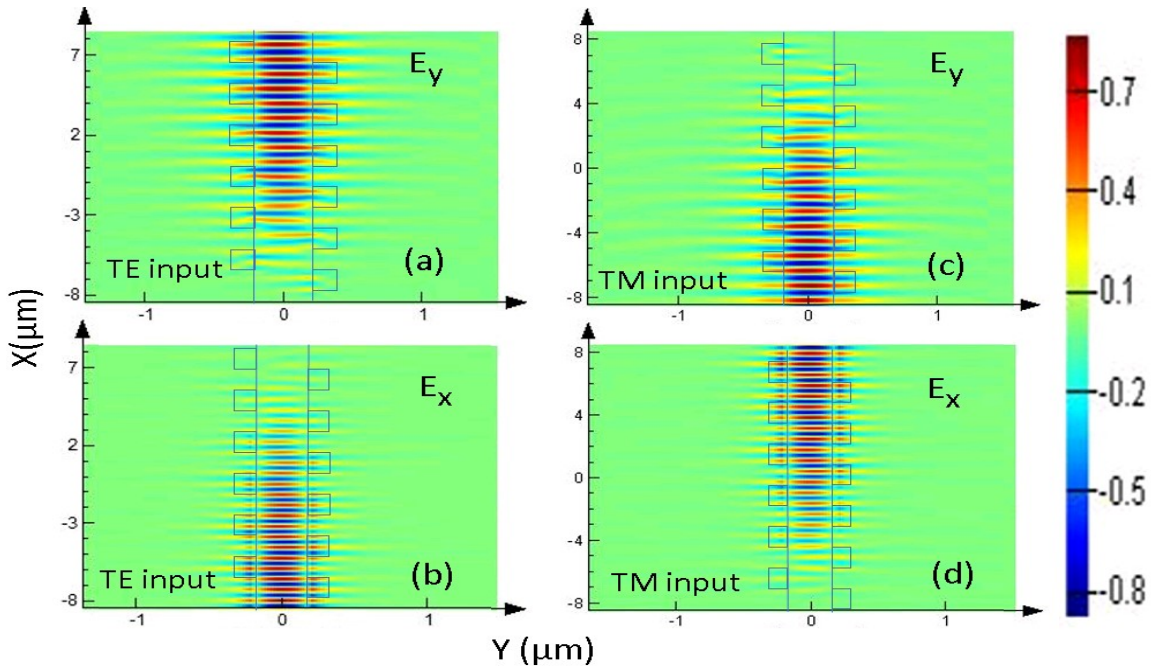


Fig.3. 6. Transverse electric field components E_x and E_y along the proposed polarization rotator design (top view) for TE (a), (b) and TM (c), (d) polarization inputs.

Based on the optimized geometrical parameters in Table 3.1, we examine the performance of our proposed rotator design with the 3D-FDTD method. Fig. 3.7 shows the ER as a function of wavelength, for both the TE and TM inputs. The peak ER for the TE-to-TM conversion is 25.45 dB at a wavelength of 1549 nm, while the peak ER for the TM-to-TE conversion is 25.01 dB at 1553 nm. At a wavelength of 1550 nm, the ER is 25.38 dB and 24.12 dB for the TE-to-TM and TM-to-TE conversions, respectively. It is also observed that the simulated ER is >10 dB for both the TE-to-TM and TM-to-TE conversions across the entire C-band.

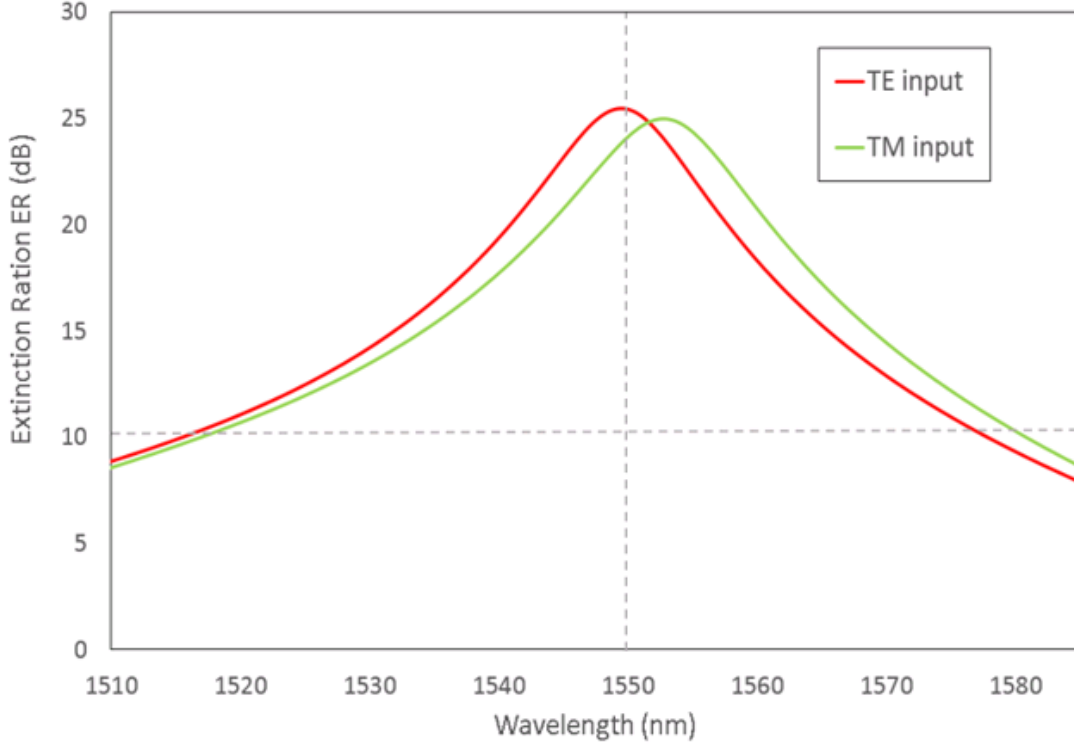


Fig.3. 7. Wavelength dependence of extinction ratio (ER) for TE and TM polarized inputs, calculated by 3D-FDTD.

Fig. 3.8 illustrates the polarization rotation efficiency (PRE) as a function of wavelength, where PRE measures the power transferred between the two orthogonally polarized beams at the output port, as defined by

$$PRE (\%)_{TE-TM} = \frac{P_{TE-TM}}{P_{TE-TE} + P_{TE-TM}} \quad (3.2)$$

The calculated PRE is above 90% over a wavelength range of 1514 nm to 1579 nm, centered at ~1550 nm for both the TE and TM inputs. The peak PRE for the TE-to-TM conversion is 99.72%, at 1549 nm, while the peak PRE for the TM-to-TE is 99.68%, at 1553 nm. At a wavelength of 1550 nm, the PRE is 99.7% and 99.61% for the TE-to-TM and TM-to-TE conversion, respectively.

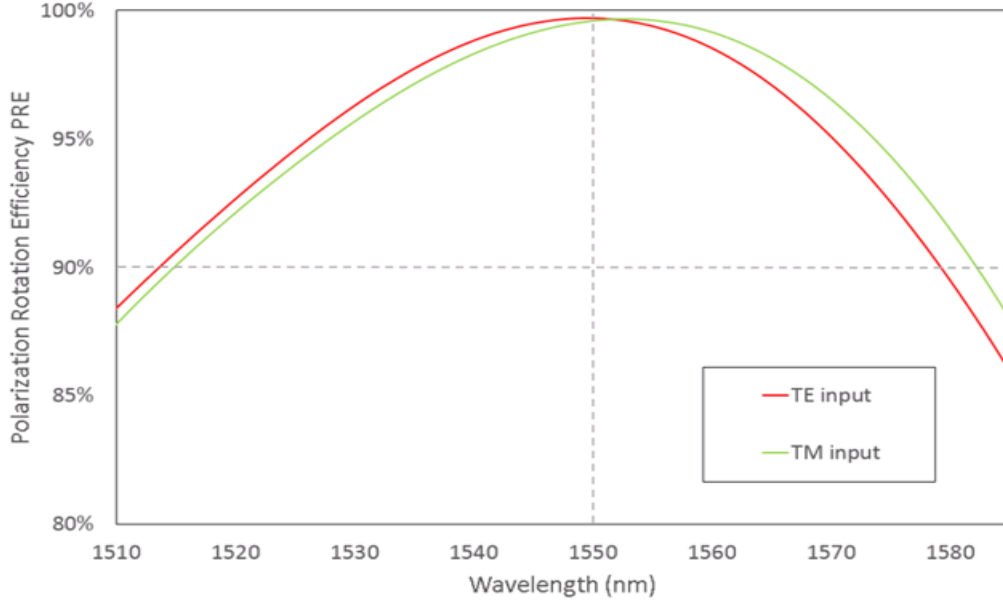


Fig.3. 8. Wavelength dependence of polarization rotation efficiency (PRE) for TE and TM polarized inputs, calculated by 3D-FDTD.

Finally, we examine the loss of the proposed rotator structure. The insertion loss (IL) is define by

$$IL = 10 \log_{10} \left(\frac{P_{out}}{P_{in}} \right) \quad (3.3)$$

where P_{out} is the total power measured at the output, and P_{in} is the total power at the input. Fig. 3.9 shows the simulated IL as a function of wavelength for the proposed design. Unlike the previously proposed PR designs based on asymmetrical periodic loaded structures [1-4], we address the critical issue of the modal mismatch in the perturbation sections of the waveguide geometry by only introducing perturbations in the slab sections. With this modification, the IL has been greatly reduced. The device maintains less than 0.5 dB loss over the wavelength range of 1500 nm to 1580 nm, covering the entire C-band.

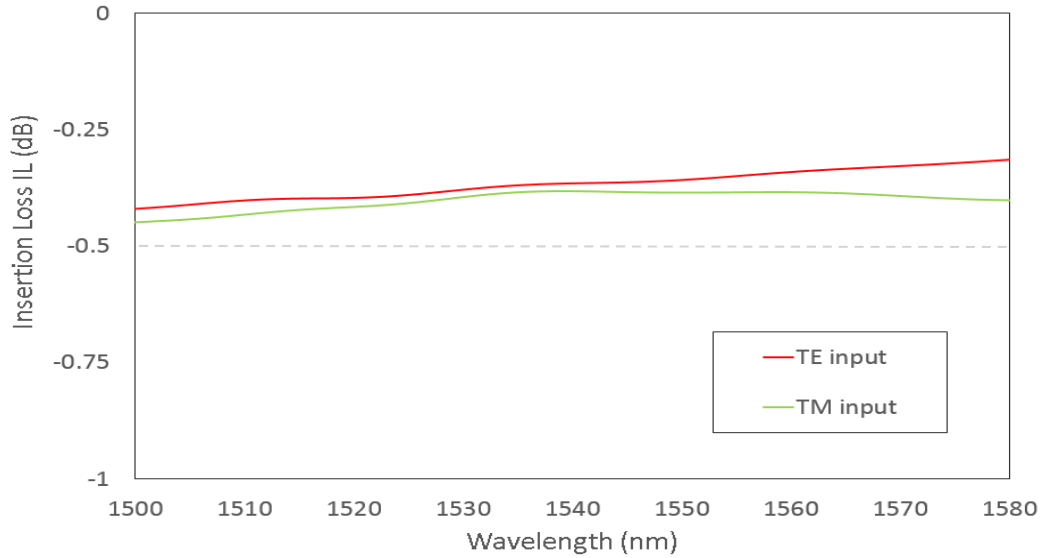


Fig.3. 9. Wavelength dependence of the insertion loss for TE and TM polarized inputs, calculated by 3D-FDTD.

3.3 Second Polarization Rotator Design

3.3.1 Device Structure

The structure of the second PR design based on asymmetrical period loaded SOI waveguides is illustrated in Fig.3.10. It is a channel waveguide with longitudinally periodic perturbations (loadings) along the waveguide, where the periodic perturbations on either side are mismatched. These perturbations are partial etches with a depth of 160 nm and tapered slab sections along the waveguide. The maximum width of the partial etch is W_s , while the width of the remaining waveguide core is W_c . Each section of the partial etches has a length of $2L_{HT}$, where L_{HT} is defined as the length of the half-tapered section. The proposed PR structure is formed by alternating the side perturbations for N times, where each period contains one partially etched section on each side of the waveguide. The device can be realized in a simple two-step etching process where one shallow etch is required to form the periodic loadings (the tapered slab sections) on either side of the waveguide, followed by one full etch to define the core.

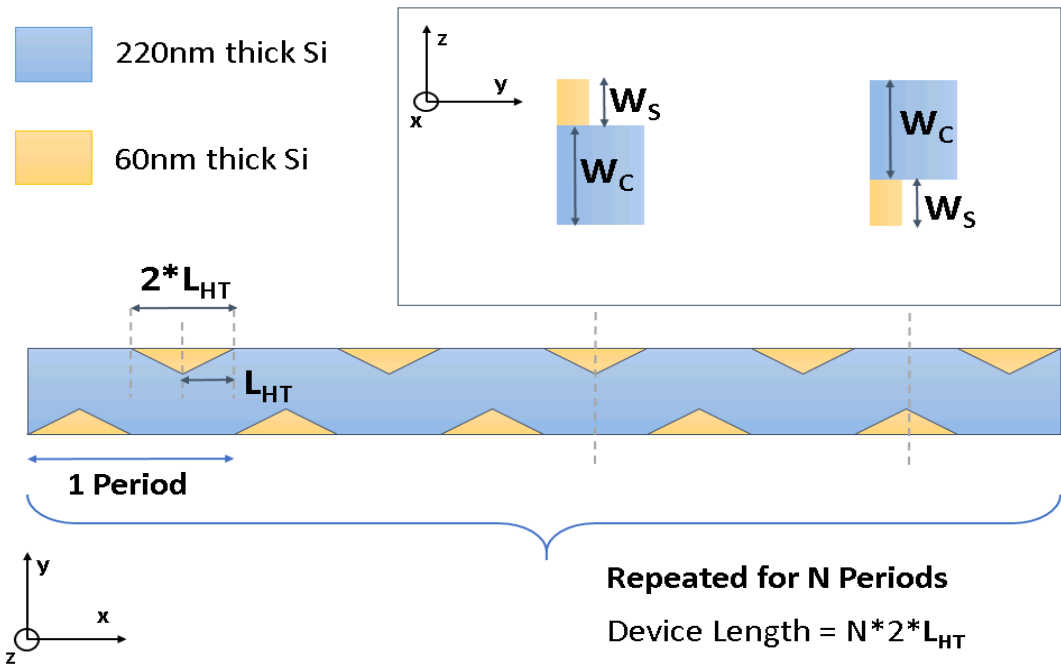


Fig.3. 10. Top and cross-sectionional views (inset diagram) of the proposed polarization rotator design.

3.3.2 Parameter Optimization

In our simulations, we focus on the C-band wavelengths for the quasi-TE and quasi-TM input modes. The refractive index of Si and the surrounding cladding are assumed to be $n_{Si}=3.476$ and $n_{SiO_2}=1.444$, respectively. Due to the limitations of the available foundry services (IMEC, for example), the thicknesses of the waveguide core and slab are chosen to be 220 nm and 60 nm, respectively.

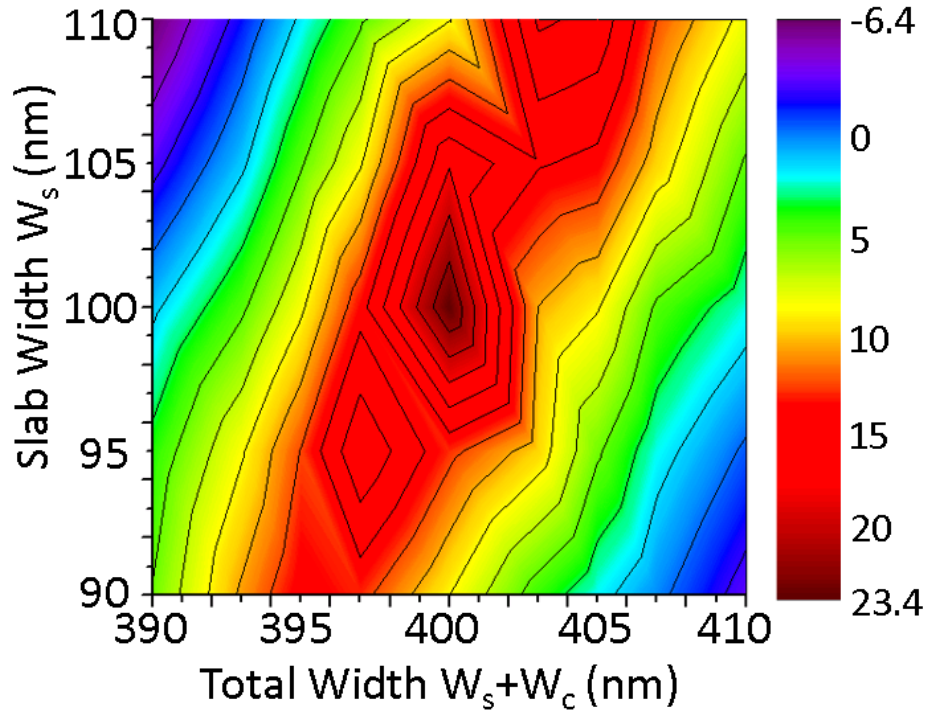


Fig.3. 11. EME calculation of ER as a function of total waveguide width ($W_c + W_s$) and slab width (W_s).

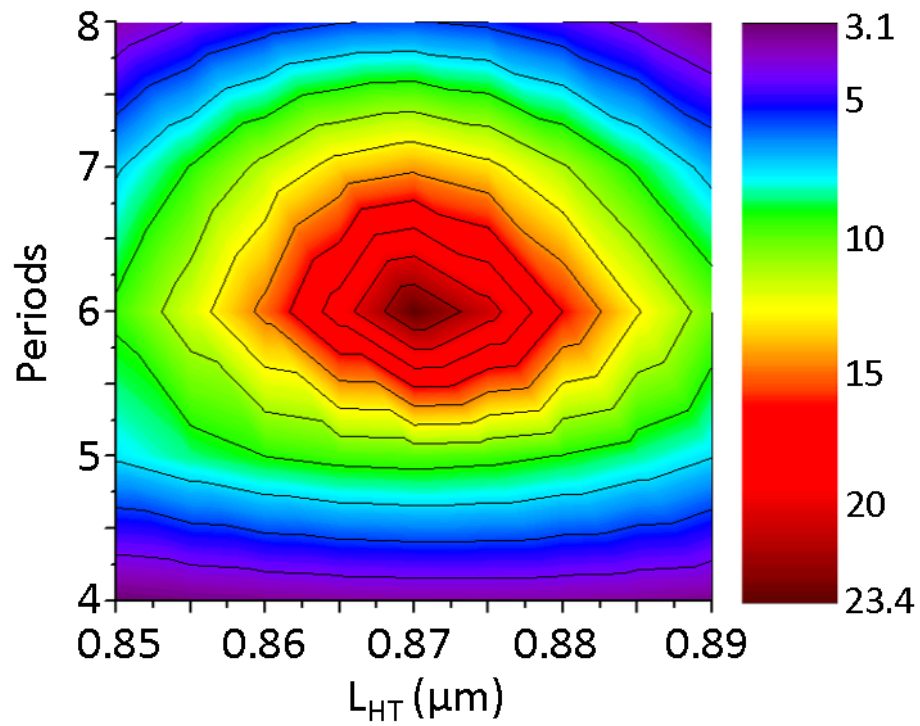


Fig.3. 12. EME calculation of ER as a function of the number of periods (N) and the half-taper length (L_{HT}).

For a given access waveguide height of 220 nm, and a slab height of 60 nm, the rotator performance will depend on the geometrical parameters W_c , W_s , L_{HT} , and the number of periods N . To determine the optimal core and slab width W_c and W_s , we first fix $L_{HT}=0.87 \mu\text{m}$ and the number of periods $N=6$. Fig. 3.11 shows the calculated ER as a function of total width ($W_c + W_s$) and slab width W_s . The best ER (23.4 dB) is found when total width= $0.4 \mu\text{m}$ and $W_s=0.1 \mu\text{m}$ ($W_c=0.3 \mu\text{m}$). The calculated ER is over 20 dB for a total width= $0.4 \mu\text{m} \pm 0.002 \mu\text{m}$ and $W_s=0.1 \mu\text{m} \pm 0.003 \mu\text{m}$.

Next we determine the optimal value of L_{HT} and N by fixing total width = $0.4 \mu\text{m}$ and $W_s = 0.1 \mu\text{m}$. Fig. 3.12 shows the ER as a function of N and L_{HT} , where the best ER (23.4 dB) is found when $L_{HT}=0.87 \mu\text{m}$ and $N=6$. The calculated ER is over 20 dB within the L_{HT} range of $0.864 \mu\text{m}$ to $0.877 \mu\text{m}$ for $N=6$.

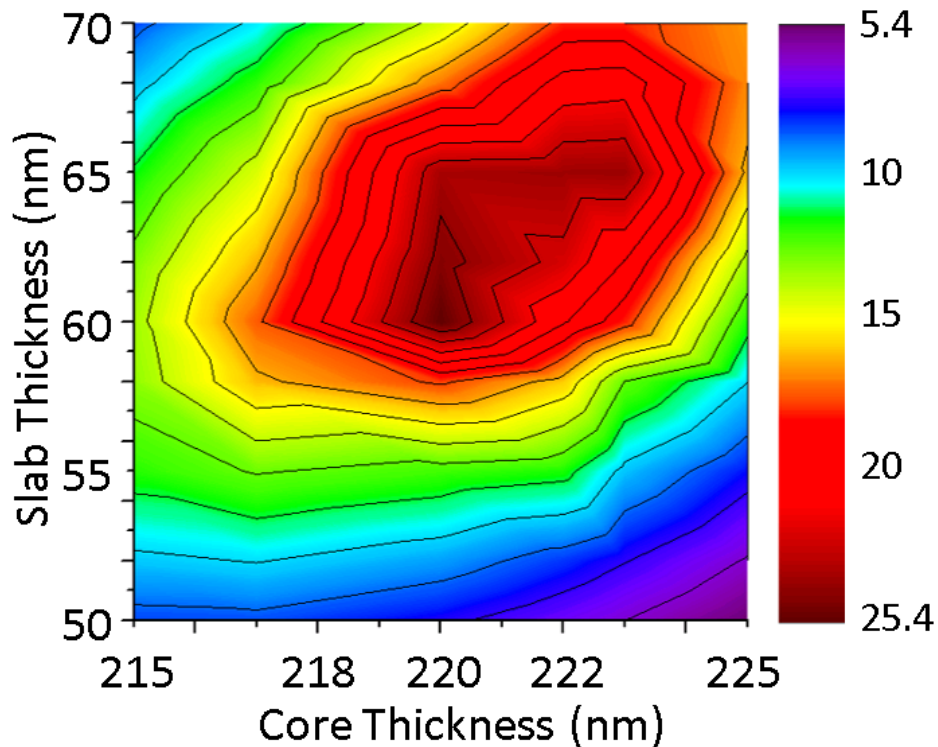


Fig.3. 13. EME calculations of ER as a function of slab and core thicknesses.

We then perform fabrication tolerance analysis on slab and core thickness. Fig. 3.13 presents the calculated ER as a function of these thicknesses, with W_c , W_s , L_s , and N being fixed. The calculated ER is over 20 dB for a core thickness of $220 \text{ nm} \pm 3 \text{ nm}$ and a slab thickness of $62 \text{ nm} \pm 4 \text{ nm}$. Because the operation of this device is based on breaking the symmetry at the waveguide cross section, the device's performance remains optimal for core-and-slab thickness combinations as large as $(223 \text{ nm}, 70 \text{ nm})$, since the rotation of the optical axis is still present. Note that the contour plots are not perfectly smooth. This is due to being based off of individual data points obtained from the EME calculations.

3.3.3 Performance Evaluation

The design optimization of the proposed PR structure is done by using the eigenmode expansion (EME) method, and is cross checked by the 3D-FDTD simulations. The refractive indices of Si and the surrounding cladding are assumed to be $n_{\text{Si}}=3.476$ and $n_{\text{SiO}_2}=1.444$, respectively. Based on the limitations of the available public foundry services, we selected the thicknesses of the waveguide core and the partially etched perturbed section to be 220 nm and 60 nm , respectively. As summarized in Table 3.2, the optimal values of the asymmetric waveguide sections are: $W_s=0.1 \mu\text{m}$, $W_c=0.3 \mu\text{m}$, $L_{\text{HT}}=0.87 \mu\text{m}$, and $L_{\text{total}}=20.88 \mu\text{m}$ ($N=6$). Based on the optimized parameters, we examine the operating wavelength range of our proposed rotator design by investigating ER and PRE with 3D-FDTD.

TABLE 3. 2. SUMMARY OF OPTIMIZED GEOMETRICAL PARAMETERS

Core Thickness (μm)	Slab Thickness (μm)	W_c (μm)	W_s (μm)	L_s (μm)	N	Device Length (μm)
0.22	0.06	0.3	0.1	0.87	6	20.88

Fig.3.14 shows ER as a function of wavelength for TE and TM inputs. The peak ER for the TE-TM conversion is 26.6 dB, at a wavelength of 1552 nm; while the peak ER for the TM-TE conversion is 32.5 dB, at 1544 nm. It is also observed that the simulated ER is >10 dB across the wavelength range of 1535 nm to 1567 nm, for the TE-TM conversion, and 1528 nm to 1558 nm for the TM-TE conversion.

The PRE of the optimized design is plotted as a function of wavelength in Fig. 3.15. For the TE-TM conversion, the calculated PRE is above 90% over the wavelength range of 1535 nm to 1568 nm; and a peak PRE of 99.79% is found at 1552 nm. For the TM-TE conversion, the calculated PRE is above 90% from 1527 nm to 1560 nm; and a peak PRE of 99.95% is found at 1544 nm. The difference in performance for the TE-TM and TM-TE conversions is because loss is polarization dependent, and the two modes evolve differently along the tapered sections.

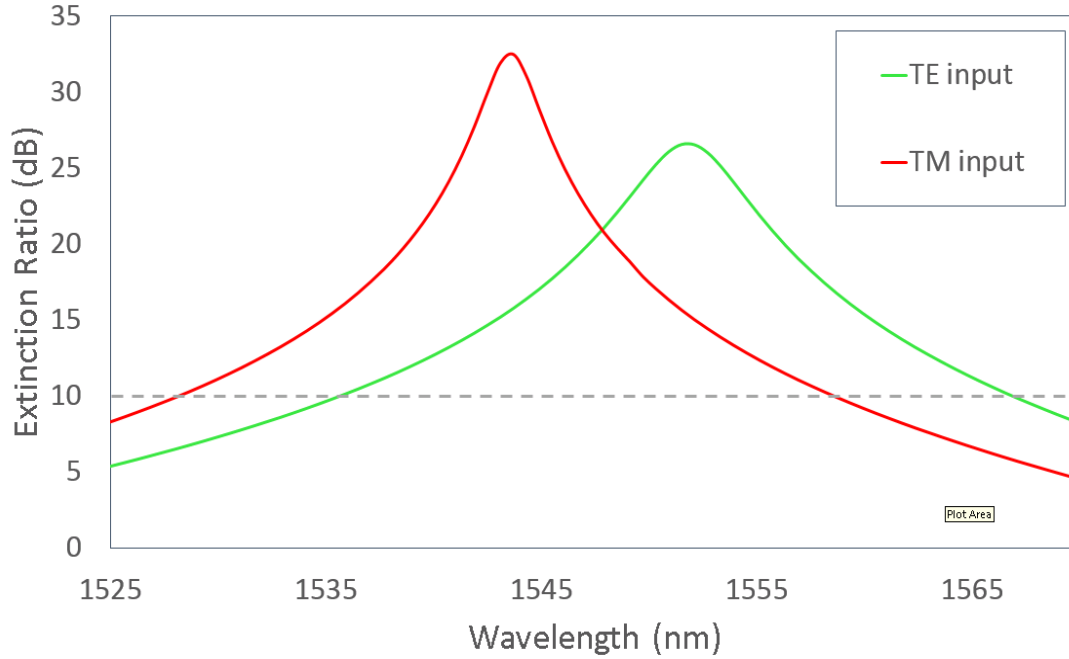


Fig.3. 14. Extinction ratio of the proposed polarization rotator design as a function of wavelength for TE and TM-polarized input modes. Calculations are made by 3D-FDTD.

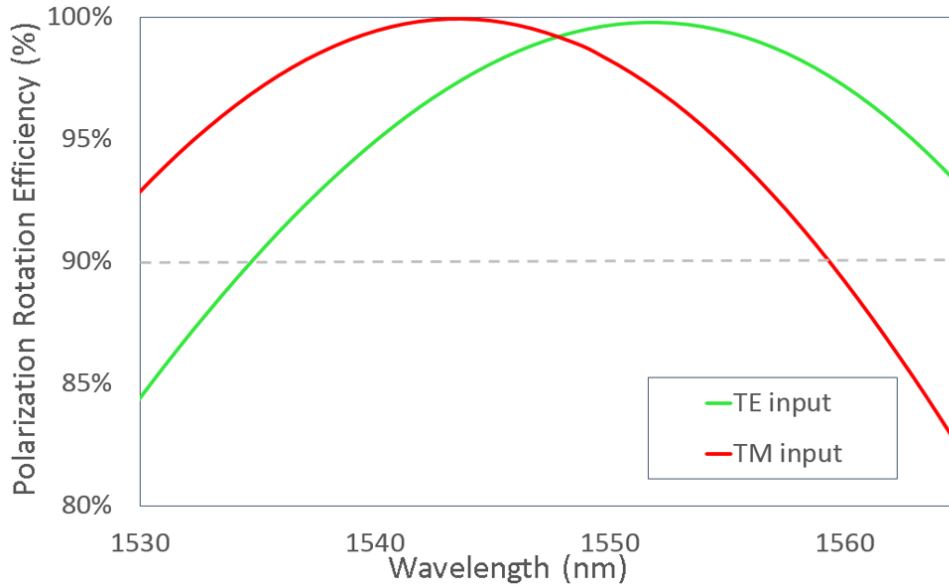


Fig.3. 15. Wavelength dependence of the polarization rotation efficiency for TE and TM-polarized inputs. Calculations are made by 3D-FDTD.

The IL of the optimized design is plotted as a function of wavelength in Fig. 3.16. The calculated IL is -2 dB over the wavelength range of 1530 nm to 1565 nm, for TE and TM inputs.

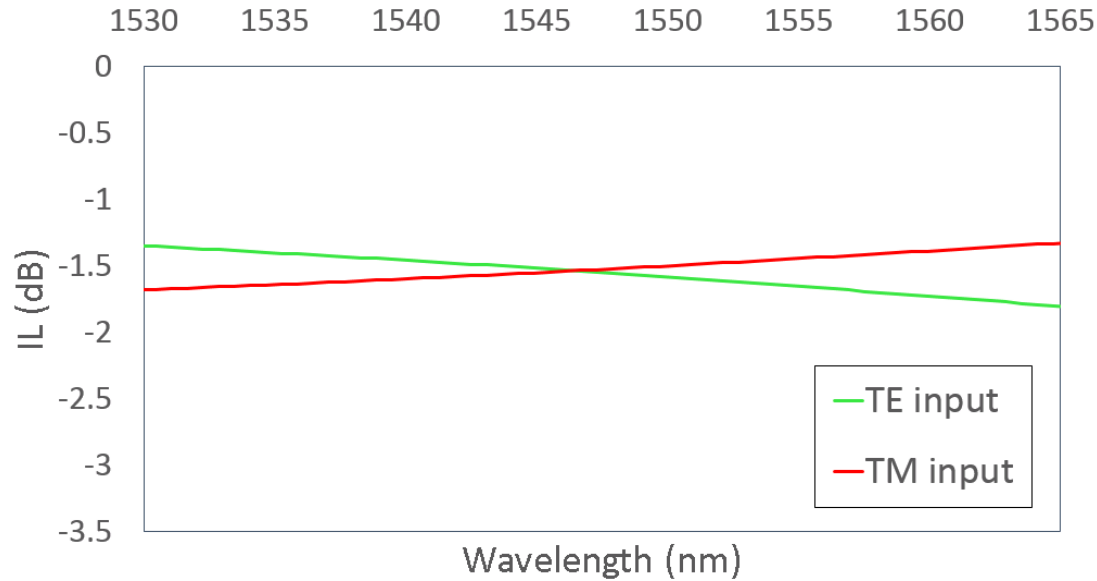


Fig. 3. 16. Wavelength dependence of the device's insertion loss (IL) for TE and TM-polarized inputs. Calculations are made by 3D-FDTD.

References

- [1] Y. Shani, R. Alferness, T. Koch, U. Koren, M. Oron, B. I. Miler and M. G. Young, "Polarization rotation in a symmetric periodic loaded rib waveguides", *Appl. Phys. Lett.*, Vol. 59, No. 11, Pp. 1278-1280, Sept. 1991.
- [2] J. J. G. M. Van Der Tol, F. Hakimzadeh, J. W. Pedersen, D. Li and H. Van Burg, "A new short and low-loss passive polarization converter on InP", *IEEE Photon. Technol. Lett.*, Vol. 7, No. 1, Pp. 32-34, Jan. 1995.
- [3] S. S. A. Obayya, B. M. A. Rahman, and H. A. El-Mikati, "Vector Beam Propagation Analysis of Polarization Conversion in Periodically Loaded Waveguides", *IEEE Photon. Technol. Lett.*, Vol. 12, No. 10, Pp. 1346-1348, Oct. 2000.
- [4] T. Mangeat, L. Escoubas, F. Flory and L. Roussel, "Integrated polarization rotator made of periodic asymmetric buried Ta₂O₅/silica sol-gel waveguides", *Opt. Express*, Vol. 15, No. 19, Pp. 12436-12442, Sept. 2007.

Chapter 4.

Fabrication and Testing Setup

This chapter covers the mask layout preparation and the fabrication and testing methods for the proposed devices. The mask layout was designed at Carleton University, using Mentor Graphics' IC-design tool—Pyxis Technology. The layout was generated with the AMPLE scripting language. The devices were fabricated using IMEC-ePIXfab Si Photonics technology, available through EURO PRACTICE, CMC, and the UBC SiEPIC program. The testing stage was setup in Carleton's Silicon Micro/Nano Photonics Laboratory. The testing-circuit design and the stage setup are also covered in this chapter.

4.1 IMEC Fabrication Technology Overview

The fabrication technology in IMEC's silicon photonics PSV technology features an SOI wafer with a 220-nm top Si film, a 2000-nm buried-oxide (BOX) layer. This technology is based on the 193-nm-deep ultraviolet lithography platform. It offers a range of passive building blocks, and is intended for communication-device prototyping and manufacturing.

There are 3 etch levels available through this technology, including a full etch of 220 nm (WG level), a shallow etch of 70 nm (FC level), and a deep etch of 160 nm (SK level). Fig. 4.1 illustrates the available etching levels. Three cladding options are also available: the top oxide, side oxide (with gaps filled), and air cladding. During the fabrication process, the WG-level structures are defined first, followed by the SK-level structures, and then the FC-level structures. Each etching is tracked by the remaining Si thickness, not the etch depth [1].

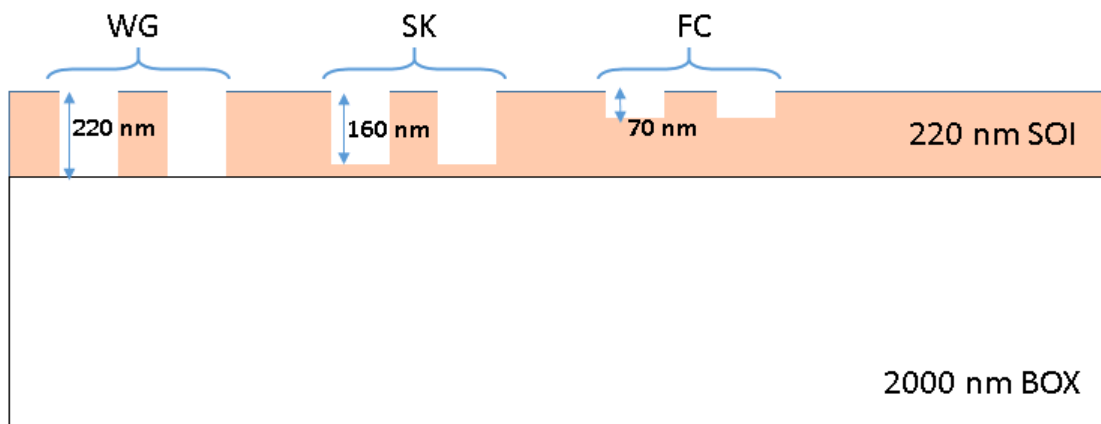


Fig.4. 1. The three available etch levels in IMEC’s Si Photonics PSV technology.

4.2 Mask Layers and Process Modules for the SOI Patterning

For each etch level, three mask layers are available for patterning waveguide and trench structures. The three mask layers include the core layers (COR), cladding layers (CLD), and trench layers (TRE). Each COR layer must be placed inside the CLD layer on the same etch level in order to form a waveguide structure. TRE layers can be placed by themselves; they are ideal for grating-like structures. Fig.4.2 below shows an example of patterning on the SK level. From the cross-sectional view, we see that a high-contrast rib waveguide structure is formed by combining the SK_COR and SK_CLD layers, and grating structures are formed by the SK_TRE layers [1].

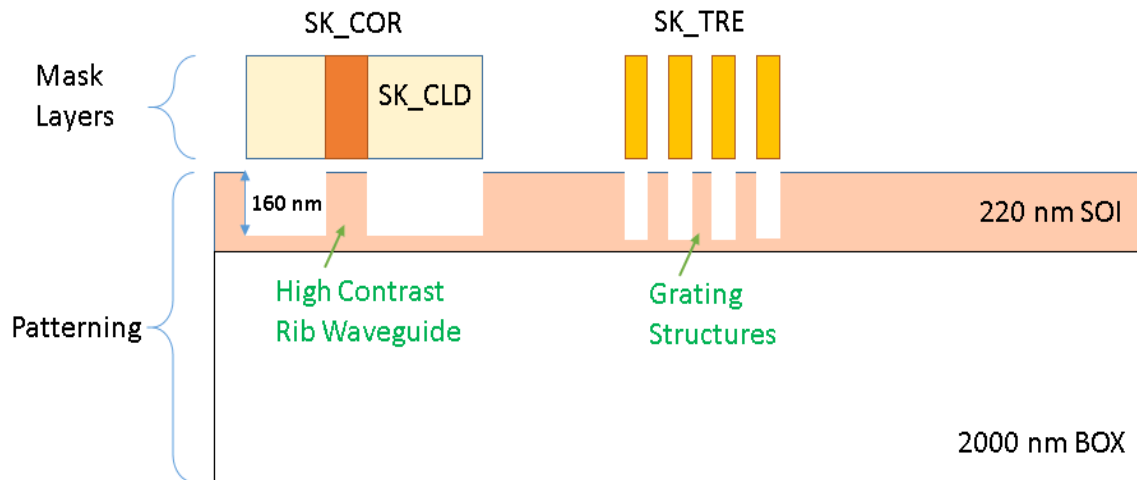


Fig.4. 2. Cross-sectional view of SOI patterning on the SK levels.

By combining mask layers on different etch levels, complex structures like that shown in Fig. 4.3 can be formed. First, the WG_COR and WG_CLD layers are used to define a strip waveguide with a width W_g . This is followed by a shallow etch with the FC_COR and FC_CLD layers—forming a ridge structure with a width W_c on the strip waveguide. The second step could be replaced by using two FC_TRE layers on each side, as shown in Fig. 4.3[1]. Note that depositing FC layers on top of the WG_CLD and WG_TRE layers will have no effect to the patterning, as the silicon will be fully etched [2].

In our proposed designs, the asymmetrical waveguide structures are formed by using WG_COR/WG_TRE and WG_CLD layers to define the entire waveguide, with SK_TRE layers being used to form the 60-nm-thick slab regions.

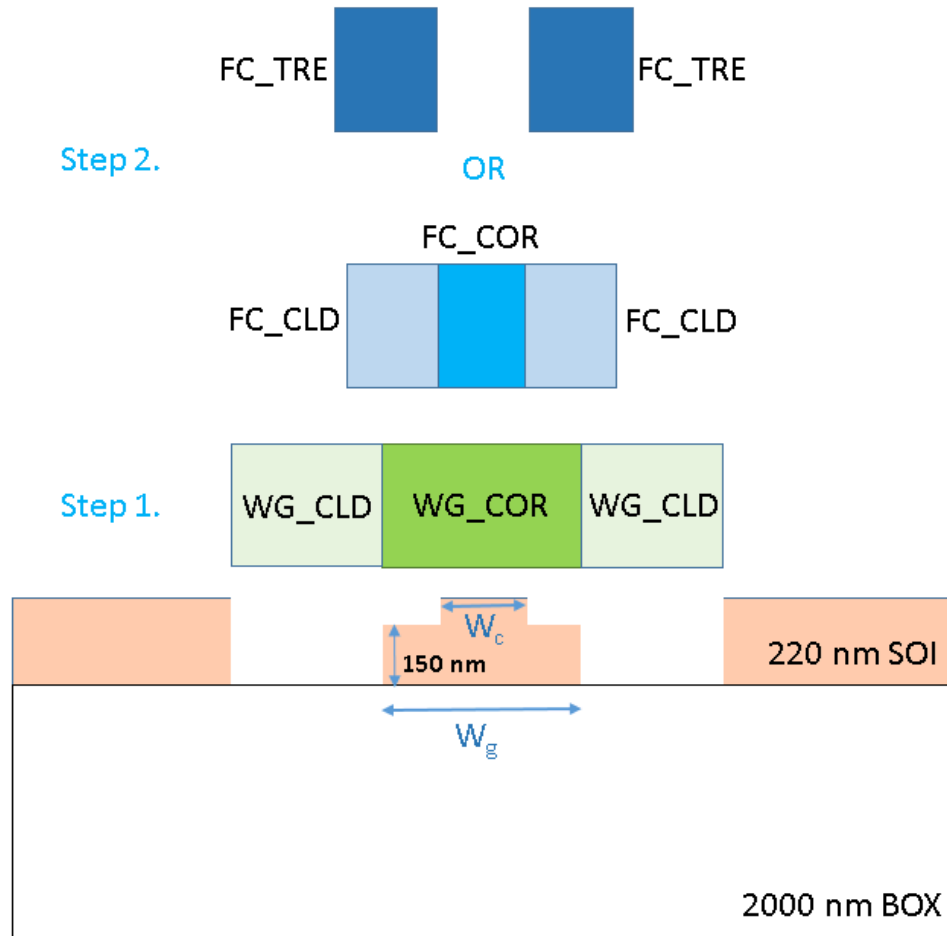


Fig.4. 3. Cross-sectional view of the SOI patterning process with mask layers on different etch levels.

4.3 Fabrication Tolerances and Bias

With this technology, the minimum achievable linewidth is 130 nm, and the minimum achievable spacing between features is 150 nm. However, larger values are more resistant to fabrication errors; with widths above 180 nm being recommended for better yields [1].

The thickness of the SOI wafer's silicon layer varies by ± 10 nm. The remaining slab thickness after the shallow etch (FC layers) varies by ± 15 nm, and by ± 10 nm after the deep etch (SK layers) [1].

The process targets a specific linewidth/spacing combination (450 nm/180 nm) for all etch levels [1]. All other dimensions are thus off target and biased. For the mask design purpose of the proposed devices in this thesis, only the linewidth is considered, as no line pairs are used. Fig. 4.4 plots the bias features for all etch levels. This provides a comparison of the linewidth of the mask with that of the wafer. The data is obtained from [2], where the overall measurement error is ± 10 nm. The dashed lines present the fitted trend lines.

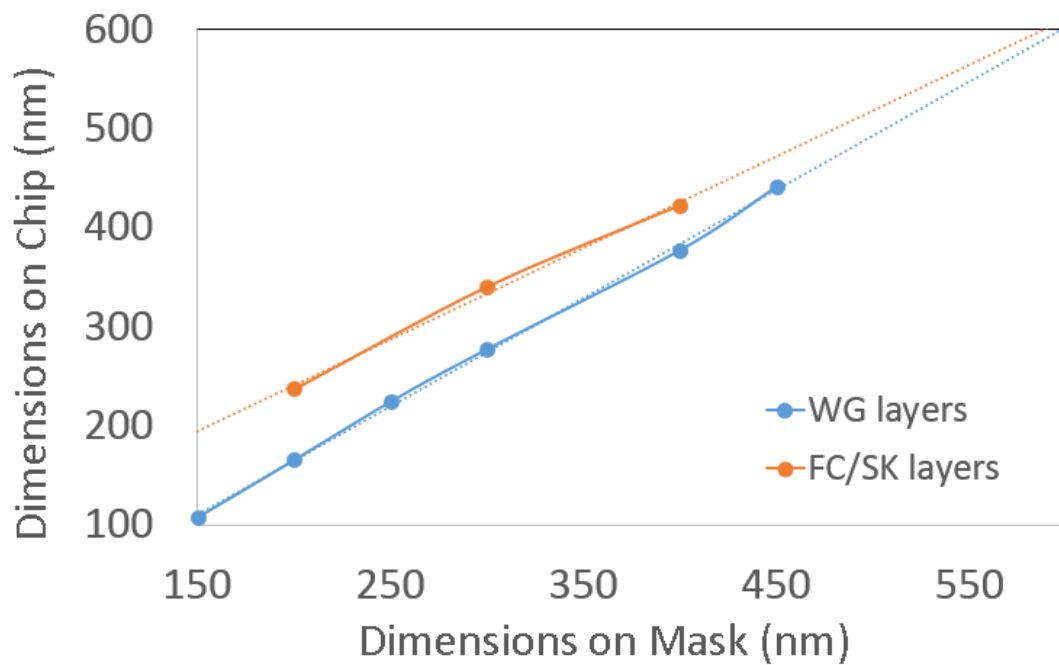


Fig.4. 4. Comparison of the dimensions of the mask with that of the wafer, based on the data provided in [2].

4.4 Mask Layout Design

The mask layout was designed at Carleton University, using Mentor Graphics' IC-design tool—Pyxis Technology. The layout was generated using AMPLE. The AMPLE scripts written to generate the mask layouts for both designs are given in Appendix A. In order to achieve the desired dimensions on chip, dimensions for all the segments used in the mask layout were chosen by taking consideration of the fabrication bias described in Section 4.2.

The mask layout designs for the proposed devices are shown in Fig. 4.5. In this figure, shapes in red represent the WG_TRE layers, shapes in green represent the SK_TRE layers, and the blue areas represent the WG_COR layers.

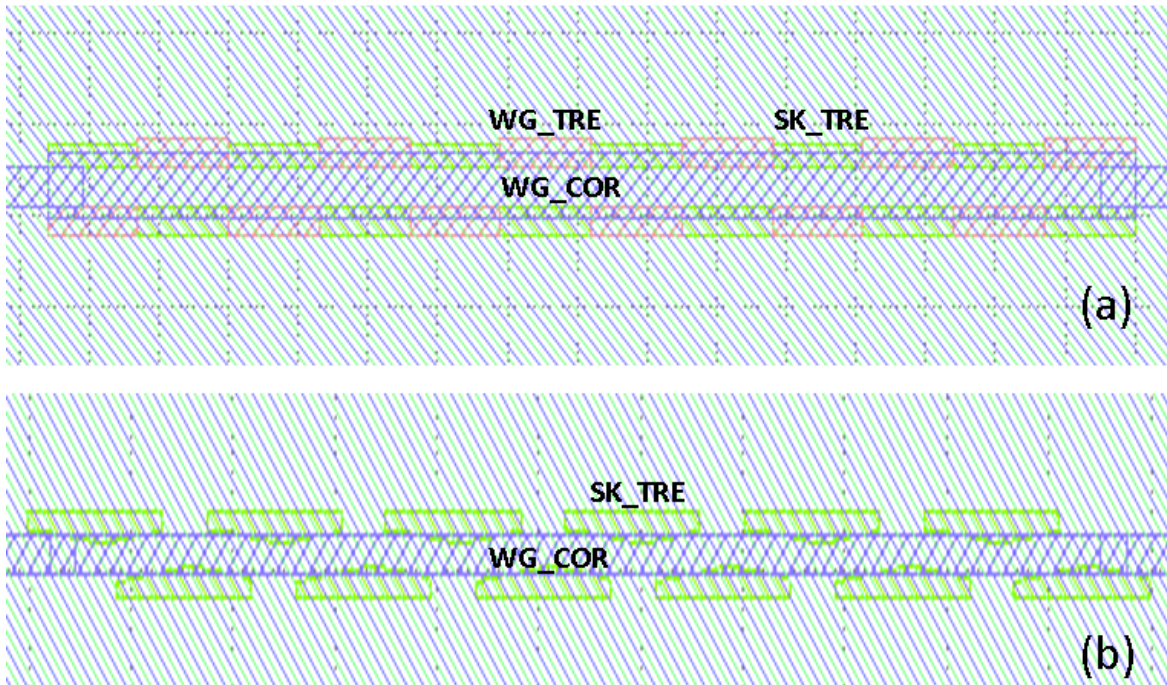


Fig.4. 5. Mask layout designs for the two proposed devices.

The device shown in Fig.4.5 (a) is formed by first defining a wide waveguide ($W=W_c+2W_s$) with square cutouts along each side, via WG layers. This is followed by a deep etching of 160

nm on the sides to create the 60-nm-thick slab region. The device shown in Fig. 4.5 (b) is formed by first defining the waveguide region, and then by creating the tapered perturbed regions by introducing triangular shaped SK_TRE layers.

4.5 Testing Circuit Mask Design

The 2 mm × 2 mm chip space provided by the foundry included the mask layout for both designs' testing and reference circuits. In our mask design, we varied the geometric parameters of our rotator design in order to compensate for fabrication errors. In order to compensate for the wafer thickness variation, three different sets of devices with different perturbed section lengths (L_s or L_{HT}) were used for each design. Different sets of waveguide core and slab widths were also included to compensate for fabrication errors. For devices with optimized perturbed section lengths, two groups of three identical devices are fabricated for each specific set of waveguide core and slab widths. For devices with perturbed section lengths compensating for wafer thickness variations, only one group of three identical devices are fabricated. Due to spatial limitations, no variations are included to compensate for slab thickness variations and misalignment errors.

Fig. 4.6 shows the mask layout of the testing circuit for one group of devices. Three TE-mode and three TM-mode grating couplers were used to couple the light beams into and out of our devices. The grating couplers were designed in UBC [3] and supplied with the design rule deck by IMEC. In order to measure the performance of the devices, the grating couplers in each testing circuit set were paired as TE-TE, TM-TM, and TE-TM, as shown in the figure. The waveguide bending radius is 10 μm for the TE-TE circuit, and 20 μm for the TM-TM and TE-TM circuits (in order to avoid the large bending losses of TM modes). The space between

each pair of grating couplers is chosen based on the dimensions of the fiber array (FA) used for testing. Reference waveguide circuits are built without PR structures, but with grating couplers and waveguide bends of the same radius.

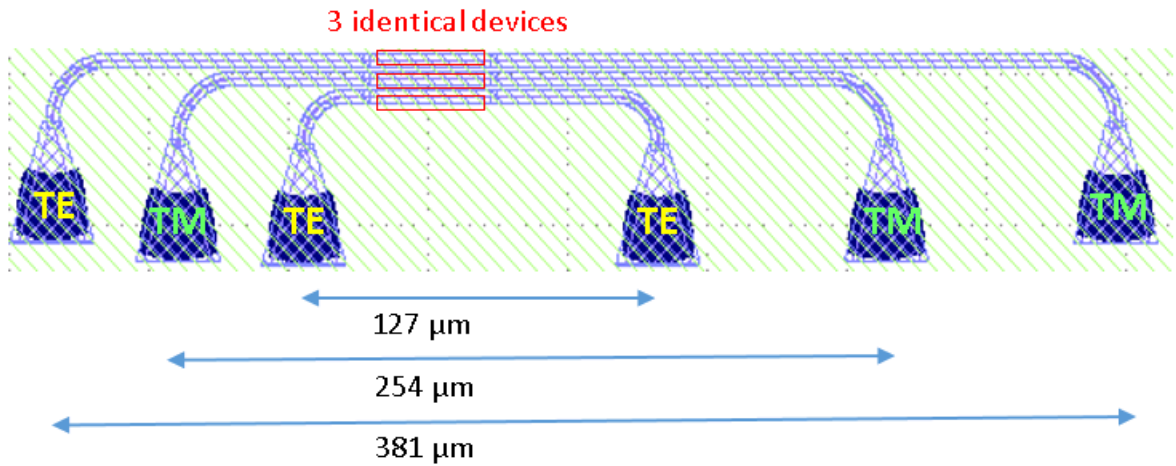


Fig.4. 6. Mask of the testing circuits for one group of devices.

The complete mask design includes mask layouts for the two PR designs and the reference waveguide circuits, as shown in Fig. 4.7. This layout was then merged into a larger map with other users' layout designs by CMC.

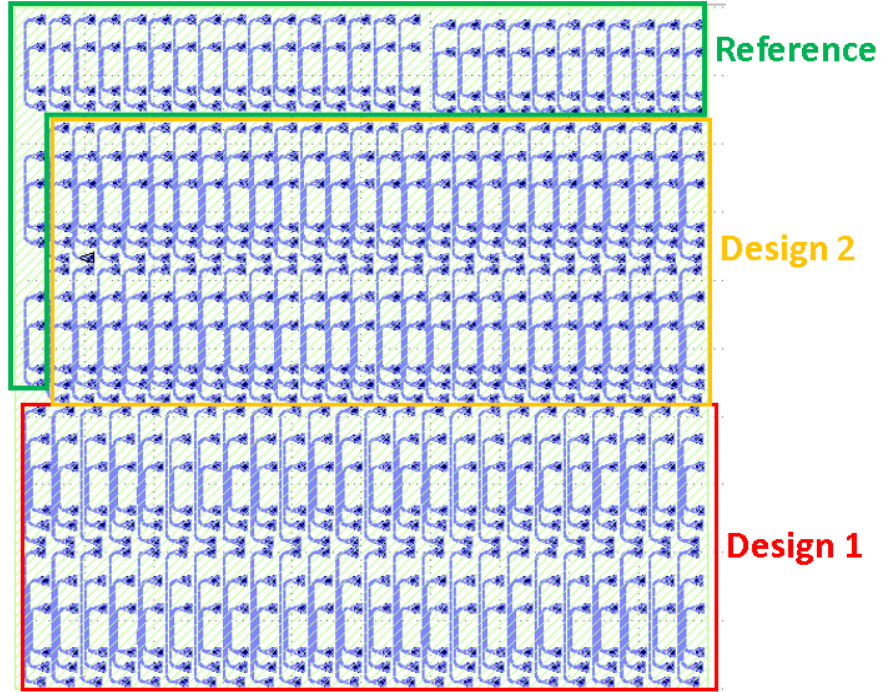


Fig.4. 7. The completed mask layout for the proposed designs.

4.6 Testing Setup

The testing setup was built using a 6-channel polarization-maintaining (PM) fiber array (FA) on an automated testing stage. The FA was customized for our testing setup by PLC Connections. It has three TE launch PANDA fibers and three TM launch PANDA fibers (Nufern PM1550-XP), and was used for light injection and collection to and from the devices. The use of an FA halves the effort needed for precise alignment compared to the edge-coupling method, as the alignment only has to be performed once per device, rather than for both the inputs and outputs. The fiber core pitch is $127\ \mu\text{m}$, which determines the space between the GCs used in the testing circuit.

The testing stage consisted of an angle rotator (Optosigma ksp-606M rotational stage) and a stage with x, y, and z control (3 ThorLab BA1 post base + Newport mb 3 plate + Thorlabs Max 341/M nanomax stage with apt stepper controller). The chip is placed on top of the testing stage

when testing, and the FA was mounted to a separate stage with an FA holder and a manual goniometer (Newport corporation 150 magnetic instrument base +3 Thorlabs pt1 1" translation stages + Thorlabs Ap20 right angle plate + Optosigma goh-60a50 goniometer). The FA holder (Custom fiber array holder bracket) is a slotted aluminum channel that can hold the FA ribbon via side screws. To achieve maximum coupling, the FA was held to a 10.8° angle from the vertical axis. This satisfies the 20° coupling requirement for the GCs [3]. An optical microscope (Zeiss Stemi 2000C) and a fiber light source (Titan tool supply co Inc FO150 light with fiber optic light guide) were used for precise alignment of the FA to the GCs of the devices. An optical vector analyzer (Luna Optical Vector AnalyzerTM 5000) was used to perform the wavelength scans of the device. It has a tunable laser covering a wavelength range of 1525 nm to 1610 nm. The polarization of the input light source was calibrated by using external polarization-control paddles (provided by the optical vector analyzer kit). Fig. 4.8 illustrates the block diagram of the entire testing setup.

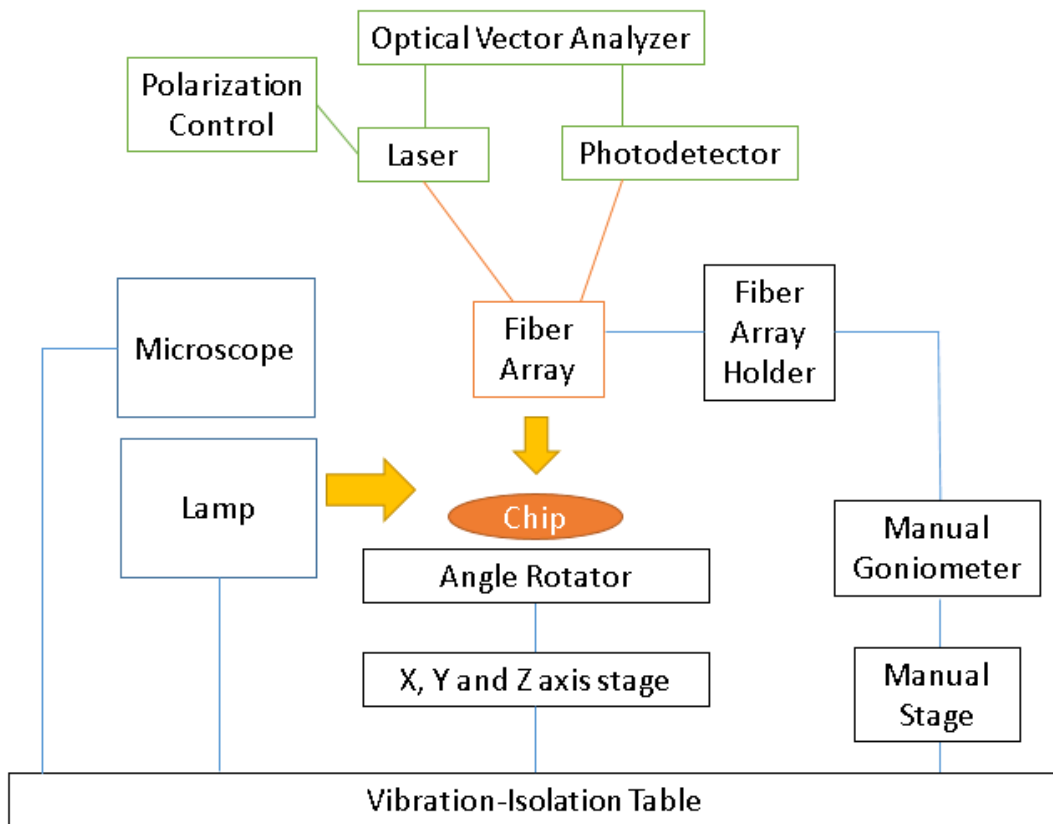


Fig.4. 8. Block diagram of the testing setup.

References

- [1] Silicon Photonics PSV Technology Handbook, IMEC, Ghent University
- [2] Silicon Photonics PSV Layout Handbook, IMEC, Ghent University
- [3] Y. Wang, J. Flueckiger, C. Lin, and L. Chrostowski, “Universal Grating Coupler Design,” in Photonics North, 2013.

Chapter 5

Experimental Results and Discussion

This chapter includes the experimental results for both PR designs; which are compared to the simulated results. The reasons for performance degradation of the fabricated devices are analyzed, and the SEM images for both fabricated PR designs are included.

5.1 SEM Images of the Fabricated Devices

SEM images of the fabricated devices were taken at Carleton University (Fig. 5.2) and the University of Ottawa (Fig. 5.1). The SEM image of the first PR design (with 60-nm-thick rectangular shaped slabs) is shown in Fig. 5.1 (a), and the SEM image of the second PR design (with 60-nm-thick triangular shaped perturbed sections) is shown in Fig. 5.1 (b). The inset of Fig.5.1 (b) shows the detailed look of one triangular shaped perturbed section. The long dark area

underneath the perturbed section is the mark left by etching, as SiO_2 is not completely resistant to etching. The SEM images were taken using an air cladding chip, the effect of SiO_2 being etched is negligible in the fabricated devices since the devices has top cladding of SiO_2 .

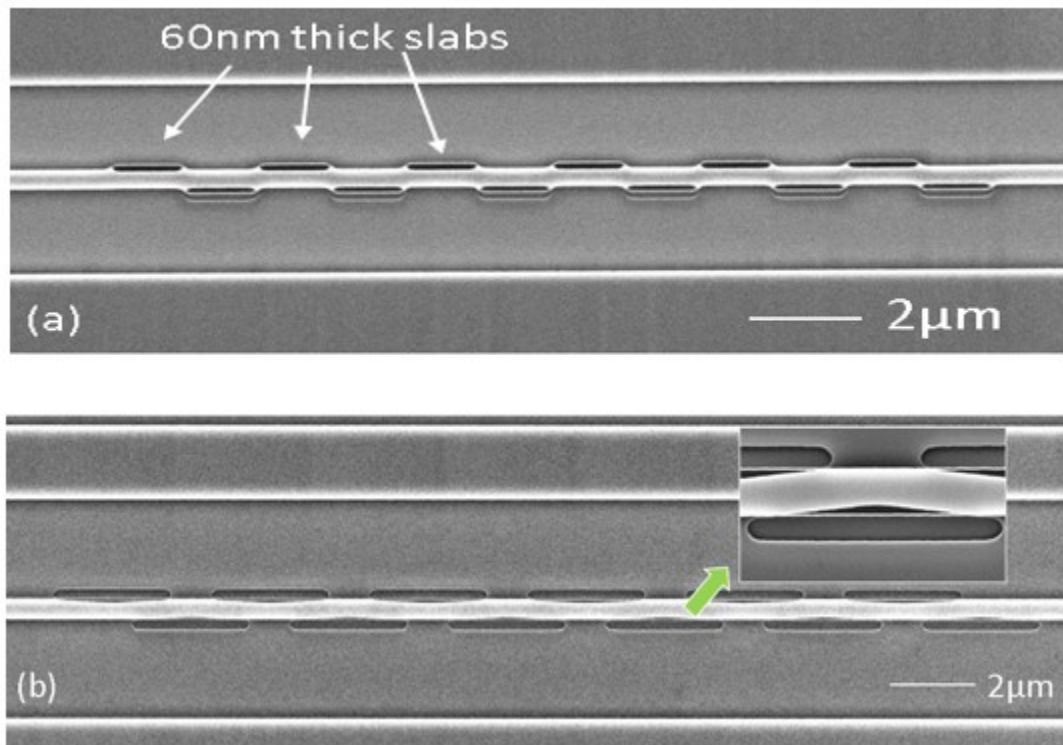


Fig.5. 1. SEM images showing (a) the top view of the first fabricated design, and (b) the top view of the second fabricated design.

Fig.5.2 shows the SEM image of one set of testing circuits, in which the grating couplers (GCs) are shown, along with the fabricated devices and their dimensions. In the testing circuit, three identical devices were fabricated and connected to a pair of TE GCs, a pair of TM GCs, and a pair consisting of one TE GC and one TM GC.

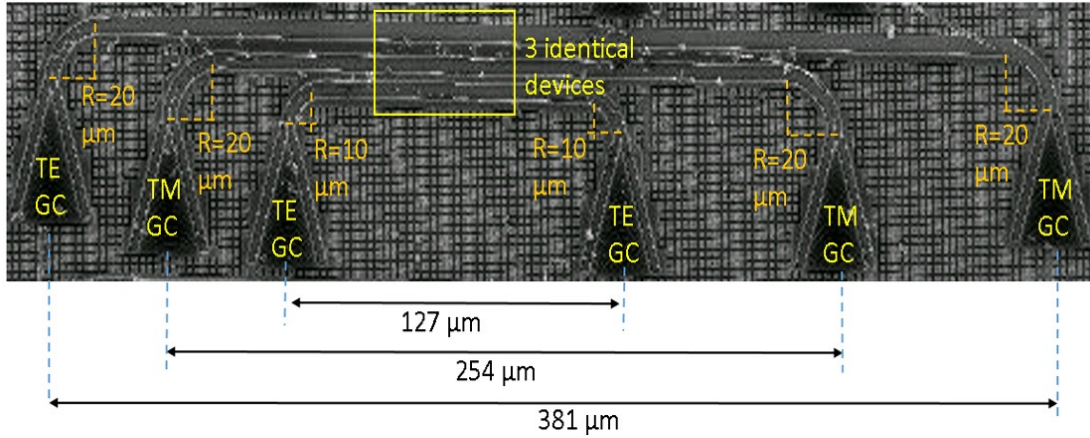


Fig.5. 2. Top view of the testing circuit for the fabricated design.

5.2 Performance Characterization for the First Design

Using the testing setup illustrated in Chapter 4, we characterized the performance of the fabricated devices. The measured transmissions were first normalized with respect to the reference circuits. The insertion loss of the TE-TE and TM-TM couplers (without the PR structures) includes the coupling loss of the GCs and the waveguide bends. The normalization for the TE-TE and TM-TM transmission was done by subtracting the TE-TE reference waveguide circuit transmission (TE-TE ref) and the TM-TM reference waveguide circuit transmission (TM-TM ref), respectively. The normalization for TE-TM/TM-TE transmission follows the relationship $TE-TM/TM-TE_{normalized} = TE-TM/TM-TE_{measured} - 0.5(TE-TE_{ref} + TM-TM_{ref})$. This would be a close approximation for the real normalized transmission. Fig. 5.3 shows the normalized measurements of the TE-TE, TE-TM, TM-TE, and TM-TM transmissions.

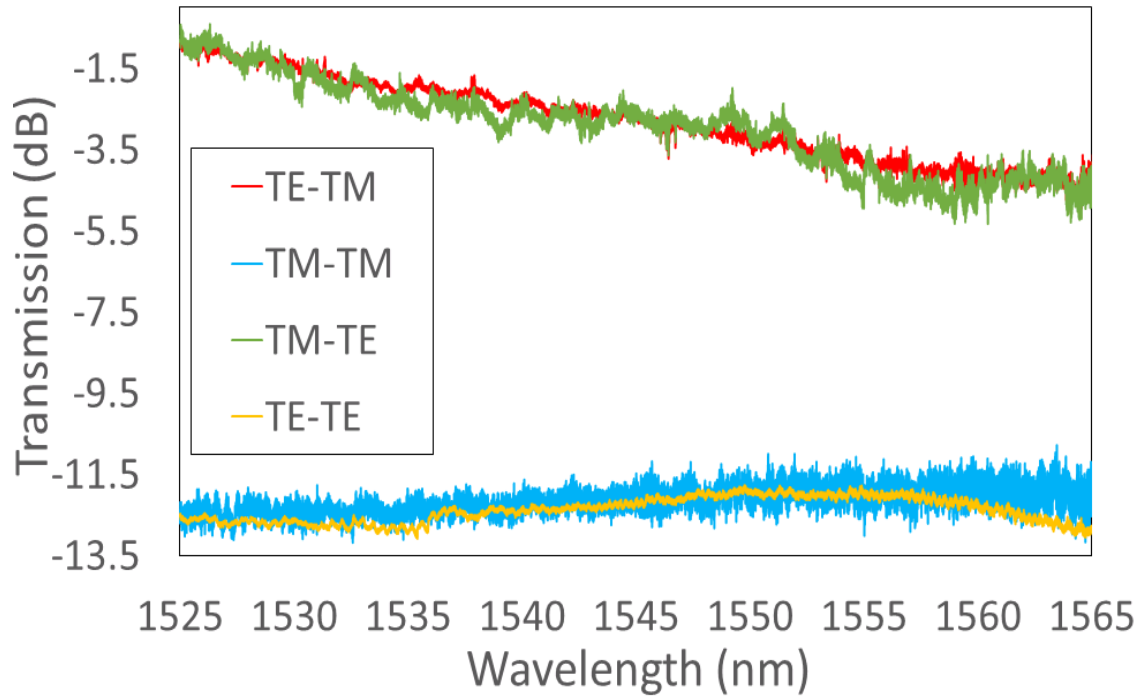


Fig.5. 3. Normalized measurements of transmission as a function of wavelength, for the fabricated device.

The ER for the TE-TM/TM-TE conversion can be obtained by subtracting the normalized TE-TE/TM-TM transmissions from the TE-TM/TM-TE transmissions, respectively. Fig. 5.4 shows the ER calculated for both polarization conversions as a function of wavelength. For both TE-TM/TM-TE conversions, the ER is over 8 dB for a wavelengths range of 1525 nm to 1553nm, and is over 6 dB over the entire C-band. The peak ER is 11.8 dB, at wavelength of ~1525 nm.

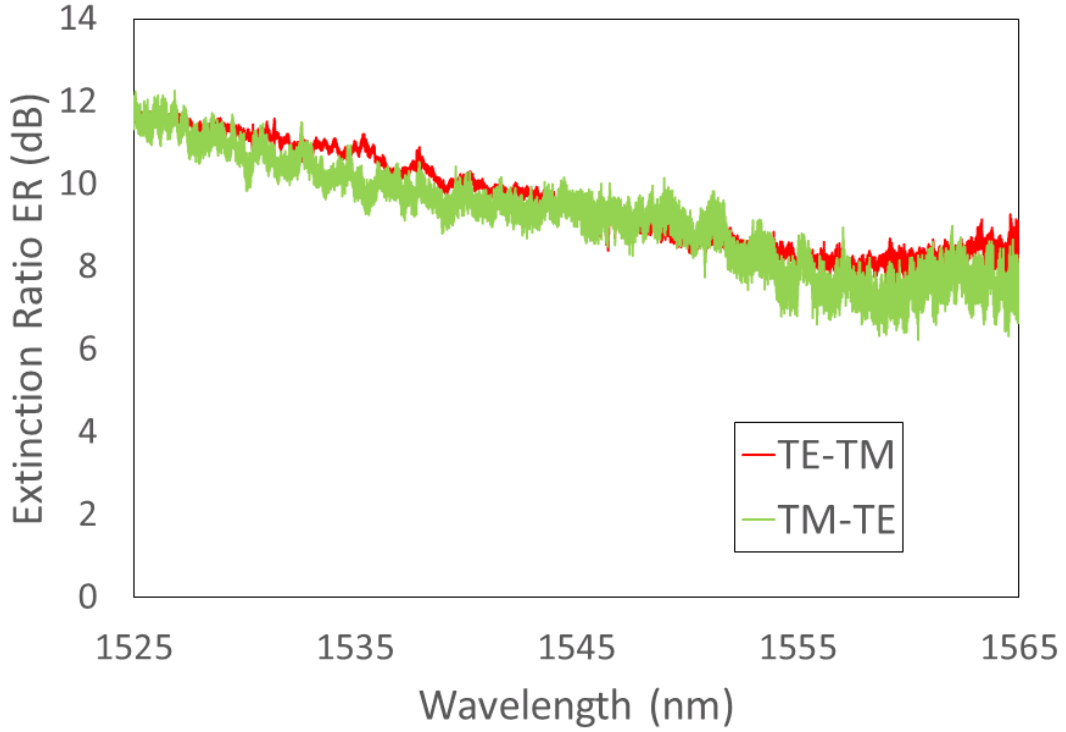


Fig.5. 4. Extinction ratio of the fabricated device (with rectangular shaped perturbed sections) as a function of wavelength.

Since the transmission measured by the optical vector analyzer presents the power ratio of output power over input power, in decibels, the P_{out}/P_{in} for the fabricated devices can be obtained following

$$P_{out}/P_{in} (\text{TE-TM or TM-TE conversion}) = 10^{(0.1 * \text{TE-TM}_{normalized} \text{ or } \text{TM-TE}_{normalized})} \quad (5.1)$$

$$P_{out}/P_{in} (\text{TE-TE or TM-TM}) = 10^{(0.1 * \text{TE-TE}_{normalized} \text{ or } \text{TM-TM}_{normalized})} \quad (5.2)$$

Thus, we can calculate the PRE by

$$\text{PRE}_{\text{TE-TM/TM-TE}} = (P_{out}/P_{in} \text{ TE-TM/TM-TE}) / [(P_{out}/P_{in} \text{ TE-TM/TM-TE}) + (P_{out}/P_{in} \text{ TE-TE/TM-TM})] \quad (5.3)$$

The PRE of the fabricated devices, for both the TE-TM conversion and the TM-TE conversion, is plotted in Fig. 5.5. At a wavelength of approximately 1525 nm, the highest PRE obtained for

the TE-TM conversion is 93.5%, and 93.9% for the TM-TE conversion. For both conversions, the PRE stays above 80% for the wavelength range of 1525 nm to 1565 nm.

The insertion loss of the PR itself is measured to be -1.2 dB at the peak wavelength (1525 nm). Simulations show less than 0.5 dB of loss for the device. The excess loss observed is mainly due to reflection and scattering losses. The slightly different performance in the TE-TM and TM-TE conversions is mainly due to the polarization dependency of these losses. In addition, the exact optimized dimensions are difficult to realize in fabrication.

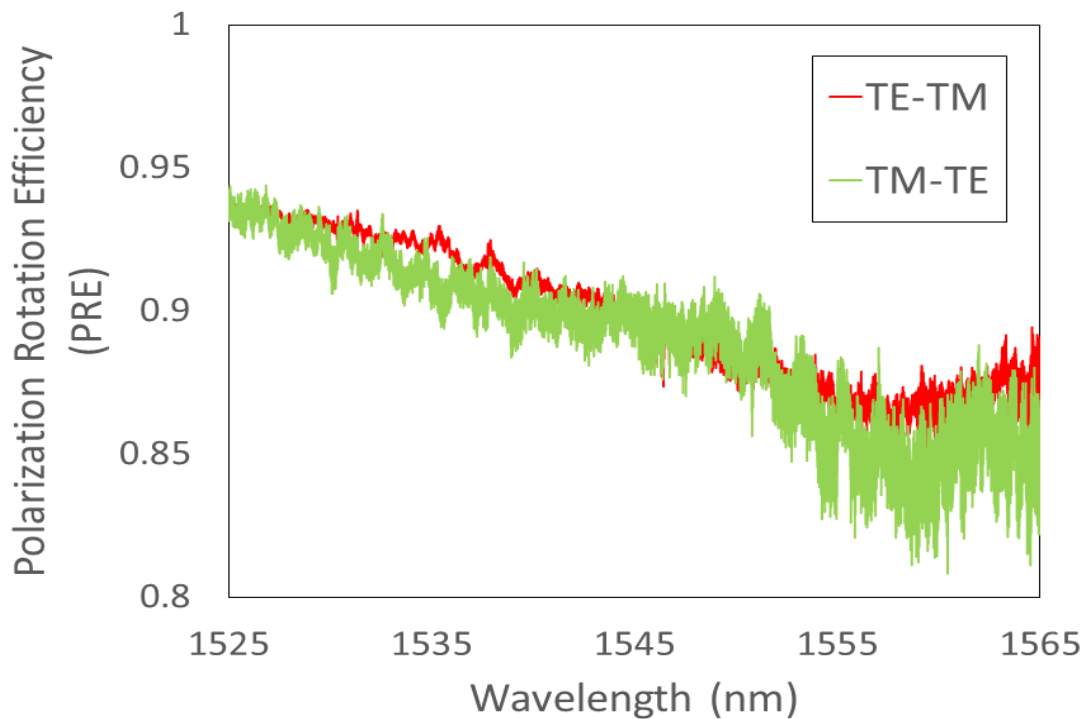


Fig.5. 5. PRE of the fabricated devices (the first design) as a function of wavelength.

In the simulations, we have predicted that the peak ER is at ~1550 nm wavelength, for both the TE-TM and TM-TE conversions. The calculated peak ER is 25.45 dB and 25.01 dB for TE-to-TM and TM-to-TE conversions, respectively. The ER is greater than 10 dB over the entire C-band. Experimentally, the ER is over 8 dB for a wavelengths range of 1525 nm to 1553 nm, and is greater

then 6 dB over the entire C-band, for both conversions. The peak ER is 11.8 dB at a wavelength of ~1525 nm.

The calculated PRE is centered at ~1550 nm, for both the TE and TM inputs. The peak PRE for the TE-TM conversion is 99.72%, and 99.68% for the TM-TE conversion. The calculated PRE is greater than 90% over the C-band. Experimentally, the PRE is greater than 80% over the C-band, and the peak PRE is found to be ~93.5% at a wavelength of 1525 nm.

The experimental results show a significantly lower performance than the simulated results. As we have shown in Chapter 3, the design is fabrication sensitive. The deviations in the optimized geometric parameters are the main reasons for the optimal peak wavelength shift and degradation of the ER in our fabricated devices. A more detailed study is presented in Section 5.4.

5.3 Performance Characterization for the Second Design

The fabricated devices based on the second PR design (with triangular shaped perturbation sections) were tested using the same testing setup and procedure. Fig. 5.6 shows the normalized measured transmission spectra for TE-TE, TE-TM, TM-TE, and TM-TM, over the operating wavelengths. The large noises observed at the longer wavelengths are due to peak wavelength shifts in the GCs used for measurement.

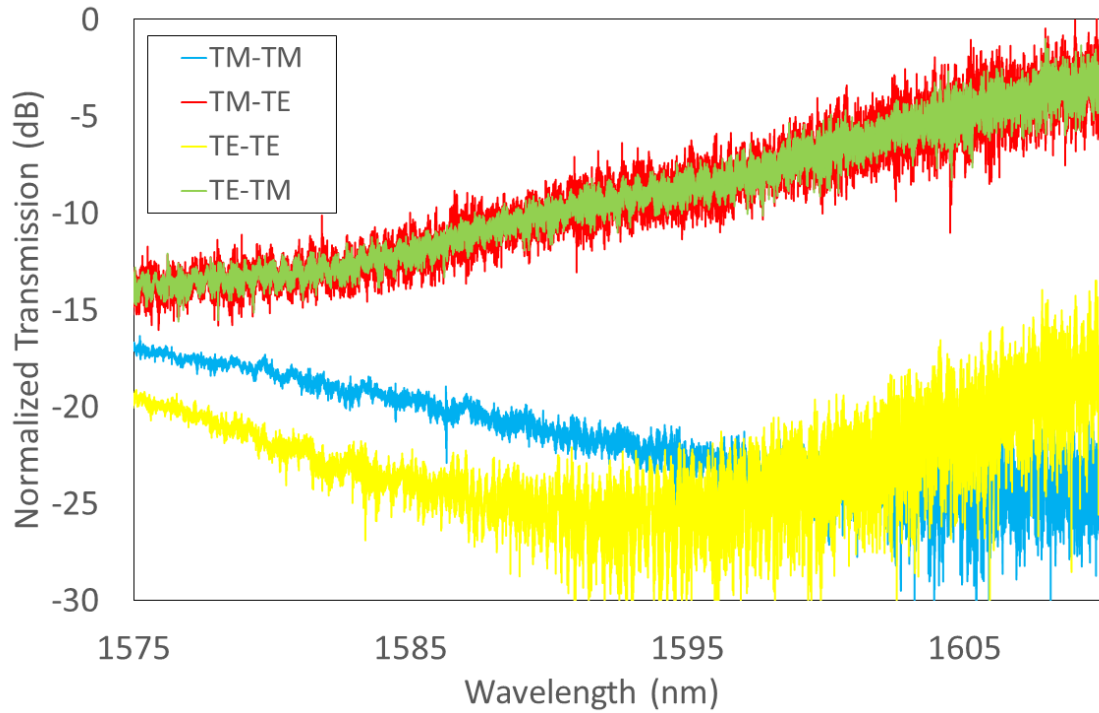


Fig.5. 6. Normalized measured transmission as a function of wavelength for the fabricated device.

Fig. 5.7 shows the ER calculated for both polarization conversions, over the operating wavelengths. The peak ER is found to be ~ 16 dB, at a wavelength of ~ 1593 nm, for the TE-TM conversion; and ~ 20 dB, at ~ 1605 nm, for the TM-TE conversion. The ER is over 10 dB for the wavelength range of 1570 nm to 1610 nm, for the TE-TM conversion; and is over 10 dB between 1585 nm and 1610 nm, for the TM-TE conversion. The noise observed at longer wavelengths is caused by peak wavelength shifts in the GCs used for measurement.

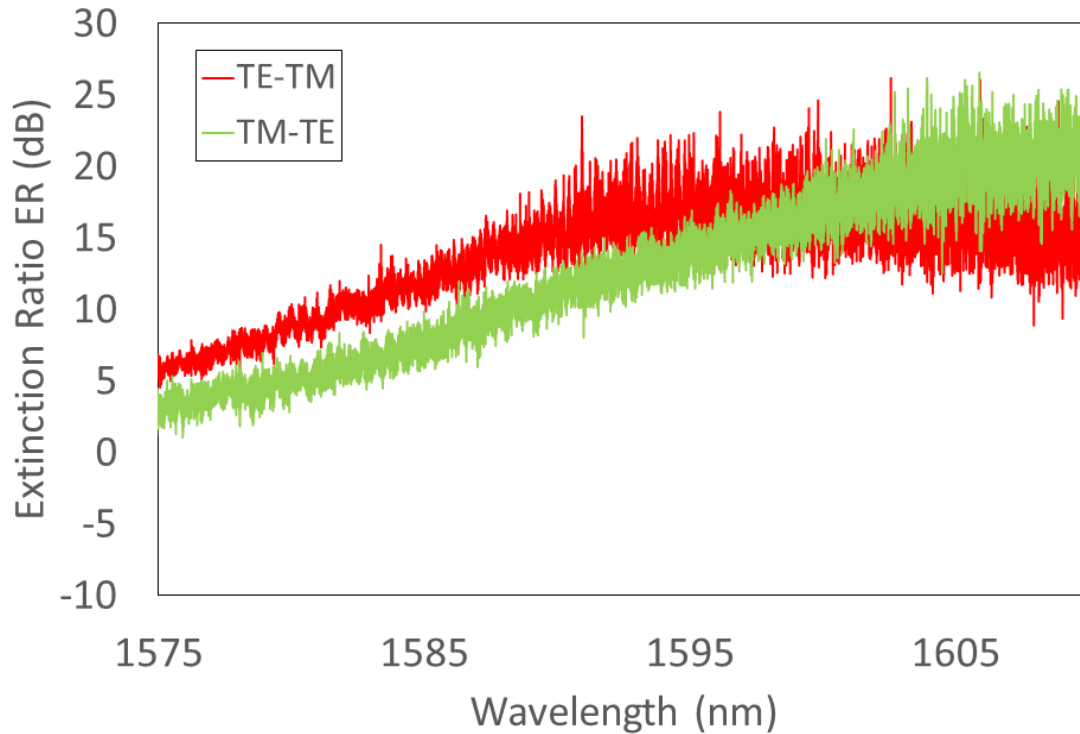


Fig.5. 7. Extinction ratio of the fabricated device (with triangular shaped perturbed sections) as a function of wavelength.

Based on the same calculation steps described in Section 5.3, the PRE values for both conversions were obtained, and plotted in Fig. 5.8. For the TE-TM conversion, the PRE is over 90% from 1578 nm to 1610 nm. For the TM-TE conversion, the PRE is over 90% from 1585 nm to 1610 nm. The peak PRE is found to be $\sim 97.5\%$, at ~ 1595 nm, for the TE-TM conversion; and $\sim 98.75\%$, at ~ 1607 nm, for the TM-TE conversion.

The insertion loss of the PR itself is measured to be ~ -2.5 dB at the peak transmission, for both polarization conversions. Simulations show less than -2 dB of loss over the operating bandwidth of the device. The excess loss is mainly due to reflection and scattering.

The slightly different performance between the two conversions is caused by the difference in the evolution of TE and TM modes in triangular shaped perturbed sections, polarization-dependent

reflection/scattering loss, and the exact optimized dimensions being difficult to realize in fabrication.

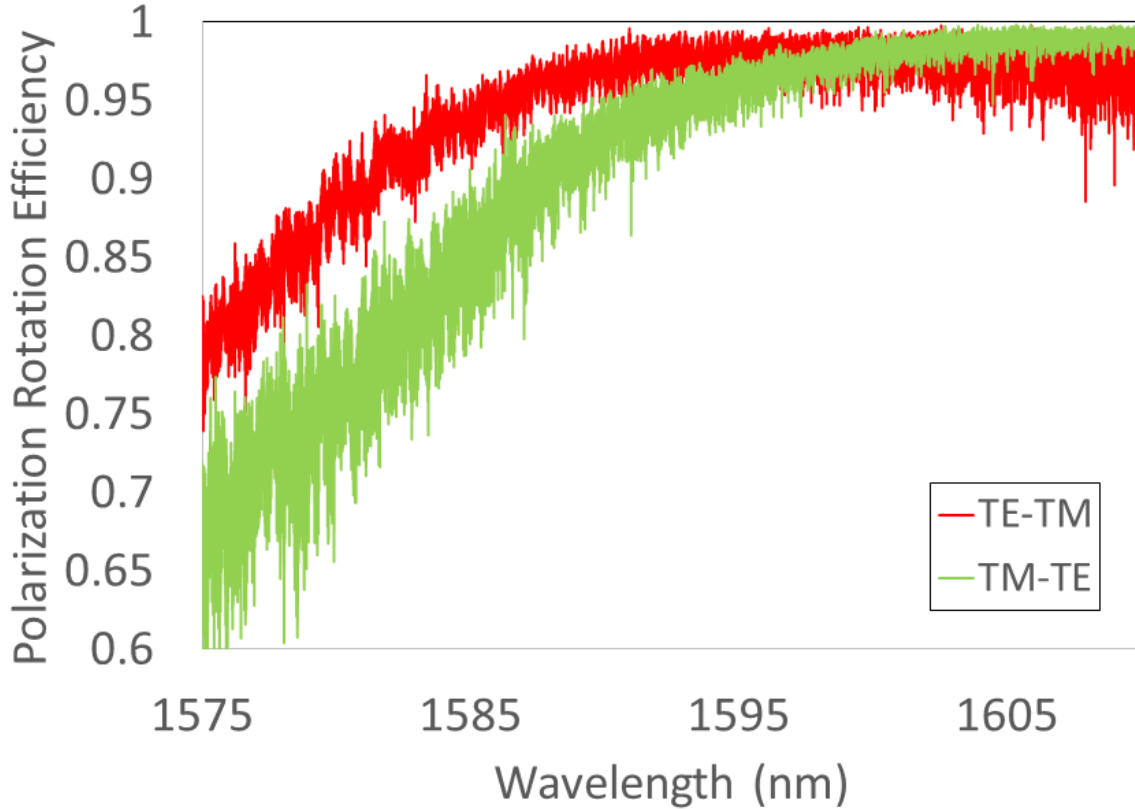


Fig.5. 8. PRE for the fabricated devices (with triangular shaped perturbations) over the operating wavelengths.

In the simulations, we predicted that the peak ER would be 26.6 dB, at a wavelength of 1552 nm, for the TE-TM conversion; and 32.5 dB, at 1544 nm, for the TM-TE conversion. And that the ER would be greater than 10 dB over the entire C-band. Experimentally, the PRE is over 80% between 1575 nm to 1610 nm for TE-TM, and over 80% between 1583 nm to 1610 nm for TM-TE. For the TE-TM conversion, the peak PRE is found to be ~97.5 %, at ~1595 nm; and ~98.75 %, at ~1607 nm, for the TM-TE conversion.

The calculated PRE is centered at 1552 nm for TE-TM, and at 1544 nm for TM-TE. The peak PRE is 99.79 % and 99.95 % for the two conversions, respectively. The PRE remains greater than

90% over the entire C-band. Experimentally, the PRE is over 80% between 1575 nm and 1610 nm, for TE-TM; and between 1583 nm and 1610 nm, for TM-TE. The peak experimental PRE is found to be ~97.5 %, at ~1595 nm, for TE-TM; and ~98.75 %, at ~1607 nm, for TM-TE.

The experimental results show a significantly lower level of performance than the simulated results. As we have shown in Chapter 3, the design is fabrication sensitive. The deviations from the optimized geometry parameters of our device are the main reasons for the optimal peak wavelength shift and degradation of the ER in our fabricated devices. A more detailed study is presented in Section 5.4.

5.4 Discussions on the Experimental Results

The degradation in performance of the fabricated devices are mainly due to errors introduced in fabrication steps. In simulations, we have observed that both PR designs are sensitive to geometrical parameters deviations. As shown in Chapter 3, in order to maintain the device performance ($ER > 20$ dB) for the PR designs, less than 5 nm variation in geometrical parameters in required. Efforts had been made to measure the actual dimensions in the fabricated devices using SEM. However, the measurement has a ± 10 nm error and thus cannot provide useful information for better understanding the device performance. Future efforts could be made in measuring the actual dimensions using other techniques including transmission electron microscopy (TEM), atomic force microscopy (AFM). In this thesis, validation of the demonstrated PR designs were done through calculations considering fabrication deviations. Table 5.1 summarizes the fabrication tolerances for both PR designs.

TABLE 5. 1. SUMMARY OF THE FABRICATION TOLERANCES

Geometrical Parameters	First PR Design (with rectangular shaped perturbations) Fabrication Tolerance (nm)	Second PR Design (with tapered shaped perturbations) Fabrication Tolerance (nm)
W_c	± 3	NA
W_s	± 15	± 3
W_c+W_s	NA	± 2
L_s	± 25	NA
L_{HT}	NA	± 6
H_c	± 5	± 4
H_s	± 6	$-2 \sim 6$

As we can see from Table 5.1, the width of the waveguide core region (presented by W_c for the first design and W_c+W_s for the second design) is the most crucial design parameter for both designs. As shown in Chapter 3, a ± 10 -nm variation in the core width will degrade the ER by 23 dB for the first design (with rectangular shaped perturbed sections) and by 20 dB for the second design (with triangular shaped perturbed sections). W_s also has a significant effect on the second design's performance.

Waveguide core width variations of ± 15 nm were cross-checked by the FDTD method to show the effect they have on the first PR design. These examples are for illustration purposes only, and thus only TE inputs were considered. Table 5.2 summarizes, in detail, the effects introduced by waveguide core width variations for the first PR design.

TABLE 5. 2. SUMMARY OF THE IMPACT OF CORE WIDTH VARIATIONS BY THE FDTD METHOD FOR THE FIRST DESIGN

W_c (μm)	Deviation from the optimized W_c (μm)	Extinction Ratio at 1550 nm Wavelength (dB)	Peak Wavelength (nm)	Extinction Ratio at Peak Wavelength (dB)
0.385	0.015	4.01	1492	13.66
0.39	0.01	11.3	1520	16.674
0.395	0.005	14.81	1533	19.44
0.4	0	25.38	1550	25.38
0.405	0.005	17.6	1563	30.175
0.41	0.01	11.4	1575	28.7
0.415	0.015	6.81	1590	21.3

From Table 5.2, we can see that a variation in W_c is not only responsible for the degradation of ER, but it also causes the peak wavelength shift. For a W_c deviation of ± 15 nm from the optimized value, the ER degrades from 25.38 dB to 4.01 dB, at a wavelength of 1550 nm. We also observed a shift in the peak wavelength for this deviation, where at the new peak wavelength, ER is maintained above 10 dB. For a W_c deviation of -15 nm, the peak ER is found to be 13.66 dB at a new peak wavelength of 1492 nm. Here, the ER is maintained above 10 dB over the wavelength range of 1456 nm to 1521 nm. For a W_c deviation of 15 nm, the peak ER is found to be 21.3 dB at a new peak wavelength of 1590 nm. Here, the ER is maintained above 10 dB over the wavelength range of 1563 nm to 1617 nm.

By taking the fabrication variations of W_c into consideration, Fig. 5.9 compares the simulated ER to the measured ER. The simulated ER demonstrates a similar trend to that of the measured ER.

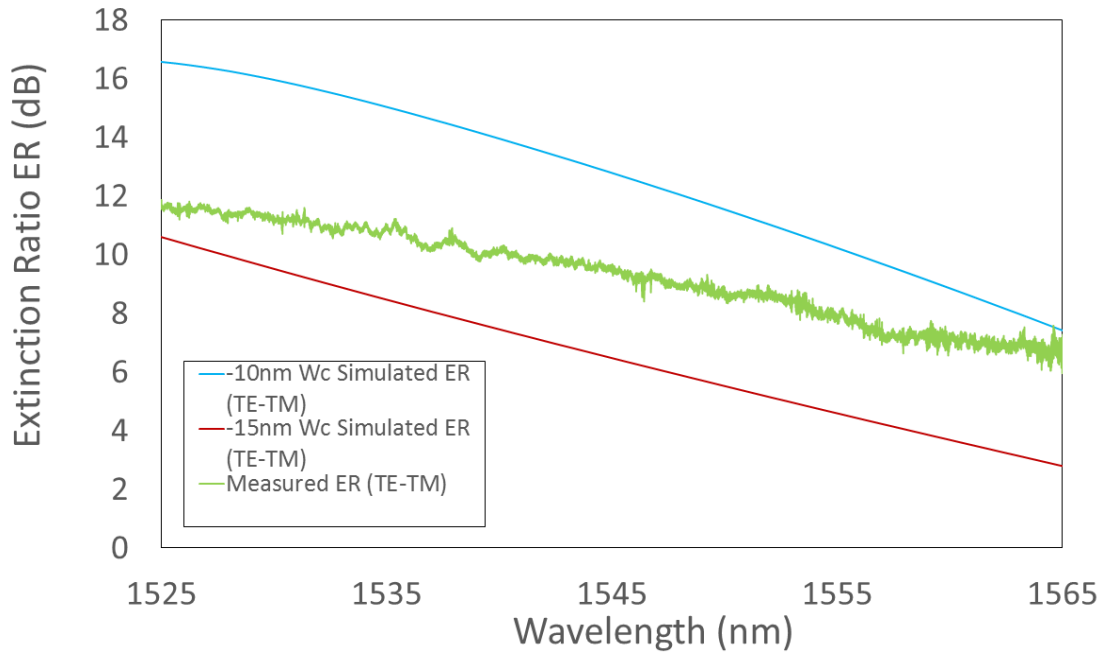


Fig.5. 9. Comparison between the measured ER and the simulated ER considering fabrication deviations.

Based on the results shown in Table 5.2 and Fig. 5.9, we believe that the fabricated PR can demonstrate a higher ER at wavelengths shorter than 1525 nm; however, this assumption cannot be proven with the available testing equipment.

The effect of the core width (W_s+W_c) variation in the second PR design is summarized in Table 5.3. The data was obtained by FDTD simulations. The variation in the core width is done by fixing W_s while varying W_s+W_c .

TABLE 5.3. SUMMARY OF IMPACT OF CORE WIDTH VARIATION BY THE FDTD METHOD FOR THE SECOND DESIGN

W_c+W_s (μm)	Deviation from the optimized W_c+W_s (μm)	Extinction Ratio at 1550 nm Wavelength (dB)	Peak Wavelength (nm)	Extinction Ratio at Peak Wavelength (dB)
0.385	0.015	-3.97	1493	10.5
0.39	0.01	1.39	1514	13.9
0.395	0.005	8.46	1534	18.02
0.4	0	26.2	1552	26.6
0.405	0.005	8.3	1569	31.5
0.41	0.01	2.03	1585	20.716
0.415	0.015	-3.08	1603	16.2

From Table 5.3, we can observe the same effect as shown in Table 5.2—that a variation in W_c is not only responsible for the degradation of ER, but it also causes the peak wavelength shift. For a W_c+W_s deviation of ± 15 nm from the optimized value, the ER degrades from 26.6 dB to ~ -3 dB, at a wavelength of 1550 nm. We also observed a shift in the peak wavelength for this deviation, where at the new peak wavelength, ER is maintained over 10 dB. For a W_c+W_s deviation of -15 nm, the peak ER is found to be 10.5 dB at a new peak wavelength of 1493 nm. For a W_c+W_s deviation of 15 nm, peak ER is found to be 16.2 dB at a new peak wavelength of 1603 nm. Here, the

As shown in Table 5.1, the slab width (W_s) is also crucial to the second PR design. The effect of the W_s variation in the second PR design is summarized in Table 5.4. This data was obtained from FDTD simulations. Please note that in all of the following cases, W_s+W_c maintains the same value of 400 nm. And as the examples provided below are for illustration purposes only, only TE inputs were considered.

TABLE 5. 4. SUMMARY OF THE IMPACT OF SLAB WIDTH VARIATION BY THE FDTD METHOD FOR THE SECOND DESIGN

W_s (μm)	Deviation from the optimized W_s (μm)	Extinction Ratio at 1550 nm Wavelength (dB)	Peak Wavelength (nm)	Extinction Ratio at Peak Wavelength (dB)
0.09	0.01	10.24	1564	17.14
0.095	0.005	16.2	1558	26.67
0.098	0.002	22.7	1554	31.2
0.1	0	26.2	1552	26.6
0.102	0.002	20.8	1549	21.33
0.105	0.005	15	1545	16.85
0.11	0.01	9.8	1539	12.3

From the results summarized in Table 5.4, we can see that the slab width (W_s) also affects the device performance, but not as significantly as the core width (W_s+W_c). A ± 10 nm variation in W_s results in a ~ 12 -nm peak wavelength shift, with a ~ 16 -dB degradation in the ER at a 1550-nm wavelength. Comparing the results summarized in Table 5.3 to that of Table 5.4, we can find that the total width W_s+W_c variations have a more significant effect on the device performance.

By taking fabrication variations of (W_s+W_c) into consideration, Fig. 5.10 compares the simulated and measured ER values. In order to reduce the effect of the large noise at longer wavelengths, a moving average of every 50 data points were calculated and plotted (darker green line) for the measured ER. The simulated ER demonstrates a similar trend to that of the measured ER.

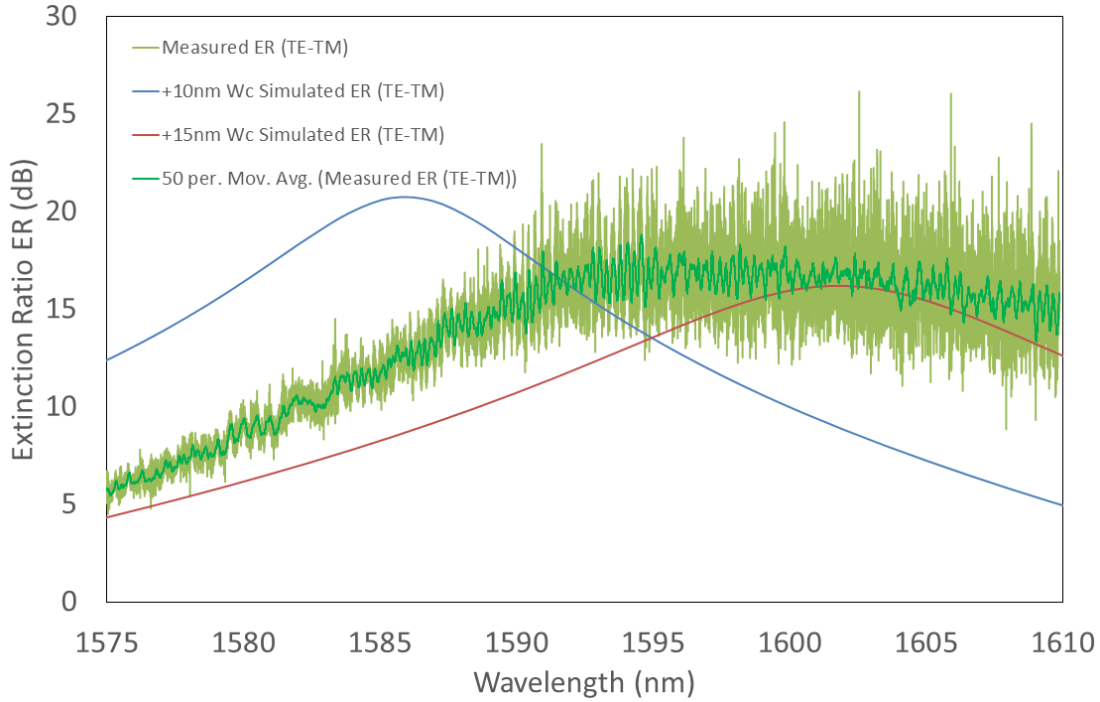


Fig.5. 10. Comparison of the measured ER and the simulated ER, considering fabrication deviations.

In summary, the performance degradation and peak wavelength shifts observed in the measured results are mainly affected by fabrication variations in the waveguide core width (W_c for the first PR design and W_c+W_s for the second PR design). Based on the simulations, the fabrication deviations in the waveguide core width are found to be around -10 nm to -15 nm, for the first PR design, and around 10 nm to 15 nm for the second PR design. The discrepancy in the waveguide core width deviations for the two different PR designs is because the two are formed by using different mask layers (see Section 4.5). Fabrication deviations in other design parameters (e.g., H_c , H_s , W_s , L_s/L_{HT}) would also affect the performance of the fabricated devices, but not as significantly as that of the waveguide core width.

Furthermore, the deviations introduced in fabrication not only influenced the performance of the fabricated devices, but also affected the GCs. The GCs used in the testing circuits were designed

to have a center wavelength at ~ 1550 nm for both polarizations [1]. The simulated peak IL for the grating couplers was - 5.5 dB, while the measured peak IL was -10.2 dB [1]. Fig. 5.11 shows the measured transmission spectra for the TE and TM inputs from the reference circuits, where no PR structures were included. From the plot, we can see that the peak wavelengths for the TE and TM GCs have been shifted to 1525 nm. The excess loss measured at the peak wavelengths was caused by waveguide bends and misalignment between the FA and the GCs. The peak wavelength shifts in the GCs are believed to be the reason for the large noise observed at longer wavelengths, as the normalization was done with respect to a reference that also had more loss at these wavelengths.

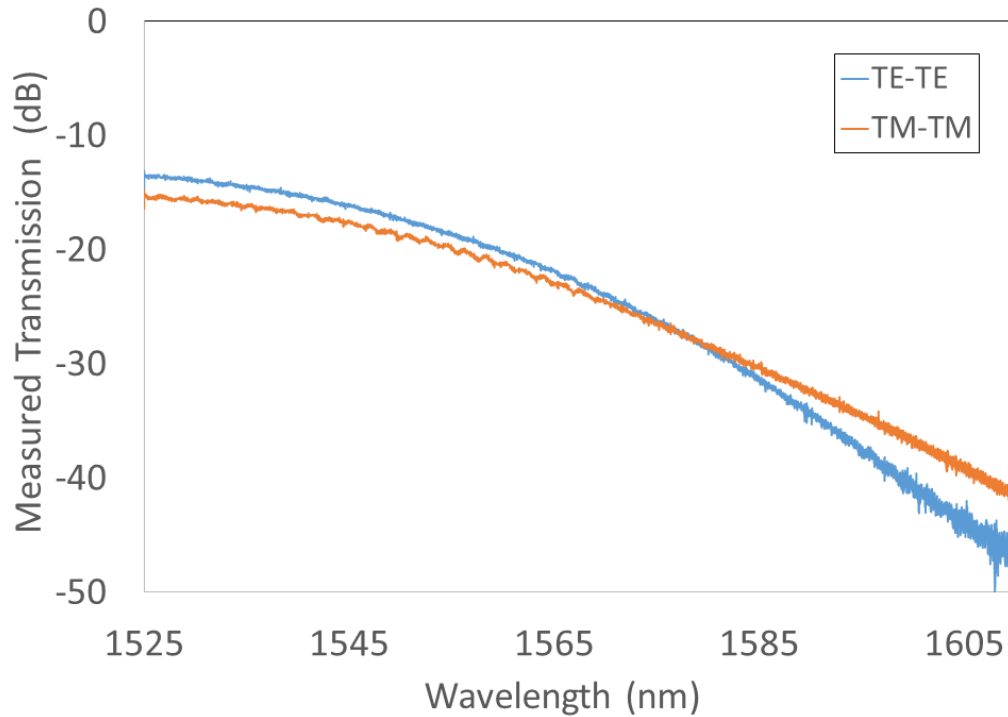


Fig.5. 11. Measured transmission for TE and TM inputs of the reference circuits.

5.5 Discussions on Fabrication Tolerance

The performance of the fabricated devices is influenced by deviations in the geometrical parameters. These deviations may be introduced by fabrication errors, fabrication bias, or misalignment between different mask layers.

As presented in Chapter 4, the current fabrication technology limits the resolution in fabrication. In my designs, WG layers (220-nm thick) and SK layers (60-nm thick) are used to form the proposed PR structures. Based on the information obtained from the foundry, the SOI wafer used for fabrication may have a ± 10 nm variation in the thickness of the silicon layer, and a ± 10 nm variation in the thickness of the SK layer. In addition, as each layer will either experience different processing steps, or use different plates of masks, each layer will be slightly different [2]. Fabrication defects, such as sidewall roughness and rounded corners (as shown in Fig. 5.1(a)), will also degrade the performance of the fabricated devices. In order to compensate for the fabrication errors, we can include more design variations in the fabricated chip. However, more variations would mean more space required on the chip.

Fabrication bias, as mentioned in Chapter 4, means that all the fabricated dimensions will be off target, except for the designated ones. In order to avoid this, we would try to use the designated dimensions whenever they are applicable. In the mask designs, all dimensions are chosen based on the fitted trend lines shown in Fig. 4.4. However, the fitted values may not present the actual fabricated dimensions. In addition, the waveguide structure in the first PR design is defined by using both WG_COR and WG_TRE layers, making the core width of the fabricated devices harder to control.

Since two lithography steps are required to define the device structures for both designs, misalignment between different mask layers can be crucial. A typical misalignment error is ± 20 nm [3]. One solution would be to include more design variations to eliminate this effect. In this fabrication run, not enough space was given to include enough design variations to compensate for this effect. Recently, a self-alignment fabrication process had been proposed to enhance performance repeatability and manufactural yield [4]. As shown in Fig. 5.12, a hard mask is used to protect the Si rib from the second etching step that defines the slab regions in their design. However, this method has not yet been made available in standard foundry services.

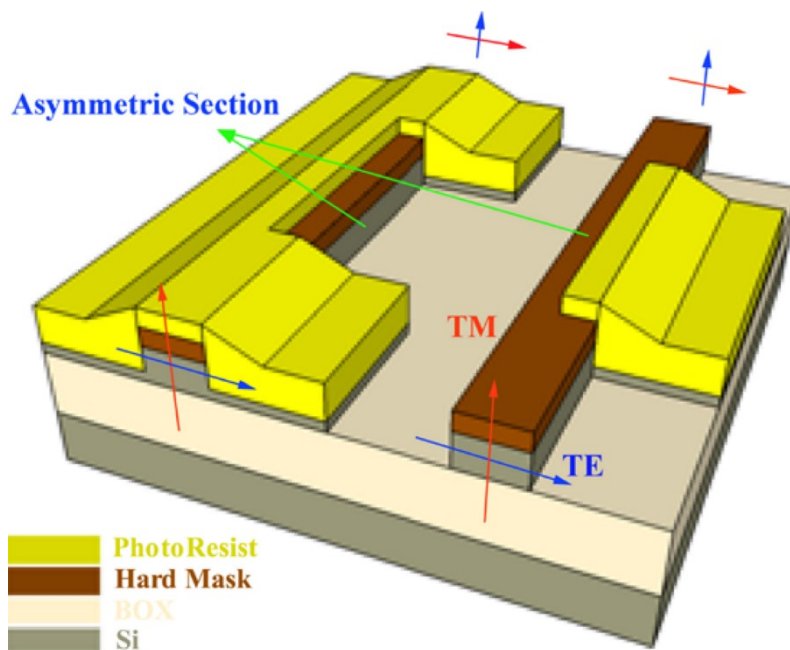


Fig.5. 12. Self-alignment process by using a hard mask for the rib waveguides (left) and channel waveguides (right) [4].

References

- [1] Y. Wang, J. Flueckiger, C. Lin, and L. Chrostowski, “Universal Grating Coupler Design,” in Photonics North, 2013.
- [2] J. Zhang, Personal Communication via Emails, Aug 18th, 2014.
- [3] J. Zhang, Personal Communication via Emails, Aug 6th, 2014.
- [4] H. Zhou, C. LI, A.L. Eujin, L. Jian, M. Yu and G.Lo, “Ultra-Compact and broadband Si photonics polarization rotator by self-alignment process”, Optics Express, Vol. 23, No. 5, pp. 6815-6821, Mar. 2015

Chapter 6

Conclusions and Future Work

This thesis covers the detailed design, analysis, fabrication preparation, and performance characterization of two polarization rotator (PR) designs on the 220-nm silicon-on-insulator (SOI) platform. These PR designs feature compact device footprints and a CMOS-compatible two-step etching fabrication process. Ultimately, we demonstrated the performance of both PR designs by simulations and experiments.

Both PR designs are based on asymmetrical periodic loaded structures. Such structures have been extensively studied in other platforms (e.g., III-V materials), and have recently been studied on the silicon platform [1][2]. In the studies on the silicon platform, the period of alternation is chosen to be similar to the periods of Bragg gratings, thus resulting in long, narrowband devices. Unlike these designs, our designs use solely the polarization effect in asymmetrical periodic loaded structures. The first PR design is formed by a rib waveguide with longitudinal periodic perturbations in the slab section of the waveguide, where the periodic loadings on the left and right sides are mismatched. The second PR design is a channel waveguide with longitudinal triangular shaped periodic perturbations along the waveguide, where the periodic perturbations on either side

are mismatched. The resultant devices have compact lengths of 15.78 μm and 20.88 μm , respectively. Both designs are approximately 18 times shorter than the shortest devices demonstrated based on the same structures so far [2].

The design and in-depth analysis of both PRs have been presented in this thesis. The numerical modeling of the two devices are based on numerical methods, including the finite-difference method, the mode-film matching method, the eigen mode expansion method, and the finite-difference time-domain method. Simulations are performed to find the optimal design parameters, to characterize the performance of the proposed designs, and to investigate the fabrication tolerance of the devices.

In the simulations, we focused on the performance of the PR designs over the entire C-band. The three performance parameters we investigated were the extinction ratio (ER), polarization rotation efficiency (PRE), and insertion loss (IL). By simulations, for the first PR design (with rectangular shaped perturbations), we have found the peak ER for the TE-TM conversion to be 25.45 dB, at a wavelength of 1549 nm; while the peak ER for the TM-TE conversion is 25.01 dB, at 1553 nm. The simulated ER is >10 dB for both conversions across the entire C-band. The calculated PRE is above 90% over a wavelength range of 1514 nm to 1579 nm, centered at ~1550 nm, for the TE and TM inputs. The peak PRE for the TE-TM conversion is 99.72 %, at 1549 nm; and the peak PRE for the TM-TE conversion is 99.68%, at 1553 nm. At a wavelength of 1550 nm, the PRE is 99.7% and 99.61% for the TE-TM and TM-TE conversions, respectively. Simulations show that the IL of the first PR design is less than 0.5 dB over the operating wavelength range.

Simulations on the second PR design (with triangular shaped perturbations) showed that the peak ER for the TE-TM conversion is 26.6 dB, at a wavelength of 1552 nm; while the peak ER for the TM-TE conversion is 32.5 dB, at 1544 nm. It is also observed that the simulated ER is >10

dB across the wavelength range of 1535 nm to 1567 nm, for the TE-TM conversion, and 1528 nm to 1558 nm for the TM-TE conversion. For TE-TM, the calculated PRE is above 90% over the wavelength range of 1535 nm to 1568 nm, and the peak PRE is 99.79%, at 1552 nm. For TM-TE the PRE is above 90% from 1527 nm to 1560 nm, and the peak PRE is 99.95%, at 1544 nm. The simulated IL is less than -2 dB over the operating wavelengths.

Even though the simulations of the PR designs demonstrate good performance over the C-band, the proposed designs are sensitive to fabrication errors. Fabrication tolerance analysis was performed on both designs to investigate the effects introduced by fabrication deviations. The width of the waveguide core region is found to be the most crucial parameter for both designs. In addition, for the second PR design, the slab width is also a crucial parameter, as varying it ultimately changes the waveguide core width. In order to maintain good performance, deviations on these crucial parameters have to fall within ± 3 nm.

The fabrication of both PR designs was carried out by IMEC- ePIXfab in Belgium. The fabrication technology features an SOI wafer with a 220-nm top Si film and a 2000-nm buried-oxide (BOX) layer based on a 193-nm-deep ultraviolet lithography platform. The mask layout was designed at Carleton University using Mentor Graphics' IC-design tool—Pyxis Technology—and the layout was generated by the AMPLE scripting language. In the testing circuit, three identical devices were fabricated and connected to a pair of TE grating couplers (GCs), a pair of TM GCs, and a pair consisting of 1 TE GC and 1 TM GC. The mask layout consisted of testing circuits for both polarization rotator designs, and the reference circuits, where no PR structures were used. The characterization of the fabricated devices was done at Carleton University by using a tunable laser covering a wavelength range of 1525 nm to 1610 nm, and was analyzed via an optical vector

analyzer. A 6-channel polarization maintaining (PM) fiber array (FA) (with three TE channels and three TM channels) was used to inject and collect light from the devices.

The fabricated PR designs have demonstrated the ability to convert TE inputs to TM, and vice versa. For the first design, the peak ER is 11.8 dB, at wavelength of ~ 1525 nm. For both conversions, the ER is greater than 8 dB over a wavelength range of 1525 nm to 1553 nm, and is greater than 6 dB over the entire C-band. At a wavelength of approximately 1525 nm, the highest PRE obtained for the TE-TM conversion is 93.5 %. For the TM-TE conversion, this value is 93.9 %. For both conversions, the PRE stays above 80% for the wavelength range of 1525 nm to 1565 nm. For the second PR design, the peak ER is found to be ~ 16 dB, at ~ 1593 nm, for the TE-TM conversion; and ~ 20 dB, at ~ 1605 nm, for the TM-TE conversion. The PRE is over 80% for the wavelength range of 1575 nm to 1610 nm, for the TE-TM conversion, and is over 80% for the wavelength range of 1583 nm to 1610 nm, for the TM-TE conversion. For the TE-TM conversion, the peak PRE is found to be $\sim 97.5\%$, at ~ 1595 nm. For the TM-TE conversion, the peak PRE is found to be $\sim 98.75\%$, at ~ 1607 nm.

The experimental results proved that the fabricated structures can work as PRs for certain wavelength ranges; however, the measured peak wavelengths shift by ~ 25 nm for the first design, and ~ 50 nm for the second design. The measured results also show degradation in the performance of the devices. The observed peak wavelength shifts and the degradation in performance are caused by deviations in the geometrical parameters (especially deviations in the waveguide core width). The deviations are introduced by fabrication errors and defects, fabrication bias, and misalignment between different masks.

6.1 Significant Contribution

The significance of this work is that, by only introducing the periodic loaded structures, mode rotation can be achieved by asymmetric waveguide sections in the commonly used 220-nm-thick SOI platform—while maintaining a compact device footprint and a wide operating bandwidth.

The 220-nm-thick SOI platform is too thin to obtain fully hybridized modes (50% TE and 50% TM) by simply breaking the waveguide symmetry. We addressed this issue by periodically alternating asymmetrical structures to achieve a full polarization rotation. The periodic structures also allow for flexible selection of geometric parameters, as for any asymmetrical waveguide section there will be a (half beat length, periods) combination that can be used to obtain full rotation. Our designs, supported with experimental demonstration, present the most compact polarization rotators utilizing the asymmetric periodic loaded SOI waveguides, thus far. The fabrication of these devices is fully CMOS-compatible, via a simple two-step lithography process, and no special claddings are required to break the vertical symmetry. Furthermore, we believe this work opens a new prospect for flexible, compact, and highly efficient polarization rotator designs on the SOI platform.

6.2 Publications

- Y. Sun, Y. Xiong and W. N. Ye, Compact SOI Polarization Rotator using Asymmetric Periodic Loaded Waveguides, *IEEE Photonics Journal*, 8(1), pp.1-8, Feb 2016.
- Y. Sun and W. N. Ye, CMOS-compatible polarization rotator design based on asymmetrical periodic loaded waveguide structure, accepted for oral presentation, *Photonics West 2016*

- Y. Sun and W. N. Ye, Compact polarization rotator design based on asymmetrical periodic loaded SOI waveguides, oral presentation, DOI: 10.1109/PN.2015.7292490, Photonics North 2015.

6.3 Achievements

- Elected President, SPIE Carleton University Student Chapter (2014-2015)
- Ed Ireland Engineering Award, 2014

6.4 Future Works

Several directions for future work based on this thesis can be recommended:

1. Future investigation and development on the current PR designs

The main effort would be to optimize the fabrication process to reduce the effects imposed by fabrication deviations. This could include optimizing the mask layout design by fully understanding the effects imposed by each design parameter, and by including more design variations (with more space required on chip). Other possible solutions include trying different fabrication technologies and following designated fabrication steps [3] designed for devices with stringent fabrication requirements.

2. Further investigation of the asymmetrical periodic loaded structures

As mentioned in this thesis, the use of asymmetrical periodic loaded structures brings more flexibility to PR designs on the 220-nm SOI platform. It would be of worth to further investigate this structure to see if there are more efficient, compact, and fabrication-tolerant designs. Future efforts can also be made to design PRs aiming for different wavelength ranges. Furthermore, the asymmetrical loaded waveguide sections do not need to be cut-

corner structures (as used in this thesis); structures like slanted sidewalls or subwavelength trenches can be used. The designer would need to ensure that the new structures could be fabricated by the available fabrication technologies.

3. Application of the current PR designs

In the future, the demonstrated PR designs in this thesis could potentially be extended to polarization splitting-rotating devices. One possible way would be to integrate this structure into an asymmetrical directional coupler, with properly designed widths, to satisfy the phase-matching conditions. The designer would need to investigate the mode exchange between the PR structure and the input waveguide. In addition, the PR designs demonstrated could also be combined with an existing silicon-photonics modulator to realize a dual-polarization modulator, which is widely used in high-speed coherent optical communication systems.

References

- [1] H. Okayama, Y. Onawa, D. Shimura, H. Yaegashi, and H. Sasaki, “Polarization rotation Bragg grating using Si wire waveguide with non-vertical sidewall”, *Opt. Express* 22(25), 31371-31378 (2014).
- [2] H. Yun, J. Flueckiger, Z. Chen, Y. Wang, L. Chrostowski, and N. A.F. Jaeger, “A wavelength-selective polarization rotating reflector using a partially-etched asymmetric Bragg grating on an SOI strip waveguide”, *IEEE Group IV Photonics Conference*, Vancouver, BC (2015)
- [3] H. Zhou, C. LI, A.L. Eujin, L. Jian, M. Yu and G.Lo, “Ultra-Compact and broadband Si photonics polarization rotator by self-alignment process”, *Optics Express*, Vol. 23, No. 5, pp. 6815-6821, Mar. 2015

Appendix A

Ample scripts written for mask layout generation of the two polarization rotators.

```
function PeriodicDoubleEtchPRiRoutenoGC()
{
//first PR design

local x=0;

local x1=3;

local x2=13;

local y=0;

local y1=45;

local y2=90;

local dev2y=-415;

local R=15;

local R1=20;

local cladwidth=2;

//Based on WG bias, WG_COREwidth=420nm(on mask) to give 400nm(on chip)

local WG_width=0.4;

local WG_width_flavor=[-0.04, -0.02, -0.01, 0, 0.01, 0.02, 0.04];

//10

//Based on WG bias, WG_TREwidth=325nm(on mask)to give 300nm (on chip)

local WGTrench_width=0.32;

//Based on SK bias, SKwidth=260nm(on mask) to give 300nm(on chip)

local SKtrench_width=0.26;

local WGTrench_width_flavor=[-0.04, -0.015, 0, 0.015, 0.04];

local SKTrench_width_flavor=[-0.04, -0.01, 0, 0.01, 0.04];

local k;
```

```

local kk;

for (kk=0; kk<length(WG_width_flavor); kk=kk+1){
  for(k=0;k<2;k=k+1){
    $add_text("psr215TE_TE",[0.6+x+WG_width_flavor[kk], 15.5],"WG_TEXT", 0.5,@right);
    build_PeriodicDoubleEtchPR(1.3, WGtrench_width, SKtrench_width, WG_width+WG_width_flavor[kk], 1.3*12, 12,
x, y);
    $add_text("psr215TM_TM",[0.6+x1+5+WG_width_flavor[kk], 15.5],"WG_TEXT", 0.5,@right);
    build_PeriodicDoubleEtchPR(1.3, WGtrench_width, SKtrench_width, WG_width+WG_width_flavor[kk], 1.3*12, 12,
x1+R1-R, y);
    $add_text("psr215TE_TM",[0.6+x2+5+WG_width_flavor[kk], 15.5],"WG_TEXT", 0.5,@right);
    build_PeriodicDoubleEtchPR(1.3, WGtrench_width, SKtrench_width, WG_width+WG_width_flavor[kk], 1.3*12, 12,
x2+R1-R, y);
    x=x+82;
    x1=x1+82;
    x2=x2+82;
  }
}

for (kk=0; kk<length(WGTrench_width_flavor); kk=kk+1){
  for(k=0;k<2;k=k+1){ $add_text("psr215TE_TE",[0.6+x, 15.5],"WG_TEXT", 0.5,@right);
  $add_text("psr215TE_TE",[0.6+x+5, 15.5],"WG_TEXT", 0.5,@right);
  build_PeriodicDoubleEtchPR(1.3, WGtrench_width+WGTrench_width_flavor[kk],
SKtrench_width+SKTrench_width_flavor[kk], WG_width, 1.3*12, 12, x, y);
  $add_text("psr215TM_TM",[0.6+x1+5, 15.5],"WG_TEXT", 0.5,@right);
  build_PeriodicDoubleEtchPR(1.3, WGtrench_width+WGTrench_width_flavor[kk],
SKtrench_width+SKTrench_width_flavor[kk], WG_width, 1.3*12, 12, x1+R1-R, y);
  $add_text("psr215TE_TM",[0.6+x2+5, 15.5],"WG_TEXT", 0.5,@right);
  build_PeriodicDoubleEtchPR(1.3, WGtrench_width+WGTrench_width_flavor[kk],
SKtrench_width+SKTrench_width_flavor[kk], WG_width, 1.3*12, 12, x2+R1-R, y);
  x=x+82;
  x1=x1+82;
  x2=x2+82;
}
}

```

```

}

x=0;

x1=3;

x2=13;

//for 220nm thickness

for (kk=0; kk<length(WG_width_flavor); kk=kk+1){

    $add_text("psr220TE_TE",[0.6+x+WG_width_flavor[kk], 15.5+dev2y],"WG_TEXT", 0.5,@right);

    build_PeriodicDoubleEtchPR(1.33, WGTrench_width, SKTrench_width, WG_width+WG_width_flavor[kk], 1.33*12,
12, x, y+dev2y);

    $add_text("psr220TM_TM",[0.6+x1+5+WG_width_flavor[kk], 15.5+dev2y],"WG_TEXT", 0.5,@right);

    build_PeriodicDoubleEtchPR(1.33, WGTrench_width, SKTrench_width, WG_width+WG_width_flavor[kk], 1.33*12,
12, x1+R1-R, y+dev2y);

    $add_text("psr220TE_TM",[0.6+x2+5+WG_width_flavor[kk], 15.5+dev2y],"WG_TEXT", 0.5,@right);

    build_PeriodicDoubleEtchPR(1.33, WGTrench_width, SKTrench_width, WG_width+WG_width_flavor[kk], 1.33*12,
12, x2+R1-R, y+dev2y);

    x=x+82;

    x1=x1+82;

    x2=x2+82;

}

for (kk=0; kk<length(WGTrench_width_flavor); kk=kk+1){

    $add_text("psr220TE_TE",[0.6+x, 15.5+dev2y],"WG_TEXT", 0.5,@right);

//for 220nm thick wafer

    build_PeriodicDoubleEtchPR(1.33, WGTrench_width+WGTrench_width_flavor[kk],
SKTrench_width+SKTrench_width_flavor[kk], WG_width, 1.33*12, 12, x, y+dev2y);

    $add_text("psr220TM_TM",[0.6+x1+5, 15.5+dev2y],"WG_TEXT", 0.5,@right);

//220nm thickness

    build_PeriodicDoubleEtchPR(1.33, WGTrench_width+WGTrench_width_flavor[kk],
SKTrench_width+SKTrench_width_flavor[kk], WG_width, 1.33*12, 12, x1+R1-R, y+dev2y);

    $add_text("psr220TE_TM",[0.6+x2+5, 15.5+dev2y],"WG_TEXT", 0.5,@right);

    build_PeriodicDoubleEtchPR(1.33, WGTrench_width+WGTrench_width_flavor[kk],
SKTrench_width+SKTrench_width_flavor[kk], WG_width, 1.33*12, 12, x2+R1-R, y+dev2y);

    x=x+82;

    x1=x1+82;

```

```

x2=x2+82;
}
//for 210nm thickness
for (kk=0; kk<length(WG_width_flavor); kk=kk+1){
  $add_text("psr210TE_TE",[0.6+x+5+WG_width_flavor[kk], 15.5+dev2y],"WG_TEXT", 0.5,@right);
  build_PeriodicDoubleEtchPR(1.28, WGTrench_width, SKtrench_width, WG_width+WG_width_flavor[kk], 1.28*12,
12, x, y+dev2y);
  $add_text("psr210TM_TM",[0.6+x1+5+WG_width_flavor[kk], 15.5+dev2y],"WG_TEXT", 0.5,@right);
  build_PeriodicDoubleEtchPR(1.28, WGTrench_width, SKtrench_width, WG_width+WG_width_flavor[kk], 1.28*12,
12, x1+R1-R, y+dev2y);
  $add_text("psr210TE_TM",[0.6+x2+5+WG_width_flavor[kk], 15.5+dev2y],"WG_TEXT", 0.5,@right);
  build_PeriodicDoubleEtchPR(1.28, WGTrench_width, SKtrench_width, WG_width+WG_width_flavor[kk], 1.28*12,
12, x2+R1-R, y+dev2y);
  x=x+82;
  x1=x1+82;
  x2=x2+82;
}
for (kk=0; kk<length(WGTrench_width_flavor); kk=kk+1){
  $add_text("psr210TE_TE",[0.6+x, 15.5+dev2y],"WG_TEXT", 0.5,@right);
//for 210nm thick wafer
  build_PeriodicDoubleEtchPR(1.28, WGTrench_width+WGTrench_width_flavor[kk],
SKtrench_width+SKTrench_width_flavor[kk], WG_width, 1.28*12, 12, x, y+dev2y);

  $add_text("psr210TM_TM",[0.6+x1+5, 15.5+dev2y],"WG_TEXT", 0.5,@right);
//210nm thickness
  build_PeriodicDoubleEtchPR(1.28, WGTrench_width+WGTrench_width_flavor[kk],
SKtrench_width+SKTrench_width_flavor[kk], WG_width, 1.28*12, 12, x1+R1-R, y+dev2y);

  $add_text("psr210TE_TM",[0.6+x2+5, 15.5+dev2y],"WG_TEXT", 0.5,@right);

  build_PeriodicDoubleEtchPR(1.28, WGTrench_width+WGTrench_width_flavor[kk],
SKtrench_width+SKTrench_width_flavor[kk], WG_width, 1.28*12, 12, x2+R1-R, y+dev2y);

```

```

x=x+82;

x1=x1+82;

x2=x2+82;

}

}

// **** REPLACE *EMPTY*:

function build_PeriodicDoubleEtchPR(SlabL:number {default=1.3}, WgtrenchW:number {default=0.325},
SKtrenchW:number {default=0.27}, WG_W:number {default=0.4}, WG_L:number {default=15.6}, PR:number
{default=12}, x:number {default=0}, y:number {default=0})

{
    local i;

    local Slab_Width=0.15;

    // Device definition here.

    $add_shape([[x,y], [x+WG_W+2*Slab_Width,-WG_L+y]], "WG_CORE", @internal, @keep, "drawing");

    $add_shape([[Slab_Width+WG_W+x+0.01,2+y], [Slab_Width+x-0.01,-0.5+y]], "WG_CORE", @internal, @keep,
"drawing");

    $add_shape([[Slab_Width+x-0.01,-WG_L+0.5+y], [WG_W+0.01+Slab_Width+x,-WG_L-2+y]], "WG_CORE",
@internal, @keep, "drawing");

    for (i=0;i<PR;i=i+2){

        $add_shape([[x+WG_W+Slab_Width,-i*SlabL+y], [x+WG_W+Slab_Width+SKtrenchW,-(i+1)*SlabL+y]], "SK_TRE",
@internal, @keep, "drawing");

        $add_shape([[Slab_Width+x-WgtrenchW,-i*SlabL+y], [x+Slab_Width,-(i+1)*SlabL+y]], "WG_TRENCH", @internal,
@keep, "drawing");

        $add_shape([[x+WG_W+Slab_Width,-(i+1)*SlabL+y], [x+WG_W+Slab_Width+WgtrenchW,-
(i+2)*SlabL+y]], "WG_TRENCH", @internal, @keep, "drawing");

        $add_shape([[Slab_Width+x-WgtrenchW,y-(i+1)*SlabL], [x+Slab_Width,-(i+2)*SlabL+y]], "SK_TRE", @internal,
@keep, "drawing");

    }

    $add_shape([[x-2,y+13.5], [x+WG_W+2*Slab_Width+2,y-WG_L-13.5]], "WG_CLAD" , @both);

    $add_shape([[x+Slab_Width-0.01,y-WG_L-1.5], [WG_W+Slab_Width+0.01+x,y-WG_L-1.5],
[WG_W+0.01+Slab_Width+x,y-WG_L-2.5], [0.25+Slab_Width+0.5*WG_W+x, y-WG_L-12.5],
[0.25+Slab_Width+0.5*WG_W+x, y-WG_L-13.5], [Slab_Width+0.5*WG_W-0.25+x, y-WG_L-13.5],
[Slab_Width+0.5*WG_W-0.25+x, y-WG_L-12.5], [Slab_Width+x-0.01, y-WG_L-2.5]], "WG_CORE", @internal, @keep,
"drawing");

```

```

    $add_shape([[x+Slab_Width-0.01,y+1.5], [WG_W+0.01+Slab_Width+x,y+1.5], [WG_W+0.01+Slab_Width+x,y+2.5],
    [0.25+Slab_Width+0.5*WG_W+x, y+12.5], [0.25+Slab_Width+0.5*WG_W+x, y+13.5], [Slab_Width+0.5*WG_W-
    0.25+x, y+13.5], [Slab_Width+0.5*WG_W-0.25+x, y+12.5], [x+Slab_Width-0.01, y+2.5]], "WG_CORE", @internal,
    @keep, "drawing");

    //add optical input/output ports

    $unselect_all();

    $set_autoselect(@true);

    $add_shape([[0.25+Slab_Width+0.5*WG_W+x, y-WG_L-13.5], [Slab_Width+0.5*WG_W-0.25+x, y-WG_L-
    13]], "WG_CORE", @both); //both means can see both in device and in cell mode

    $make_port(@signal, @bidirectional, "opt_in");

    $add_text("opt_in",[0.25+Slab_Width+0.5*WG_W+x, y-WG_L-13.5], "WG_TEXT", 0.5, @right);

    $unselect_all();

    $set_autoselect(@true);

    $add_shape([[0.25+Slab_Width+0.5*WG_W+x, y+13.5], [Slab_Width+0.5*WG_W-0.25+x,
    y+13]], "WG_CORE", @both); //both means can see both in device and in cell mode

    $make_port(@signal, @bidirectional, "opt_out");

    $add_text("opt_out",[0.25+Slab_Width+0.5*WG_W+x, y+13.5], "WG_TEXT", 0.5, @right);
}

// **** REPLACE *EMPTY*:

function PeriodicDoubleEtchPR_parameters(SlabL:optional number {default=1.3}, WgtrenchW:optional number
{default=0.325}, SKtrenchW:optional number {default=0.27}, WG_W:optional number {default=0.4}, WG_L:optional
number {default=15.6}, PR:optional number {default=12}, x:optional number {default=0}, y:optional number
{default=0})

{ return [ ["SlabL", $g(SlabL)], ["WgtrenchW", $g(WgtrenchW)], ["SKtrenchW", $g(SKtrenchW)],
["WG_W", $g(WG_W)], ["WG_L", $g(WG_L)], ["PR", $g(PR)], ["x", $g(x)], ["y", $g(y)]]; }

function arc_0_90(
    x1 : number,
    y1 : number,
    R : number,
    w2 : number,
    overlap : number,
    mask_layer : string

```

```

)
{
    //bending arc
    local m=500;
    local arc1=$get_arc([x1-w2/2,y1],[x1-w2/2-(R-w2/2)*(1-1/sqrt(2)),y1+(R-w2/2)/sqrt(2)],[x1-R,y1+(R-
w2/2)],m);
    local arc2=$get_arc([x1-R,y1+(R+w2/2)],[x1-
R+(R+w2/2)*sin(rad(45)),y1+(R+w2/2)*cos(rad(45))],[x1+w2/2,y1],m);
    local a=$create_vector(length(arc1)+2);
    local b=$create_vector(length(arc2)+2);
    a[0]=[x1-w2/2,y1-overlap];
    a[1:length(arc1)]=arc1[0:length(arc1)-1];
    a[length(arc1)+1]=[x1-R-overlap,y1+(R-w2/2)];
    b[0]=[x1-R-overlap,y1+(R+w2/2)];
    b[1:length(arc2)]=arc2[0:length(arc2)-1];
    b[length(arc2)+1]=[x1+w2/2,y1-overlap];
    $add_shape(append(a,b), mask_layer, @internal, @keep, "drawing");
}
function arc_180_90(
    x1 : number,
    y1 : number,
    R : number,
    w2 : number,
    overlap : number,
    mask_layer : string
)
{
    //bending arc
    local m=500;
    local arc1=$get_arc([x1-w2/2,y1],[x1-w2/2+(R+w2/2)*(1-
1/sqrt(2)),y1+(R+w2/2)/sqrt(2)],[x1+R,y1+(R+w2/2)],m);

```

```

        local arc2=$get_arc([x1+R,y1+(R-w2/2)],[x1+R-(R-w2/2)*sin(rad(45)),y1+(R-
w2/2)*cos(rad(45))],[x1+w2/2,y1],m);

        local a=$create_vector(length(arc1)+2);

        local b=$create_vector(length(arc2)+2);

        a[0]=[x1-w2/2,y1-overlap];

        a[1:length(arc1)]=arc1[0:length(arc1)-1];

        a[length(arc1)+1]=[x1+R+overlap,y1+(R+w2/2)];

        b[0]=[x1+R+overlap,y1+(R-w2/2)];

        b[1:length(arc2)]=arc2[0:length(arc2)-1];

        b[length(arc2)+1]=[x1+w2/2,y1-overlap];

        $add_shape(append(a,b), mask_layer, @internal, @keep, "drawing");
    }

```

```
function arc_270_180(
```

```
    x1 : number,
```

```
    y1 : number,
```

```
    R : number,
```

```
    w2 : number,
```

```
    overlap : number,
```

```
    mask_layer : string
```

```
)
```

```
{
```

```
    //bending arc
```

```
    local m=500;
```

```
    local arc1=$get_arc([x1,y1-w2/2],[x1-(R+w2/2)/sqrt(2),y1-w2/2+(R+w2/2)*(1-1/sqrt(2))],[x1-
(R+w2/2),y1+R],m);
```

```
    local arc2=$get_arc([x1-(R-w2/2),y1+R],[x1-(R-w2/2)*sin(rad(45)),y1+R-(R-
w2/2)*cos(rad(45))],[x1,y1+w2/2],m);
```

```
    local a=$create_vector(length(arc1)+2);
```

```
    local b=$create_vector(length(arc2)+2);
```

```
    a[0]=[x1+overlap,y1-w2/2];
```

```
    a[1:length(arc1)]=arc1[0:length(arc1)-1];
```

```
    a[length(arc1)+1]=[x1-(R+w2/2),y1+R+overlap];
```

```

    b[0]=[x1-(R-w2/2),y1+R+overlap];
    b[1:length(arc2)]=arc2[0:length(arc2)-1];
    b[length(arc2)+1]=[x1+overlap,y1+w2/2];
    $add_shape(append(a,b), mask_layer, @internal, @keep, "drawing");
}

function arc_360_270(
    x1 : number,
    y1 : number,
    R : number,
    w2 : number,
    overlap : number,
    mask_layer : string
)
{
    //bending arc
    local m=500;
    local arc1=$get_arc([x1-w2/2,y1],[x1-w2/2-(R-w2/2)*(1-1/sqrt(2)),y1-(R-w2/2)/sqrt(2)],[x1-R,y1-(R-
w2/2)],m);
    local arc2=$get_arc([x1-R,y1-(R+w2/2)],[x1-R+(R+w2/2)*sin(rad(45)),y1-
(R+w2/2)*cos(rad(45))],[x1+w2/2,y1],m);
    local a=$create_vector(length(arc1)+2);
    local b=$create_vector(length(arc2)+2);
    a[0]=[x1-w2/2,y1+overlap];
    a[1:length(arc1)]=arc1[0:length(arc1)-1];
    a[length(arc1)+1]=[x1-R-overlap,y1-(R-w2/2)];
    b[0]=[x1-R-overlap,y1-(R+w2/2)];
    b[1:length(arc2)]=arc2[0:length(arc2)-1];
    b[length(arc2)+1]=[x1+w2/2,y1+overlap];
    $add_shape(append(a,b), mask_layer, @internal, @keep, "drawing");
}

```

```

function PeriodicDoubleEtchTaperPRnoGC()
{
//second PR design

local x=0;

local x1=6;

local x2=12;

local y=-830;

local y1=y+65;

local y2=y+110;

local dev2y=-415;

local cladwidth=2;

//Based on WG bias, WG_COREwidth=420nm(on mask) to give 400nm(on chip)

local WG_width=0.4;

local WG_width_flavor=[0, 0.008, 0.014, 0.02, 0.026, 0.032, 0.04];

//10

//Based on WG bias, WG_TREwidth=325nm(on mask)to give 300nm (on chip)

local WGTrench_width=0.32;

//Based on SK bias, SKwidth=260nm(on mask) to give 300nm(on chip)

local Taper_width=0.1;

local TaperW_flavor=[-0.06, -0.045, -0.03, -0.015, 0, 0.015];

local k;

local kk;

for (kk=0; kk<length(WG_width_flavor); kk=kk+1){

for(k=0;k<2;k=k+1){

$add_text("psr215TE_TE",[0.6+x+WG_width_flavor[kk], 15.5],"WG_TEXT", 0.5,@right);

build_PeriodicDoubleEtchTaperPR(0.88, Taper_width, WG_width+WG_width_flavor[kk], 12*2*0.88, 12, x, y);

$add_text("psr215TM_TM",[0.6+x1+5+WG_width_flavor[kk], 15.5],"WG_TEXT", 0.5,@right);

build_PeriodicDoubleEtchTaperPR(0.88, Taper_width, WG_width+WG_width_flavor[kk], 12*2*0.88, 12, x1, y);

$add_text("psr215TE_TM",[0.6+x2+5+WG_width_flavor[kk], 15.5],"WG_TEXT", 0.5,@right);

```

```

build_PeriodicDoubleEtchTaperPR(0.88, Taper_width, WG_width+WG_width_flavor[kk], 12*2*0.88, 12, x2, y);

x=x+73;

x1=x1+73;

x2=x2+73;

}

}

for (kk=0; kk<length(TaperW_flavor); kk=kk+1){

for(k=0;k<2;k=k+1){

$add_text("psr215TE_TE",[0.6+x+TaperW_flavor[kk], 15.5],"WG_TEXT", 0.5,@right);

build_PeriodicDoubleEtchTaperPR(0.88, Taper_width+TaperW_flavor[kk], WG_width, 12*2*0.88, 12, x, y);

$add_text("psr215TM_TM",[0.6+x1+5+TaperW_flavor[kk], 15.5],"WG_TEXT", 0.5,@right);

build_PeriodicDoubleEtchTaperPR(0.88, Taper_width+TaperW_flavor[kk], WG_width, 12*2*0.88, 12, x1, y);

$add_text("psr215TE_TM",[0.6+x2+5+TaperW_flavor[kk], 15.5],"WG_TEXT", 0.5,@right);

build_PeriodicDoubleEtchTaperPR(0.88, Taper_width+TaperW_flavor[kk], WG_width, 12*2*0.88, 12, x2, y);

x=x+73;

x1=x1+73;

x2=x2+73;

}

}

//TE_TE

$add_shape([[x,y], [x+0.4,y-20]], "WG_CORE", @internal, @keep, "drawing");

$add_shape([[x-2-0.05,y+12], [x+0.45+2,y-20-12]], "WG_CLAD", @internal, @keep, "drawing");

$add_shape([[x,y-19.5], [0.4+x,y-19.5], [0.4+x,y-20-1], [0.45+x, y-20-11], [0.45+x, y-20-12], [x-0.05, y-20-12], [x-0.05, y-20-11], [x, y-20-1]], "WG_CORE", @internal, @keep, "drawing");

$add_shape([[x,y-0.5], [0.4+x,y-0.5], [0.4+x,y+1], [0.45+x, y+11], [0.45+x, y+12], [x-0.05, y+12], [x-0.05, y+11], [x, y+1]], "WG_CORE", @internal, @keep, "drawing");

$unselect_all();

$set_autoselect(@true);

$add_shape([[x-0.05, y-20-11.5], [0.45+x, y-20-12]], "WG_CORE", @both); //both means can see both in
device and in cell mode

```

```

    $make_port(@signal, @in, "opt_out");

    $unselect_all();

    $set_autoselect(@true);

    $add_shape([[x-0.05, y+11.5], [0.45+x, y+12]], "WG_CORE", @both); //both means can see both in device
and in cell mode

    $make_port(@signal, @in, "opt_in");

//TM_TM

    $add_shape([[x1,y], [x1+0.4,y-20]], "WG_CORE", @internal, @keep, "drawing");

    $add_shape([[x1-0.05-2,y+12], [x1+0.45+2,y-20-12]], "WG_CLAD", @internal, @keep, "drawing");

    $add_shape([[x1,y-19.5], [0.4+x1,y-19.5], [0.4+x1,y-20-1], [0.45+x1, y-20-11], [0.45+x1, y-20-12], [x1-0.05, y-20-
12], [x1-0.05, y-20-11], [x1, y-20-1]], "WG_CORE", @internal, @keep, "drawing");

    $add_shape([[x1,y-0.5], [0.4+x1,y-0.5], [0.4+x1,y+1], [0.45+x1, y+11], [0.45+x1, y+12], [x1-0.05, y+12], [x1-
0.05, y+11], [x1, y+1]], "WG_CORE", @internal, @keep, "drawing");

    $unselect_all();

    $set_autoselect(@true);

    $add_shape([[x1-0.05, y-20-11.5], [0.45+x1, y-20-12]], "WG_CORE", @both); //both means can see both in
device and in cell mode

    $make_port(@signal, @in, "opt_out");

    $unselect_all();

    $set_autoselect(@true);

    $add_shape([[x1-0.05, y+11.5], [0.45+x1, y+12]], "WG_CORE", @both); //both means can see both in device
and in cell mode

    $make_port(@signal, @in, "opt_in");

x=0;

x1=6;

x2=12;

//for 210nm thickness

for (kk=0; kk<length(WG_width_flavor); kk=kk+1){

    $add_text("psr210TE_TE",[0.6+x+WG_width_flavor[kk], 15.5+dev2y], "WG_TEXT", 0.5,@right);

    build_PeriodicDoubleEtchTaperPR(0.875, Taper_width, WG_width+WG_width_flavor[kk], 12*2*0.875, 12, x,
y+dev2y);

    $add_text("psr210TM_TM",[0.6+x1+5+WG_width_flavor[kk], 15.5+dev2y], "WG_TEXT", 0.5,@right);

```

```

    build_PeriodicDoubleEtchTaperPR(0.875, Taper_width, WG_width+WG_width_flavor[kk], 12*2*0.875, 12, x1,
y+dev2y);

    $add_text("psr210TE_TM",[0.6+x2+5+WG_width_flavor[kk], 15.5+dev2y],"WG_TEXT", 0.5,@right);

    build_PeriodicDoubleEtchTaperPR(0.875, Taper_width, WG_width+WG_width_flavor[kk], 12*2*0.875, 12, x2,
y+dev2y);

    x=x+73;

    x1=x1+73;

    x2=x2+73;

}

for (kk=0; kk<length(TaperW_flavor); kk=kk+1){

    $add_text("psr210TE_TE",[0.6+x+TaperW_flavor[kk], 15.5+dev2y],"WG_TEXT", 0.5,@right);

    build_PeriodicDoubleEtchTaperPR(0.875, Taper_width+TaperW_flavor[kk], WG_width, 12*2*0.875, 12, x,
y+dev2y);

    $add_text("psr210TM_TM",[0.6+x1+5+TaperW_flavor[kk], 15.5+dev2y],"WG_TEXT", 0.5,@right);

    build_PeriodicDoubleEtchTaperPR(0.875, Taper_width+TaperW_flavor[kk], WG_width, 12*2*0.875, 12, x1,
y+dev2y);

    $add_text("psr210TE_TM",[0.6+x2+5+TaperW_flavor[kk], 15.5+dev2y],"WG_TEXT", 0.5,@right);

    build_PeriodicDoubleEtchTaperPR(0.875, Taper_width+TaperW_flavor[kk], WG_width, 12*2*0.875, 12, x2,
y+dev2y);

    x=x+73;

    x1=x1+73;

    x2=x2+73;

}

//for 220nm thickness

for (kk=0; kk<length(WG_width_flavor); kk=kk+1){

    $add_text("psr220TE_TE",[0.6+x+WG_width_flavor[kk], 15.5+dev2y],"WG_TEXT", 0.5,@right);

    build_PeriodicDoubleEtchTaperPR(0.87, Taper_width, WG_width+WG_width_flavor[kk], 12*2*0.87, 12, x,
y+dev2y);

    $add_text("psr220TM_TM",[0.6+x1+5+WG_width_flavor[kk], 15.5+dev2y],"WG_TEXT", 0.5,@right);

    build_PeriodicDoubleEtchTaperPR(0.87, Taper_width, WG_width+WG_width_flavor[kk], 12*2*0.87, 12, x1,
y+dev2y);

    $add_text("psr220TE_TM",[0.6+x2+5+WG_width_flavor[kk], 15.5+dev2y],"WG_TEXT", 0.5,@right);

```

```

    build_PeriodicDoubleEtchTaperPR(0.87, Taper_width, WG_width+WG_width_flavor[kk], 12*2*0.87, 12, x2,
y+dev2y);

    x=x+73;
    x1=x1+73;
    x2=x2+73;

}

//220nm thickness
for (kk=0; kk<length(TaperW_flavor); kk=kk+1){
    $add_text("psr220TE_TE",[0.6+x+TaperW_flavor[kk], 15.5+dev2y],"WG_TEXT", 0.5,@right);
    build_PeriodicDoubleEtchTaperPR(0.87, Taper_width+TaperW_flavor[kk], WG_width, 12*2*0.87, 12, x, y+dev2y);
    $add_text("psr220TM_TM",[0.6+x1+5+TaperW_flavor[kk], 15.5+dev2y],"WG_TEXT", 0.5,@right);
    build_PeriodicDoubleEtchTaperPR(0.87, Taper_width+TaperW_flavor[kk], WG_width, 12*2*0.87, 12, x1, y+dev2y);
    $add_text("psr220TE_TM",[0.6+x2+5+TaperW_flavor[kk], 15.5+dev2y],"WG_TEXT", 0.5,@right);
    build_PeriodicDoubleEtchTaperPR(0.87, Taper_width+TaperW_flavor[kk], WG_width, 12*2*0.87, 12, x2, y+dev2y);

    x=x+73;
    x1=x1+73;
    x2=x2+73;
}

//TE_TE
    $add_shape([[x,y+dev2y], [x+0.4,y-20+dev2y]], "WG_CORE", @internal, @keep, "drawing");
    $add_shape([[x-2-0.05,y+dev2y+12], [x+0.45+2,y-20+dev2y-12]], "WG_CLAD", @internal, @keep, "drawing");
    $add_shape([[x,y-19.5+dev2y], [0.4+x,y-19.5+dev2y], [0.4+x,y-20+dev2y-1], [0.45+x, y-20+dev2y-11], [0.45+x, y-
20+dev2y-12], [x-0.05, y-20+dev2y-12], [x-0.05, y-20+dev2y-11], [x, y-20+dev2y-1]], "WG_CORE", @internal, @keep,
"drawing");
        $add_shape([[x,y-0.5+dev2y], [0.4+x,y-0.5+dev2y], [0.4+x,y+dev2y+1], [0.45+x, y+dev2y+11], [0.45+x,
y+dev2y+12], [x-0.05, y+dev2y+12], [x-0.05, y+dev2y+11], [x, y+dev2y+1]], "WG_CORE", @internal, @keep,
"drawing");

    $unselect_all();

```

```

    $set_autoselect(@true);

    $add_shape([[x-0.05, y-20+dev2y-11.5], [0.45+x, y-20+dev2y-12]], "WG_CORE", @both); //both means can
see both in device and in cell mode

    $make_port(@signal, @in, "opt_out");

    $unselect_all();

    $set_autoselect(@true);

    $add_shape([[x-0.05, y+dev2y+11.5], [0.45+x, y+dev2y+12]], "WG_CORE", @both); //both means can see
both in device and in cell mode

    $make_port(@signal, @in, "opt_in");

//TM_TM

    $add_shape([[x1,y+dev2y], [x1+0.4,y-20+dev2y]], "WG_CORE", @internal, @keep, "drawing");

    $add_shape([[x1-0.05-2,y+dev2y+12], [x1+0.45+2,y-20+dev2y-12]], "WG_CLAD", @internal, @keep, "drawing");

    $add_shape([[x1,y-19.5+dev2y], [0.4+x1,y-19.5+dev2y], [0.4+x1,y-20+dev2y-1], [0.45+x1, y-20+dev2y-11],
[0.45+x1, y-20+dev2y-12], [x1-0.05, y-20+dev2y-12], [x1-0.05, y-20+dev2y-11], [x1, y-20+dev2y-1]], "WG_CORE",
@internal, @keep, "drawing");

    $add_shape([[x1,y-0.5+dev2y], [0.4+x1,y-0.5+dev2y], [0.4+x1,y+dev2y+1], [0.45+x1, y+dev2y+11], [0.45+x1,
y+dev2y+12], [x1-0.05, y+dev2y+12], [x1-0.05, y+dev2y+11], [x1, y+dev2y+1]], "WG_CORE", @internal, @keep,
"drawing");

    $unselect_all();

    $set_autoselect(@true);

    $add_shape([[x1-0.05, y-20+dev2y-11.5], [0.45+x1, y-20+dev2y-12]], "WG_CORE", @both); //both means
can see both in device and in cell mode

    $make_port(@signal, @in, "opt_out");

    $unselect_all();

    $set_autoselect(@true);

    $add_shape([[x1-0.05, y+dev2y+11.5], [0.45+x1, y+dev2y+12]], "WG_CORE", @both); //both means can see
both in device and in cell mode

    $make_port(@signal, @in, "opt_in");

}

function build_PeriodicDoubleEtchTaperPR(TaperL:number {default=0.88}, TaperW:number {default=0.1},
WG_W:number {default=0.42}, WG_L:number {default=21.12}, PR:number {default=12}, x:number {default=0},
y:number {default=0})
{

```

```

    local i;

// Device definition here.

$add_shape([[x,y], [x+WG_W,-WG_L+y]], "WG_CORE", @internal, @keep, "drawing");

$add_shape([[x,2+y], [WG_W+x,-0.5+y]], "WG_CORE", @internal, @keep, "drawing");

$add_shape([[x,-WG_L+0.5+y], [WG_W+x,-WG_L-2+y]], "WG_CORE", @internal, @keep, "drawing");

for (i=0;i<PR;i=i+2){

    $add_shape([[x+WG_W-TaperW, -TaperL+y-i*2*TaperL],[x+WG_W+0.5*TaperW,y+0.5*TaperL-
i*2*TaperL],[x+WG_W+0.5*TaperW+0.2, y+0.5*TaperL-i*2*TaperL],[x+WG_W+0.5*TaperW+0.2, y-0.5*TaperL-
(i+1)*2*TaperL],[x+WG_W+0.5*TaperW,y-0.5*TaperL-(i+1)*2*TaperL]], "SK_TRE", @internal, @keep, "drawing");

    $add_shape([[x+TaperW, -TaperL+y-(i+1)*2*TaperL],[x-0.5*TaperW,y+0.5*TaperL-(i+1)*2*TaperL],[x-
0.5*TaperW-0.2, y+0.5*TaperL-(i+1)*2*TaperL],[x-0.5*TaperW-0.2, y-0.5*TaperL-(i+2)*2*TaperL],[x-0.5*TaperW,y-
0.5*TaperL-(i+2)*2*TaperL]], "SK_TRE", @internal, @keep, "drawing");

}

$add_shape([[x-2.05,y+13.5], [WG_W+2.05+x,y-WG_L-13.5]], "WG_CLAD", @both);

$add_shape([[x,y-WG_L-1.5], [WG_W+x,y-WG_L-1.5], [WG_W+x,y-WG_L-2.5], [0.25+0.5*WG_W+x, y-WG_L-12.5],
[0.25+0.5*WG_W+x, y-WG_L-13.5], [0.5*WG_W-0.25+x, y-WG_L-13.5], [0.5*WG_W-0.25+x, y-WG_L-12.5], [x, y-
WG_L-2.5]], "WG_CORE", @internal, @keep, "drawing");

$add_shape([[x,y+1.5], [WG_W+x,y+1.5], [WG_W+x,y+2.5], [0.25+0.5*WG_W+x, y+12.5], [0.25+0.5*WG_W+x,
y+13.5], [0.5*WG_W-0.25+x, y+13.5], [0.5*WG_W-0.25+x, y+12.5], [x, y+2.5]], "WG_CORE", @internal, @keep,
"drawing");

//add optical input/output ports

$unselect_all();

$set_autoselect(@true);

$add_shape([[0.25+0.5*WG_W+x, y-WG_L-13.5], [0.5*WG_W-0.25+x, y-WG_L-13]], "WG_CORE", @both);
//both means can see both in device and in cell mode

$make_port(@signal, @in, "opt_out");

$add_text("opt_out",[0.25+0.5*WG_W+x, y-WG_L-13.5], "WG_TEXT", 0.5, @right);

$unselect_all();

$set_autoselect(@true);

$add_shape([[0.25+0.5*WG_W+x, y+13.5], [0.5*WG_W-0.25+x, y+13]], "WG_CORE", @both); //both
means can see both in device and in cell mode

$make_port(@signal, @in, "opt_in");

$add_text("opt_in",[0.25+0.5*WG_W+x, y+13.5], "WG_TEXT", 0.5, @right);

```

```

}
function arc_0_90(
    x1 : number,
    y1 : number,
    R : number,
    w2 : number,
    overlap : number,
    mask_layer : string
)
{
    //bending arc
    local m=500;
    local arc1=$get_arc([x1-w2/2,y1],[x1-w2/2-(R-w2/2)*(1-1/sqrt(2)),y1+(R-w2/2)/sqrt(2)],[x1-R,y1+(R-
w2/2)],m);
    local arc2=$get_arc([x1-R,y1+(R+w2/2)],[x1-
R+(R+w2/2)*sin(rad(45)),y1+(R+w2/2)*cos(rad(45))],[x1+w2/2,y1],m);
    local a=$create_vector(length(arc1)+2);
    local b=$create_vector(length(arc2)+2);
    a[0]=[x1-w2/2,y1-overlap];
    a[1:length(arc1)]=arc1[0:length(arc1)-1];
    a[length(arc1)+1]=[x1-R-overlap,y1+(R-w2/2)];
    b[0]=[x1-R-overlap,y1+(R+w2/2)];
    b[1:length(arc2)]=arc2[0:length(arc2)-1];
    b[length(arc2)+1]=[x1+w2/2,y1-overlap];
    $add_shape(append(a,b), mask_layer, @internal, @keep, "drawing");
}
function arc_180_90(
    x1 : number,
    y1 : number,
    R : number,
    w2 : number,

```

```

        overlap : number,
        mask_layer : string
    )
{
    //bending arc
    local m=500;
    local arc1=$get_arc([x1-w2/2,y1],[x1-w2/2+(R+w2/2)*(1-
1/sqrt(2)),y1+(R+w2/2)/sqrt(2)],[x1+R,y1+(R+w2/2)],m);
    local arc2=$get_arc([x1+R,y1+(R-w2/2)],[x1+R-(R-w2/2)*sin(rad(45)),y1+(R-
w2/2)*cos(rad(45))],[x1+w2/2,y1],m);
    local a=$create_vector(length(arc1)+2);
    local b=$create_vector(length(arc2)+2);
    a[0]=[x1-w2/2,y1-overlap];
    a[1:length(arc1)]=arc1[0:length(arc1)-1];
    a[length(arc1)+1]=[x1+R+overlap,y1+(R+w2/2)];
    b[0]=[x1+R+overlap,y1+(R-w2/2)];
    b[1:length(arc2)]=arc2[0:length(arc2)-1];
    b[length(arc2)+1]=[x1+w2/2,y1-overlap];
    $add_shape(append(a,b), mask_layer, @internal, @keep, "drawing");
}

function arc_270_180(
    x1 : number,
    y1 : number,
    R : number,
    w2 : number,
    overlap : number,
    mask_layer : string
)
{
    //bending arc
    local m=500;

```

```

        local arc1=$get_arc([x1,y1-w2/2],[x1-(R+w2/2)/sqrt(2),y1-w2/2+(R+w2/2)*(1-1/sqrt(2))],[x1-
(R+w2/2),y1+R],m);

        local arc2=$get_arc([x1-(R-w2/2),y1+R],[x1-(R-w2/2)*sin(rad(45)),y1+R-(R-
w2/2)*cos(rad(45))],[x1,y1+w2/2],m);

        local a=$create_vector(length(arc1)+2);

        local b=$create_vector(length(arc2)+2);

        a[0]=[x1+overlap,y1-w2/2];

        a[1:length(arc1)]=arc1[0:length(arc1)-1];

        a[length(arc1)+1]=[x1-(R+w2/2),y1+R+overlap];

        b[0]=[x1-(R-w2/2),y1+R+overlap];

        b[1:length(arc2)]=arc2[0:length(arc2)-1];

        b[length(arc2)+1]=[x1+overlap,y1+w2/2];

        $add_shape(append(a,b), mask_layer, @internal, @keep, "drawing");
    }

function arc_360_270(
    x1 : number,
    y1 : number,
    R : number,
    w2 : number,
    overlap : number,
    mask_layer : string
)
{
    //bending arc

    local m=500;

    local arc1=$get_arc([x1-w2/2,y1],[x1-w2/2-(R-w2/2)*(1-1/sqrt(2)),y1-(R-w2/2)/sqrt(2)],[x1-R,y1-(R-
w2/2)],m);

    local arc2=$get_arc([x1-R,y1-(R+w2/2)],[x1-R+(R+w2/2)*sin(rad(45)),y1-
(R+w2/2)*cos(rad(45))],[x1+w2/2,y1],m);

    local a=$create_vector(length(arc1)+2);

    local b=$create_vector(length(arc2)+2);

    a[0]=[x1-w2/2,y1+overlap];

```

```
a[1:length(arc1)]=arc1[0:length(arc1)-1];
a[length(arc1)+1]=[x1-R-overlap,y1-(R-w2/2)];
b[0]=[x1-R-overlap,y1-(R+w2/2)];
b[1:length(arc2)]=arc2[0:length(arc2)-1];
b[length(arc2)+1]=[x1+w2/2,y1+overlap];
$add_shape(append(a,b), mask_layer, @internal, @keep, "drawing");
}
```